

**THE EFFECTS OF POROSITY ON THE
FATIGUE BEHAVIOUR OF GALFENOL**

**LES EFFETS DE LA POROSITÉ SUR LES
PROPRIÉTÉS EN FATIGUE DU GALFENOL**

A Thesis Submitted to the Division of Graduate Studies
of the Royal Military College of Canada
by

David Ian Holsworth, BEng, CD
Major

In Partial Fulfillment of the Requirements for the Degree of
Master of Applied Science in Mechanical Engineering

December 2015

© This thesis may be used within the Department of National Defence but
copyright for open publication remains the property of the author.

I would like to dedicate this work to my wonderful wife Kim and my amazing little boy Justin.

Acknowledgements

First and foremost, I would like to thank my wife for her tireless support and understanding throughout the duration of this project. I would also like to thank Mr. Jeff Fleming whose help in the preparation of specimens and use of laboratory equipment was critical to the success of this project. Dr. Jennifer Snelgrove's help in the use of the scanning electron microscope and Dr. Kevin Jaansalu's advice at the onset of this thesis were also appreciated. Dr. Underhill's help with the image and statistical analysis helped give this project more depth and Dr. Cerantola was especially helpful in the revision of my written work. Last but not least, I would also like to thank my supervisor, Dr. DuQuesnay who has provided me with excellent guidance, timely support, and patience when required.

Abstract

The fatigue behaviour of three Galfenol steels, alloys predominantly composed of iron and gallium, was investigated. Gallium contents were 18.4 at.%, 14.9 at.%, and 12.4 at.% for F, C, and M series Galfenol, respectively. C series Galfenol also had 2.2 at.% tertiary chromium, additions known to improve corrosion resistance. For all three alloys, commercially pure gallium was alloyed with low carbon steels, resulting in less than 0.15 at.% carbon content. As-received rods were produced by Bridgman rod extrusion to enhance the preferential grain orientation required to maximize the sought-after magnetostrictive effect. The as-received rods measured 24 mm diameter and 125 mm long and each was machined into eight cylindrical dogbone fatigue specimens with 4.5 mm diameter gauge sections. Constant amplitude fully reversed tension compression ($R = -1$) fatigue tests were performed on the dogbone specimens. The initial fatigue results were highly scattered with one standard deviation on life being of one order of magnitude. The as-received material was also very porous, with macropores as large as 500 μm . Hence, the primary objective of this study was to determine if reducing the porosity would improve fatigue behaviour. Hot iso-static pressing (HIP) at 310 MPa and 1250 °C increased material densities by $1\% \pm 0.1\%$ and removed $86\% \pm 6\%$ of surface area porosity. More importantly, macroporosity was removed and the largest remaining pores after HIP had Feret mean diameters less than 30 μm . After HIP, data scatter increased by 43% for the F series and was reduced by 8% for the C series. Although many of the specimens were longer lasting for the HIP F series, given the resulting high level of scatter, there was not enough statistical evidence to indicate that HIP improved its fatigue behaviour. On the contrary, mean fatigue lives for the HIP C series Galfenol was improved by 95%. Fatigue results of each of the three as-received Galfenol series were essentially the same, indicating that gallium contents between 12.4–18.4 at.% have no effect on fatigue behaviour of Galfenol. Given that fatigue behaviour of C and F series was not dramatically affected by HIP although the porosity was greatly reduced, HIP of M series was not pursued. It is suspected that the relatively large grain size and the weak boundary cohesion caused by gallium rich precipitates are responsible for the persistent large scatter in fatigue data, even after porosity reduction.

Résumé

La durée de vie en fatigue de trois alliages de Galfenol, un acier principalement composé de fer et de gallium, a été étudiée. Les tenures en gallium des alliages étaient respectivement de 18.4 at.%, 14.9 at.%, et 12.4 at.% pour les séries F, C, et M. La série C contenait 2.2 at.% de chrome comme élément tertiaire, un ajout reconnu pour améliorer la résistance à la corrosion des aciers. La pureté du gallium employé dans les trois alliages et l'acier utilisé resultat en une basse tenue en carbone, soit moins de 0.15 at.%. Les tiges de Galfenol de ce projet furent fabriquées par extrusion Bridgman et mesuraient 24 mm de diamètre et 125 mm en longueur. Chaque tige a été machinées pour produire huit échantillons de fatigue cylindriques avec un diamètre interne de 4.5 mm. Les essais en fatigue consistaient en de charge-ments uniaxiaux purement alternés ($R = -1$). Les résultats initiaux étaient très dispersés avec un écart type sur la vie d'un ordre de grandeur. Le matériel possédait des macropores mesurant jusqu'à 500 μm , alors il fut décidé de traiter les tiges par pressage isostatique à chaud (310 MPa et 1250 °C) avant de poursuivre les essais en fatigue. Le traitement de pressage a augmenté la masse volumique des échantillons par 1% \pm 0.1% et a réduit par 86% \pm 6% la surface totale occupée par les pores. Aussi, ce traitement élimina la macroporosité puisque les pores les plus larges observés suite au traitement mesuraient moins de 30 μm de diamètre. Après le traitement de pressage, la variabilité des résultats en fatigue de la série F (FH) a augmenté de 43% et celle de la série C (CH) a été diminuée de 8%. Étant donné la variabilité des résultats, il n'était pas possible de déterminer statistiquement si le pressage à chaud a contribué à une amélioration nette des résultats. Par contre, les résultats en fatigue de la série CH ont duré en moyenne 95% plus longtemps que les échantillons de la série C. Les résultats en fatigue des trois alliages étaient effectivement les mêmes, indiquant que la tenue en gallium entre 12.4–18.4 at.% a peu d'impact sur la résistance à la fatigue du Galfenol. Puisque les effets de pressage sur les propriétés en fatigue étaient limités, le pressage de la série M n'a pas été poursuivi. Il est soupçonné que la grosseur macroscopique des grains et l'affaiblissement du Galfenol causée par les hautes tenures en gallium sont aussi des causes principales de la variabilité des résultats.

Contents

Acknowledgements	iii
Abstract	iv
Résumé	v
List of Tables	ix
List of Figures	x
1 Introduction	1
1.1 Background	1
1.2 Objectives	2
1.3 Outline	3
2 Literature Review	4
2.1 General	4
2.2 Magnetostriction	4
Evolution of magnetostrictive metals	6
2.3 Discovery and evolution of Galfenol alloys	9
2.3.1 Thermal history and temperature effect	10
2.3.2 Compression effect	10
2.3.3 Crystal structure and mechanisms of magnetostriction	12
2.3.4 Secondary phases	12
2.4 Polycrystalline Galfenol	14
2.4.1 Production of polycrystalline Galfenol	14
2.4.2 Material embrittlement	16
2.4.3 Grain size and hardness	16
2.4.4 Production of polycrystalline Galfenol	17
2.5 Mechanical properties of Galfenol	19

2.5.1	Material yielding and deformation behaviour	21
2.5.2	Ternary addition effects	22
	Chromium additions	24
2.6	Fatigue	24
2.6.1	General	24
2.6.2	Mechanisms of fatigue failure	25
2.6.3	Fatigue testing	27
2.6.4	Scatter in fatigue results	28
2.6.5	Fatigue of Galfenol	29
2.7	Porosity	29
2.7.1	General	29
2.7.2	Effects of porosity on mechanical properties	31
2.7.3	Porosity effects on fatigue	31
2.8	Grain size effects on mechanical properties	34
2.8.1	Grain size effect on fatigue of metals	35
2.8.2	Stages of crack growth in large grains	37
2.9	Summary	38
3	Materials and Methodology	40
3.1	General	40
3.2	Materials	40
3.3	Specimen preparation and preliminary tests	40
	3.3.1 Hot iso-static pressing (HIP)	42
	3.3.2 Post-HIP specimen preparation	43
3.4	Fatigue testing	44
	3.4.1 Test conditions	45
	3.4.2 Test monitoring and interruptions	45
	3.4.3 Yield stress	46
3.5	Post-processing and analysis	46
	3.5.1 Fracture surface observation	47
	3.5.2 Metallographic specimen observation	47
	3.5.3 Microporosity	47
	3.5.4 Material texture	49
4	Results	51
4.1	Fatigue results	51
4.2	Density	55
4.3	Porosity	55
	4.3.1 Pore size and pore size distribution	56
	4.3.2 Surface area porosity	56

4.4	Hardness	59
4.5	Yield stress	59
5	Discussion	61
5.1	Experimental approach	61
5.2	Hot iso-static pressing (HIP)	62
5.2.1	Encapsulation	63
5.2.2	HIP effects on density	64
	Water displacement	65
	Density measurement results	65
5.2.3	HIP effects on pore sizes	66
5.2.4	HIP effects on pore shape	67
5.2.5	HIP effects on mechanical properties and fatigue behaviour .	67
5.3	Image analysis	72
5.3.1	Image analysis software	72
5.4	Fractography	73
5.5	Sources of fatigue failure	75
5.5.1	Grain size and effects on fatigue behaviour	76
5.5.2	Deformation mechanism	77
5.6	M series testing	79
6	Conclusions	80
7	Recommendations	82
	References	83
	Appendices	88
A	Density measurements	89
B	Analysis of variances (ANOVA)	92
C	Collected Data	94

List of Tables

1.1	Comparison of approximate material properties for magnetostrictive materials	1
2.1	Room temperature magnetostriction values for some Fe-based alloys	8
2.2	Magnetostriction potential and grain size for two FSZM extraction rates of directionally solidified Fe _{81.6} Ga _{18.4} Galfenol	18
2.3	Elastic properties of binary Galfenol	21
2.4	Mechanical properties Fe _{81.6} Ga _{18.4} Galfenol	22
4.1	Material densities (ρ) and porosity (P) for as-received and HIP Galfenol	55
5.1	Fatigue data analysis results	69
C.1	Rockwell B hardness results for F series Galfenol	95
C.2	Rockwell B hardness results for C series Galfenol	96
C.3	Rockwell B hardness results obtained for M series Galfenol	97
C.4	Fatigue data for the F series Galfenol	98
C.5	Fatigue data for the FH series Galfenol	99
C.6	Fatigue data for the C series Galfenol	100
C.7	Fatigue data for the CH series Galfenol	101
C.8	Fatigue data for the M series Galfenol	101

List of Figures

2.1	Schematic depiction of magnetostrictive strain	5
2.2	Saturation magnetostriction (λ_s) for at-rest and compressively pre-strained specimens	6
2.3	Technical saturation magnetostriction potential testing	7
2.4	Galfenol magnetostriction potential	9
2.5	Effect of temperature on magnetostrictive potential	10
2.6	Effects of compression of Galfenol's magnetostrictive potential	11
2.7	Binary Galfenol atomic configurations within a 16-atom unit cell model	12
2.8	Galfenol binary phase diagram	13
2.9	Binary Galfenol crystallographic structure	14
2.10	Schematic diagram of a vertical Bridgman crystal growth process in a single-zone furnace	15
2.11	Grain sizes for binary and steel Galfenol after 24-hour anneal at 1200 °C	17
2.12	Grain orientation map of research grade Galfenol produced using the FSZM technique	18
2.13	Carbon effect on magnetostrictive strain in Ga-rich Galfenol	23
2.14	Types of constant amplitude cyclic loading	24
2.15	Early stages of crack initiation	25
2.16	Typical propagation of a fatigue crack	26
2.17	Schematic representation of the stages of fatigue crack growth	26
2.18	Stress-life curves that typify fatigue test results of unnotched 300M alloy steels	27
2.19	Example of fatigue scatter for a low-carbon steel	28
2.20	Density effect on the crack growth propagation of sintered steel	32
2.21	Porosity effect on the fatigue behaviour of cast 8630 steel	33
2.22	Stress-life fatigue curves of porous sintered steel	34
2.23	Fatigue limit and yield stress and grain size for cartridge brass	35
2.24	Stress-life curves for various metals with different grain sizes	36
2.25	Stress-life fatigue curves for VT3-1 titanium alloy	37

2.26	Stress-life fatigue data for various grain sizes of stainless steel	38
3.1	Brittle fracture of Galfenol during machining of the as-received material	41
3.2	As-received Galfenol sample and machined fatigue specimen	41
3.3	Fatigue specimen dimensions	41
3.4	Visible surface-connected porosity on Galfenol rods.	42
3.5	Encapsulated Galfenol rods as-received after HIP operation.	43
3.6	Electromechanical loading frame used for fatigue testing.	44
3.7	Load and stroke output for the first half cycle of a fatigue test.	46
3.8	Sectioned specimens	48
3.9	Polished metallographic specimen example	48
3.10	Example of image processing using Matrox software	49
3.11	Grain texture as captured on etched metallographic specimens of F and C series Galfenol	50
4.1	Stress-life results for F and FH Series	52
4.2	Stress-life results for C and CH Series	53
4.3	Stress-life test results for all three as-received Galfenol series with R = -1	54
4.4	Effect of etching on Galfenol metallographic specimens.	56
4.5	Number and size of pores detected in six micrographs (27.4 mm ²) of F and FH series metallographic specimens.	57
4.6	Number and size of pores detected in six micrographs (27.4 mm ²) of C and CH series metallographic specimens.	57
4.7	F and FH series relative pore surface area	58
4.8	C and CH series relative pore surface area	58
4.9	Material hardness	59
4.10	Stress-strain path from rest to yielding for the first half cycle of fatigue tests	60
5.1	Macroporosity and visible grain boundaries on the as-received material	62
5.2	Effect of encapsulation on surface connected pores	63
5.3	Plastic deformation of the HIP capsule	64
5.4	Large surface connected pore observed in specimen F49	66
5.5	Pore geometry before and after HIP for F and C Series Galfenol	68
5.6	Plastic deformation observed for larger HIPed pores	68
5.7	Effect of HIP on fatigue behaviour of Galfenol with R = -1	71
5.8	Illustration of the contrasting effect on pore size analysis.	72
5.9	Mixed mode inter and intragranular fracture surfaces of C, CH, F, and FH Galfenol	74

5.10	Fracture surface of long-lasting specimen C2 with visible striations and thumbnail formation	74
5.11	Suspected sources of failure in short lived fatigue specimens	75
5.12	Slip band formation in fatigue specimens	77
5.13	Dislocation pile-up occurrences at grain boundaries	78
A.1	Glassware used to perform water displacement tests.	89
A.2	Scale used to measure the weight of Galfenol rods and displaced water from submerged rods.	90
A.3	Insertion of specimen for water displacement test.	91

List of Symbols and Abbreviations

$\%EL$	Percent elongation
ΔK	Stress intensity factor range
λ	Magnetostrictive strain
λ_s	Technical saturated magnetostrictive strain
ν	Poisson's ratio
ρ	Material density
ρ_t	Flaw tip radius
ρ_{th}	Theoretical material density
σ_a	Stress amplitude
σ_m	Mean stress
σ_o	Material resistance to the movement of dislocations
σ_r	Stress range
σ_y	Yield stress
A	Anisotropy parameter
a	Crack or flaw characteristic length
$at.\%$	Atomic percentage
B	Bulk stiffness
c_{ij}	Elastic constants
d	Grain size parameter

D_f	Feret mean diameter
D_{max}	Feret maximum diameter
D_{min}	Feret minimum diameter
da/dN	Incremental crack length growth per cycle
E	Elastic modulus
$FSZM$	Free standing zone melt
H	Magnetic force
HIP	Hot iso-static pressing
K_t	Stress concentration factor
k_y	Hall-Petch unpinning constant
M	Magnetization
M_s	Magnetization saturation
P	Porosity
R	Stress ratio
$stdv$	Standard deviation
$wt.\%$	Weight percentage
$(3/2)\lambda_s$	Free strain or magnetostrictive strain potential
BCC	Body centered cubic
BSE	Back-scattered electrons
DS	Directionally solidified
HRB	Rockwell hardness, B scale
N_f	Number of cycles to failure
P/M	Powder metallurgy
SEM	Scanning electron microscopy
T_m	Melting temperature

1 Introduction

1.1 Background

Galfenol is a type of smart or functional material that possesses magnetostrictive properties. Functional materials are defined by their ability to efficiently couple thermal, electrical, or magnetic properties with accompanying changes in mechanical behaviour. Magnetostrictive materials are known for their ability to pair applied magnetic fields with elastic deformations or strains.

Although the magnetostrictive effect was first discovered by Joule [1] in 1847, its first practical application occurred during WWII when nickel alloys were used in the newly invented sonars. Since then, advances in material science have resulted in the production of magnetostrictive materials with sensitivities over an order of magnitude greater than the magnetostrictive potentials achieved in the nickel-based alloys first introduced during WWII. As can be seen in Table 1.1, piezo-ceramics and iron based alloys containing rare-earth elements such as terbium and dysprosium (Terfenol-D) now possess magnetostrictive potentials nearly two orders of magnitude larger than those observed in iron or nickel alloys (~ 30 -50 parts per million or ppm) or steel. Unfortunately, these advanced materials were expensive to manufacture and given their brittle nature, costly to operate in rugged environments where they are prone to failure.

Table 1.1: Comparison of approximate material properties for Galfenol and other magnetostrictive materials [2, 3].

Material	Piezo-ceramics	Terfenol-D	Galfenol	Steel
Magnetostriction (ppm)	1000	2000	400	30
Modulus of elasticity (GPa)	60	25-35	200	200
Tensile strength (MPa)	28	28	500	400-1200
Ductile/Brittle	Brittle	Brittle	Ductile	Ductile

Note: ppm represents strain expressed in parts per million, where 1000 ppm equates to 0.1% strain.

In an effort to develop more cost effective instrumentation for the U.S. Navy, in 1999, the Magnetic Materials Group at the U.S. Naval Surface Warfare Centre investigated the potential of Fe-Ga alloys for fabrication of sensing equipment. These alloys, named Galfenol, are binary iron-gallium alloys typically containing around 20 atomic percent (at.%) gallium. Although the new metal alloy does not possess the same magnetostrictive potential as some other advanced ceramics, its steel-like mechanical properties, including toughness, machinability, and strength make it a good prospective replacement for inherently brittle materials currently used in high-tech sensing applications. In spite of the fact that Galfenol single crystals can achieve up to 400 ppm magnetostrictive strain, they are still relatively costly to produce.

In order make Galfenol-based sensing equipment cost effective, production of bulk polycrystalline material is required. Because the magnetization-mechanical coupling characteristics are so heavily dependent on crystal orientation, only directional solidification (DS) and hot rolling processes have been shown to produce a grain orientation that is uniform enough to produce acceptable magnetostriction levels. With polycrystalline processes possible, production costs may be reduced by up to 80% over more expensive functional ceramics like Terfenol-D [4].

Considering that Galfenol possesses good mechanical properties, its development has brought with it the onset of new magnetostrictive applications, including actuators, energy harvesters, and vibration control applications. Seeing as many of these applications are typically exposed to cyclical loading, it is necessary to determine the material's fatigue behaviour. Initial steps for this project included tension-compression fatigue testing. Because the as-received Galfenol samples were laden with up to 0.5% surface area porosity and the fatigue data was heavily scattered, it was decided to remove porosity by hot iso-static pressing (HIP) before pursuing with further testing.

1.2 Objectives

The central focus of this project was to observe and document the fatigue behaviour of DS Galfenol. Fatigue behaviour will be defined as the relationship between stress and life as seen on S-N curves. This also encompasses data the slope and intercept of S-N curves as well as the degree of scatter observed in fatigue test results. Given that previously obtained fatigue data on as-received Galfenol was abnormally scattered and that the material was laden with visible surface-connected macropores, the following objectives were derived:

1. Evaluate the effectiveness of hot iso-static pressing (HIP) on the reduction of porosity in Galfenol.

2. It was found that HIP was effective at removing up to 96% of the material porosity. Therefore, the second objective was to evaluate the effect of porosity reduction on the fatigue behaviour of Galfenol.
3. Seeing as Galfenol specimens with three different alloys were tested, the third objective was to determine how gallium content affected fatigue behaviour.

1.3 Outline

The remainder of this manuscript is organized as follows: Chapter 2 consists of a comprehensive review of the literature and material science theory that is pertinent for this project. Chapters 3 and 4 describe the procedures used during the experimental portion of this project as well as the results obtained from the various tests. Chapter 5 presents a discussion of results and key findings from this project, and finally Chapters 6 and 7 present conclusions and recommendations.

2 Literature Review

2.1 General

The first part of this literature review will consist of an overview of magnetostriction as a material property. After providing a brief summary of the evolution of magnetostrictive materials which ultimately lead to the recent discovery of Galfenol, a summary of the key research that has been published on this new alloy will also be provided. Although this project was conducted on polycrystalline Galfenol, the majority of the baseline research available is on the single crystal form of the alloy.

There is little to no research yet published on the the effects of porosity and material texture on fatigue behaviour of Galfenol. As these topics are closely linked with the project objectives, the last part of this review includes a summary of key findings of the effects of porosity and texture on the fatigue behaviour of similar iron-based alloys.

2.2 Magnetostriction

Joule [1] first introduced the concept of magnetostriction to the scientific community in 1847. In his ground breaking work, he identified that ferromagnetic materials like Fe and steel possessed the ability to change shape or strain, somewhat, when faced with a preferentially oriented magnetic field of strength H . This is in essence the description of magnetostrictive strain. The magnitude of the strain in a given orientation is symbolized by λ_{xyz} and x , y , and z represent crystallographic directions. Given that for ferromagnetic materials these types of strains remain well within the elastic regime, on the order 10^{-5} to 10^{-4} , λ is typically expressed in parts per million (ppm) where 1 ppm equates to a strain of 10^{-6} . For the sake of context, pure Fe possesses a maximum potential for λ of ~ 30 ppm in its preferential or magnetostrictively easy cubic crystal orientation [1]. Figure 2.1 illustrates how the application of a magnetic field (H) causes a reorientation of magnetic domains, which in turn can impart strains on a material.

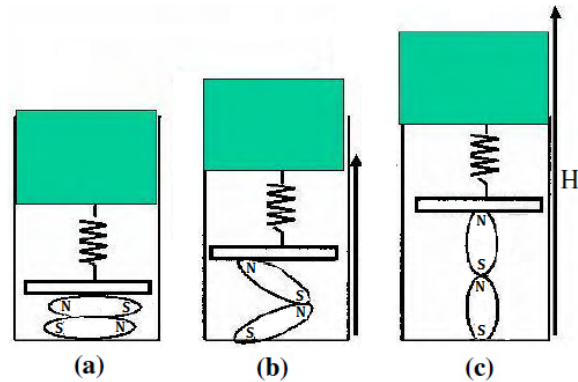


Figure 2.1: Schematic depiction of magnetostrictive strain. The ellipses depict magnetic domains and the applied field (H) is depicted both in magnitude and direction [2]. a) no strain b) some strain (λ) c) technical magnetostrictive saturation (λ_s).

The degree to which magnetic domains are reoriented in a material is dependent on the direction and strength of H . As can be seen in Figure 2.1c, once the magnetic domains become completely aligned in parallel with the applied magnetic field, the technical saturated magnetostrictive strain is achieved (λ_s). This is the material property which quantifies a ferromagnetic material's potential to be strained by a magnetic field in a given direction. The level of induced magnetization (M) incurred when λ_s is achieved is called the technical saturation magnetization (M_s) and is measured in A/m or oersteds, where $1 \text{ Oe} = 79.58 \text{ A/m}$. Increases in magnetization beyond M_s do not produce further strains. The ratio of M_s and λ_s directly impacts the sensitivity of a magnetostrictive material which in turn is a critical factor in the design of sensing equipment.

Unlike the illustration in Figure 2.1a, ferromagnetic metals at rest typically possess magnetic domains that are randomly oriented (Figure 2.1a). A better representation of this phenomenon is also included in Figure 2.2a. In this figure, the application of a sufficiently large magnetic field (H) results in the reorientation of the material's magnetic domains which in turn produces strains as large as λ_s .

Because "at-rest" materials possess randomly oriented magnetic domains, the potential for strain in a given direction can actually be larger than λ_s . In order to maximize strains in a given direction, it is first necessary to align domains perpendicular to the axis of the applied magnetic field. As depicted in Figure 2.2b, using a sufficiently large compressive strain of Δ can produce an alignment of magnetic domains perpendicular to the longitudinal axis. Once this has occurred, the application of a magnetic field along the longitudinal axis can result in larger strains than what can be produced from rest. In this case, total strain in the longitudinal axis is $\lambda_s + \Delta$.

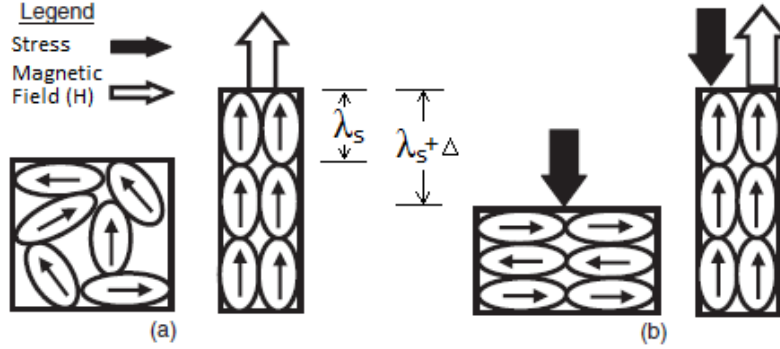


Figure 2.2: Saturation magnetostriction (λ_s) for (a) “at-rest” magnetostrictive materials and (b) materials for which a compressive pre-strain (Δ) is applied before the application of the magnetic field [5].

This is also called the magnetostrictive potential of a material, or $(3/2)\lambda_s$, which is always larger than λ_s . See Section 2.3.2 for additional information regarding the effects of compressive pre-stresses on Galfenol.

Without the application of a compressive “pre-strain”, $(3/2)\lambda_s$ may not be determined by measuring strains along one axis. Conveniently, $(3/2)\lambda_s$ can be determined by calculating the difference in λ_s produced along two perpendicular directions using the following equation:

$$(3/2)\lambda_s = \lambda_{\parallel} - \lambda_{\perp} = \lambda_{100} - (-(1/2)\lambda_{100}) = (3/2)\lambda_{100} \quad (2.1)$$

The experimental procedure used to obtain $(3/2)\lambda_s$ is depicted in Figure 2.3. In this figure, λ_{\parallel} and λ_{\perp} to a known crystallographic orientation can be used to determine $(3/2)\lambda_s$ using equation 2.1. In the example provided in the previous equation, the potential for λ_{100} is calculated. This is the main experimental technique that has been used to determine $(3/2)\lambda_s$ of Galfenol specimens [4, 6].

Evolution of magnetostrictive metals

Two decades after Joule [1] discovered the magnetostrictive effect, in 1865, the Italian physicist Villari identified that ferromagnetic materials also demonstrated the inverse or Villari effect when subjected to mechanical deformations [7]. Villari discovered that an imparted strain on a ferromagnetic material would affect its magnetic properties. In essence, the magnetostrictive effect discovered by Joule is the main material property utilized in the design and fabrication of actuating devices while the Villari effect is predominantly utilized in the design of sensing or energy harvesting devices.

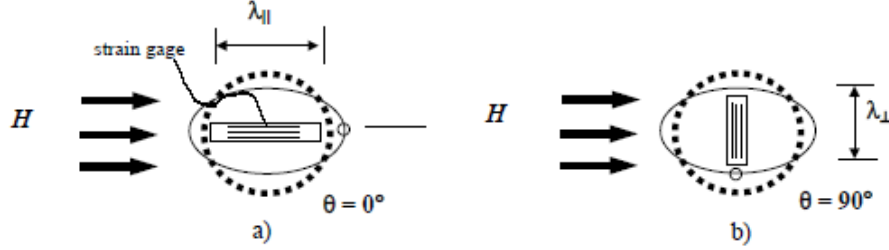


Figure 2.3: Technical saturation magnetostriction potential testing using a disk-shaped ferromagnetic specimen. a) λ_s is measured in parallel to the [100] direction, yielding saturation magnetostriction λ_{\parallel} ; b) λ_s is then measured perpendicular to the specimen [100] direction, yielding saturation magnetostriction λ_{\perp} . $(3/2)\lambda_s = \lambda_{\parallel} - \lambda_{\perp}$ and dotted lines represent the unstrained specimen [4].

About half a century later, in 1926, Honda and Kaya [8] discovered that the magnetostrictive effect observed in Fe and steel was highly anisotropic. They established that body centered cubic (BCC) metals possessed magnetostrictive easy, medium, and hard directions, $\langle 100 \rangle$, $\langle 110 \rangle$, and $\langle 111 \rangle$, respectively.

Although the magnetostriction effect had been observed for nearly one century, the first practical applications of magnetostrictive materials did not occur until WWII. At this time, nickel (Ni) alloys were introduced as acoustic transducers in the fabrication of sound navigation and ranging (SONAR) devices [9]. Possessing modest λ_s of ~ 50 ppm, not much more than pure Fe, successful use of Ni alloys in new sonar technologies would prove to be the catalyst for the development of new sensing and actuating materials in the decades to follow.

In 1959, two researchers significantly advanced the understanding of the magnetostrictive effect in metals. Tatsumoto and Okamoto [10] identified that below Fe's Curie temperature of $\sim 700^\circ\text{C}$, λ_s in single crystal Fe was inversely proportional to temperature. In the same year, Hall [11] discovered that substitution of non-magnetic elements with Fe could improve λ_s by nearly one order of magnitude. A summary of his key findings is provided in Table 2.1. In line with the work done by Honda and Kaya [8], Hall showed that Fe-Ga binary alloys were also highly anisotropic, with $\langle 100 \rangle$ as the magnetostrictively easy or strong and $\langle 111 \rangle$ as the magnetostrictively weak directions.

Four years after Hall's discovery, in 1963, Clark *et al.* [12] discovered that rare-earth elements such as terbium (Tb) and dysprosium (Dy) held at 80 K could possess λ_s as high as 60 000 ppm, nearly two orders of magnitude larger than those observed in any other metal. Unfortunately, because Tb and Dy's Curie temperatures are well below freezing temperatures (273 K), the sought-after magneto-mechanical

Table 2.1: Room temperature magnetostriction values for some Fe-based alloys in the strong and weak magnetostrictive directions, $\lambda_{(100)}$ and $\lambda_{(111)}$, respectively [11].

Alloy addition	Symbol	Content (at.%)	λ_{100} (ppm)	λ_{111} (ppm)
Gallium	Ga	17	207	-
Gallium	Ga	13	153	-16
Aluminum	Al	16	86	-2
Chromium	Cr	15.6	51	-6
Vanadium	V	15.6	43	-10

behaviour was essentially lost at room temperature, ~ 295 K. In order to increase magnetostrictive levels at room temperature, Clark *et al.* [6] investigated the potential of alloying these highly magnetostrictive elements with Fe, known to possess a much higher Curie temperature of around 700°C . Clark *et al.* successfully produced TbFe_2 and DyFe_2 alloys with high enough Curie temperatures to produce magnetostrictive levels as high as $\lambda_s = 2000$ ppm at room temperature [13], one order of magnitude higher than the Fe-Ga alloys researched by Hall.

This advancement in the development of magnetostrictive materials proved promising, yet one draw-back of these newly discovered rare-earth element alloys was that high levels of magnetization were required to obtain λ_s [14]. Essentially, these new alloys were not sensitive enough for use in the production of sensing or actuating applications.

In 1972, further research by Clark and Benson [13] lead to the development of a balanced alloy consisting of $\text{Tb}_{.27}\text{Dy}_{.73}\text{Fe}_{1.95}$ which possessed more practical levels of M_s . Named Terfenol-D for its three compositional elements and the place of its discovery¹, this new rare-earth and Fe-based alloy would quickly rival piezoceramics such as lead zirconic titanate (PZT) and lead magnesium niobate (PMN) as the material of choice for fabrication of sensing and actuating devices.

As one can read from Table 1.1, Terfenol-D's very high λ_s is accompanied with inherent brittleness and relative low strength. Albeit used for decades as the material of choice in U.S. Navy sensing equipment, Terfenol-D's propensity to fail in harsh and demanding environments was proving to be too costly. In the late 1990s, the U.S. Navy's Naval Surface Warfare Centre (NSWC) (formerly N.O.L.), would fund research in the hopes of finding a tougher material that could replace the more brittle and costly legacy smart materials used in U.S. naval sensing equipment.

¹**T**erbium, **fe** for Fe, **-D** for dysprosium, and **no**l for the U.S. Naval Ordnance Laboratory (N.O.L.).

2.3 Discovery and evolution of Galfenol alloys

Of the binary alloys studied by Hall [11, 15], Fe-Ga combinations possessed the largest magnetostrictive potential (see Table 2.1). Although still only producing strains about one-tenth of those observed in Terfenol-D, Fe-Ga alloys possess steel-like machineability, strength, and toughness. As these are all properties lacking in the more brittle Terfenol-D, Clark *et al.* [16], who had been researching magnetostrictive materials for decades, further examined the potential applications of Fe-Ga alloys.

Applying the same naming convention used for Terfenol-D, Fe-Ga binary alloys would be named Galfenol. As described by Kellogg [4], raw materials for the manufacturing of Galfenol cost about one-quarter of costs associated with the manufacturing of Terfenol-D. Coupled with its steel-like robustness, Galfenol quickly became a great prospective material for the design of sensing and actuating instruments.

In their early work, Clark's group [16] mapped the magnetostrictive potential of furnace cooled single crystal Galfenol with varying Ga content. They concluded that increases in Ga content could enhance the magneto-mechanical behaviour observed in BCC α -Fe matrix up to $(3/2)\lambda_s$ of 400 ppm, far eclipsing magnetostrictive strains observed by Hall [16].

As can be seen in Figure 2.4, maximum strains were obtained in the cubic $\langle 100 \rangle$ directions when Ga contents were above ~ 20 at. %.

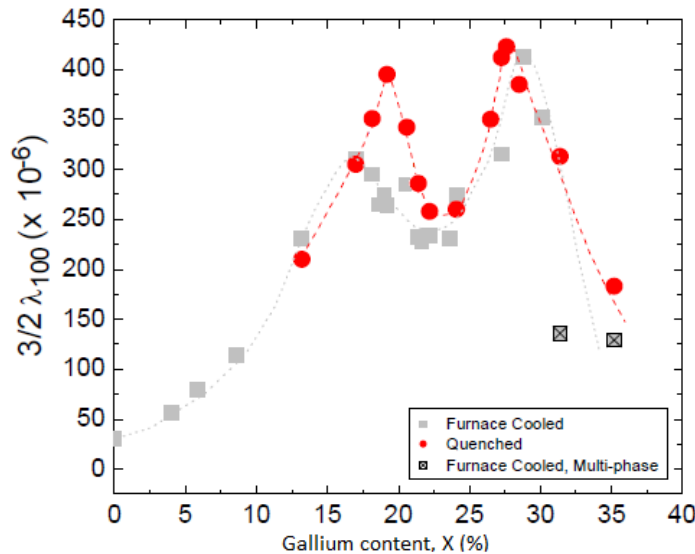


Figure 2.4: Magnetostrictive potential for binary Galfenol single crystals with varying thermal histories. $\text{Fe}_{100-x}\text{Ga}_x$ and $H = 15$ kOe [17].

2.3.1 Thermal history and temperature effect

Even if Figure 2.4 shows that $(3/2)\lambda_s$ occurs at two peaks, Galfenol with high Ga content becomes too brittle to be machined or formed [18] and only alloys with Ga contents below ~ 25 at.% are typically considered for useful applications [4]. One can note from the previous figure that cooling rates or thermal history can increase Galfenol's $(3/2)\lambda_s$, especially for $x \sim 18$ -25 at.% [19]. As included in this figure caption, at.% alloy compositions are often expressed as subscript values next to their respective element symbol.

Noting the work done decades earlier by Tatsumoto and Okamoto [10], reducing material temperature improves Galfenol's magnetostrictive behaviour [20]. Unlike TbFe_2 or DyFe_2 , Curie temperatures for Galfenol alloys are close to that of Fe, around 700°C . For this reason, useful levels of λ_s are retained at ambient temperatures. Clark *et al.* [6] showed that reductions of 100°C increased λ_s by 10% (see Figure 2.5).

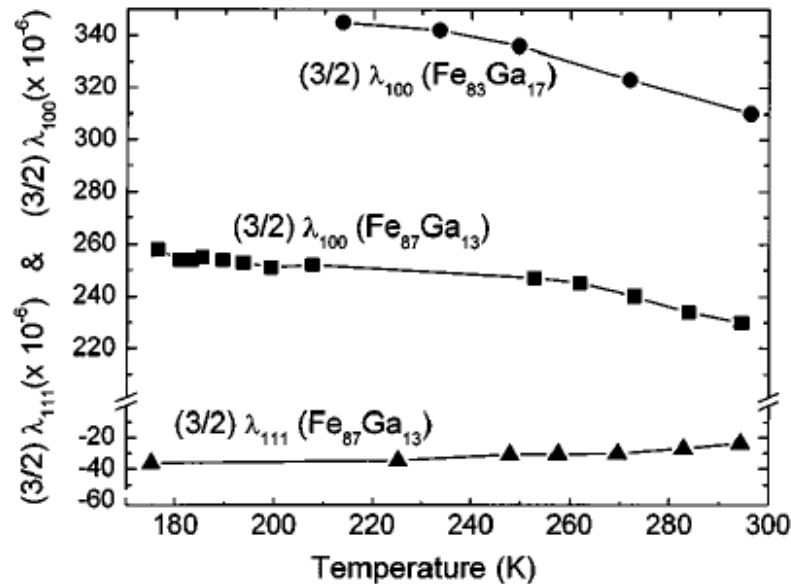


Figure 2.5: Magnetostriction in the [100] and [111] direction, $(3/2)\lambda_{100}$ and $(3/2)\lambda_{111}$, respectively [16].

2.3.2 Compression effect

As illustrated in Figure 2.2a, it is difficult to obtain a ferromagnetic material with perfectly aligned magnetic domains. Having tested the magnetostrictive response

of various compositions of Galfenol, Clark *et al.* [6] concluded that compressive stresses ($-\sigma$) could increase λ_s by nearly 50%. Figure 2.6 illustrates this effect on a high Ga content Galfenol sample at room temperature. It is to be noted that the magnitude of the compressive stresses are below 100 MPa.

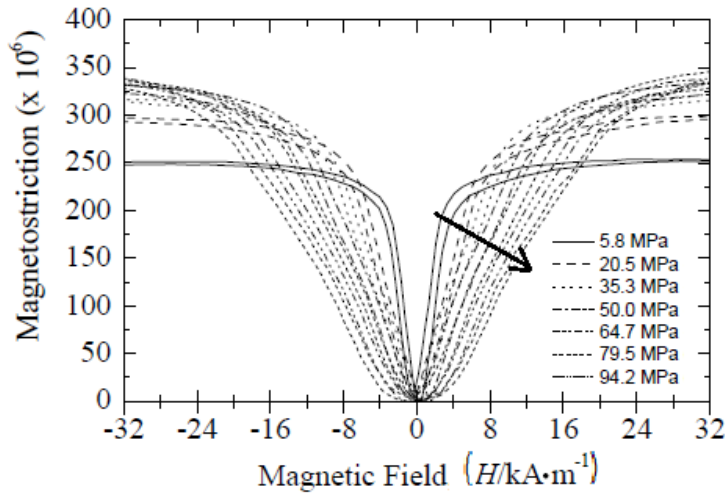


Figure 2.6: Effects of compression on $\text{Fe}_{81}\text{Ga}_{19}$ binary Galfenol's magnetostrictive potential where the arrow indicates increasing compression [6].

Wun-Fogle *et al.* [17] showed that compressive stresses can be introduced into Galfenol specimens by stress annealing (see Figure 2.2). In their work, they applied a variety of compressive and tensile stresses to Galfenol during annealing. Compressive stresses held during annealing helped align and maintain magnetic domains perpendicular to the magnetostrictive strain axis, leading to larger λ_s upon magnetization. Use of this technique essentially removed the need to maintain a compressive stress on the specimen to maximize λ_s [21].

Others, such as Brooks *et al.* [22] found that magnetic field annealing can be used to magnetically align domains perpendicular to the strain axis (see Figure 2.2b). Once magnetized, the magnetic domains can be kept in place by annealing the material. After observing annealing conditions between 300 and 700 °C, the 1 T magnetic field can be removed and the domains remain preferentially aligned, perpendicular to the desired strain axis [22]. Stress annealing has since become the manufacturing process of choice for many bulk Galfenol manufacturing processes.

2.3.3 Crystal structure and mechanisms of magnetostriction

As eluded to in Kellogg's dissertation on the development of Fe-Ga alloys [4], an exact understanding of how or why Ga substitutions into a single-phased α -Fe matrix produce such abnormally large strains was not well understood. It was theorized that substituted Ga atoms which are about 10% larger than Fe atoms, produce a distortion within the α -Fe matrix when pairs of Ga atoms are aligned along one of the cubic directions ($\langle 100 \rangle$). When exposed to a magnetic field, the localized unit cell strains are relaxed and distortion occurs. Basic geometry dictates that orthorhombic and tetrahedral orientations within BCC cells, $\langle 110 \rangle$ and $\langle 111 \rangle$ respectively, are longer than the unit cell parameter in the cubic directions $\langle 100 \rangle$. For this reason, internal strains resulting from the presence of two larger Ga atoms along non-cubic orientations are effectively negligible.

Even if the BCC unit cell model provides some basis from which to explain Galfenol's crystallographic structure, the two models most commonly used to describe elastic and magnetostrictive behavior of Galfenol are the 16-atom unit cell seen in Figure 2.7 and the 128-atom unit cell. For Galfenol with less than 12.5 at.% Ga content, the smaller model is sufficient to characterize Galfenol behaviour. For higher Ga content Galfenol, the larger 128-atom unit cell is required to reproduce more accurate characterization [23].

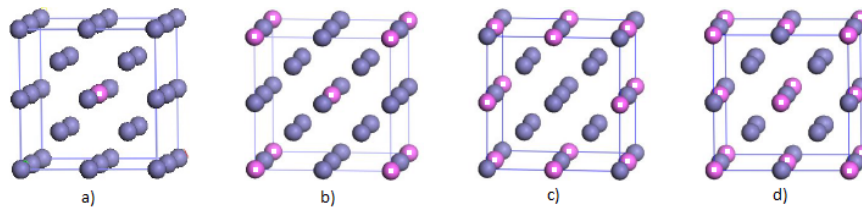


Figure 2.7: Binary Galfenol atomic configurations for 16-atom cubic cell structures. $\text{Fe}_{100-x}\text{Ga}_x$; where $x = 6.25, 12.5, 18.75,$ and 25 from a) to d), respectively. Pink balls with white squares represent gallium atoms [24].

2.3.4 Secondary phases

Datta *et al.* [25] analyzed the effects of thermal history on material crystallographic structure and dependent magnetostrictive potential. They established that thermal history only affected magnetostriction in Galfenol with Ga contents above 17 at.%. Using high resolution X-Ray diffraction, they found that quenched Galfenol with more than 17 at.% Ga maintained a uniform homogenous α -Fe like phase. Conversely, slow-cooled high Ga content Galfenol contained multiple phases. Figure 2.8

2.3. Discovery and evolution of Galfenol alloys

shows that near Ga contents of 20 at.% result in the expected formation of secondary and even tertiary phases.

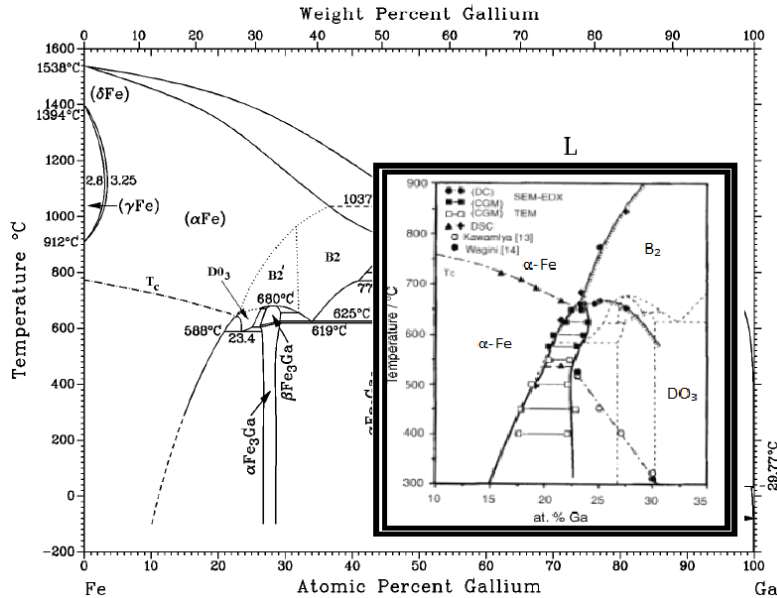


Figure 2.8: Binary Fe-Ga phase diagram where γ , α , β , DO_3 , and B_2' represent various crystallographic formations or phases [26]. The smaller scale sub figure was obtained from [27].

It was determined that α phases consist of randomly distributed and substituted Ga atoms within the Fe homogeneous phase. For higher content Galfenol, it is expected that Ga atoms cluster together in neighbouring unit cells, hereby creating a long-range ordering of distorted unit cells. This long range ordering produces the secondary phases discussed earlier.

Unit cell structures for these phases are represented in Figure 2.9. It is theorized that in these high Ga concentration secondary phases, unit cell distortions are self-canceling and macroscopic strains are therefore mostly negated [27]. This explains why λ_s is reduced in Galfenol with Ga contents above 17 at.%, where the presence of DO_3 and B_2 phases is expected (see Figure 2.8).

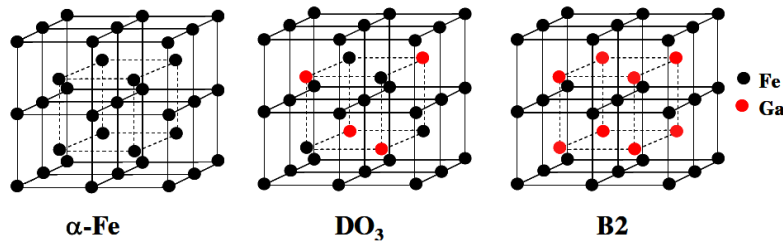


Figure 2.9: Binary Galfenol crystallographic structure for various structures [2].

2.4 Polycrystalline Galfenol

Considering that Galfenol's sought-after magnetostriction effect is highly anisotropic and strains are well within the elastic regime, early research was predominantly conducted on single crystals [6, 16, 19, 24, 28, 29]. Although this research helped identify the full potential of Galfenol's magnetostrictive effect, production of Galfenol single crystals is too slow and expensive to be deemed a viable solution for replacing Terfenol-D or PZTs. In order to achieve cost savings over more expensive piezoceramics, bulk Galfenol needed to be produced in the polycrystalline form.

2.4.1 Production of polycrystalline Galfenol

More recent research, like that of Kellogg's [4] and Summers' [30], has been aimed at developing processes for producing polycrystalline Galfenol with more useful levels of magnetostrictive potential. In his early work, Kellogg assessed over twelve manufacturing techniques ranging from powder metallurgy (P/M) to forging. The biggest challenge in maximizing λ_s for polycrystalline Galfenol was assuring the highest degree of preferential crystalline orientation in a given specimen. For this reason, it is critical that manufacturing methods result in maximized cubic texture.

In practice, it is not possible to perfectly align crystals during the manufacturing process of bulk polycrystalline metals. As seen earlier, $(3/2)\lambda_{110}$ and $(3/2)\lambda_{111}$ for Galfenol are very small and slight misorientations of grains within a polycrystalline sample quickly detract from the overall magnetostrictive effect in the desired [100] axis. As well, it is also believed that the presence of grain boundaries also disrupt the magnetostrictive effect. Compared with single-crystal specimens which produced $(3/2)\lambda_s$ up to ~ 400 ppm, most polycrystalline specimens produced by Kellogg [4] possessed $(3/2)\lambda_s$ well below 100 ppm. Of the fifteen processes tested by Kellogg, two produced alloys with $(3/2)\lambda_s \sim 165$ ppm, still less than half of what was reported by Clark *et al.* [16] for single crystals.

Kellogg's first successful method consisted of hot rolling a stainless steel encap-

ulated cast Galfenol ingot measuring 9.5 mm x 51 mm x 51 mm at approximately 1000 °C. The starting ingot thickness was reduced by 55%, down to 4.2 mm over a series of 72 rolling passes with reheating to 1000 °C every three passes. After hot rolling, the sample was annealed in 99.99% argon gas at 475 °C for 180 min, then at 1100 °C for 240 min, and furnace cooled for 8 hours. Specimens from this sample produced on average $(3/2)\lambda_s$ of ~ 160 ppm [4].

The other technique that resulted in comparable levels of magnetostriction consisted of directional solidification (DS) using a modified Bridgman rod method. This is the same method used to produce the Galfenol samples for this project and previously by Clark and Kellogg [6, 16, 28] to manufacture single crystal specimens. As can be seen in Figure 2.10, this process is initiated by arc welding a starting ingot containing the alloy elements, in this case, a mixture of high purity Fe and Ga. This typically occurs in a noble gas environment to prevent oxidization. Once the alloy has been melted numerous times to ensure an even alloy solution, the crucible used for melting the alloy is slowly extracted from the heat source to help induce crystal growth. This solidification technique introduces a desirably high degree of texture which maximizes λ_s for polycrystalline Galfenol.

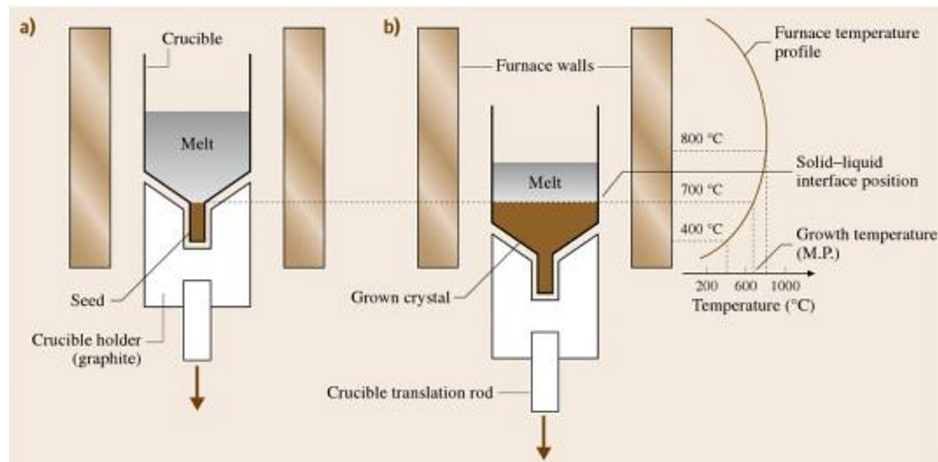


Figure 2.10: Schematic diagram of a vertical Bridgman crystal growth process in a single-zone furnace: a. at the beginning of the growth process and b. with a partially grown crystal [31].

Extraction rates from the heat source can be as low as 2–4 mm/hr. Slow extraction rates are required to produce uniform cubic texture and grain formation along the Bridgman rod's longitudinal axis [30]. Once the extraction is complete, the sample is annealed to maximize homogeneity as the formation of secondary phases is known to reduce λ_s [20]. Using faster extraction rates of 100 mm/hr and an alumina crucible to

produce a 50.8 mm long and 6.35 mm diameter Bridgman rod, Kellogg [4] produced polycrystalline $\text{Fe}_{83}\text{Ga}_{17}$ Galfenol which possessed $(3/2)\lambda_s$ of 170 ppm with an optimized stress level of 28 MPa. Unfortunately, the material produced was deemed too brittle to be machined or formed.

2.4.2 Material embrittlement

Subsequent grinding of the DS specimen grown by Kellogg [4] caused shattering and intergranular brittle fracture. Once fractured, further “light” strikes with a hammer resulted in further intergranular brittle fracture. Remarkably, grains were measured to be 2–4 mm in diameter and as much as 20 mm in length. Forceful hammering of single crystals only produced plastic deformation. This indicates that although Galfenol has the potential to be ductile, abnormally large grain growth leads to low fracture toughness in polycrystalline Galfenol specimens. It is believed that Ga-rich intermetallics precipitate along grain boundaries which in turn causes weak bonds between grains and lowers fracture toughness [4].

Seeing as the potential applications for Galfenol consist of small sensors or actuators [32, 33, 34], controlling grain size (d) and minimizing brittle intergranular fracture is critical for the successful development and manufacturing of small components. Because of the inherent brittleness of DS specimens, Kellogg [4] concluded from his work that the preferred method of manufacturing polycrystalline Galfenol was in the highly textured sheet form where hot rolling techniques help maximize preferential cubic grain orientation.

2.4.3 Grain size and hardness

Brooks and Summers [18] also investigated the effect of Ga content on d and hardness of Galfenol. Using electron spectroscopy and a scanning electron microscope (SEM), they observed fracture surfaces and material texture of hot rolled Galfenol specimen’s tested by three-point bending. Because post-forming heat treatments above 1100 °C had been proven to harden the Galfenol [4], they annealed the hot-rolled specimens in argon at 1200 °C for 24 hours to promote brittle fracture. The summary of the d measurements is included in Figure 2.11.

Using Vickers hardness testing on single crystal specimens, Brooks and Summers [18] determined that binary Galfenol with 15 and 20 at.% Ga contents had hardness of 200 and 250, respectively. Vickers hardness was as high as 475 for $\text{Fe}_{100-x}\text{Ga}_x$ with $x \geq 30\%$. These findings suggest that Galfenol undergoes a ductile to brittle transition between 15.5 and 18.4 at.% Ga content. Unfortunately, this coincides with the range of Ga content shown to significantly increase $(3/2)\lambda_s$ (see Figure 2.4). Therefore,

maximizing magnetostrictive potential is typically coupled with inherent brittleness which limits machining and manufacturing options.

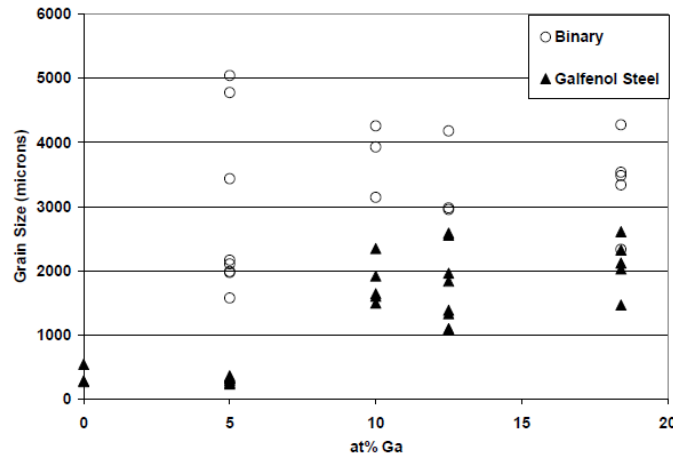


Figure 2.11: Grain sizes (d) for binary and steel Galfenol after 24-hour anneal at 1200 °C [18].

2.4.4 Production of polycrystalline Galfenol

Due to its ability to retain some ductility, Kellogg [4] recommended that bulk polycrystalline Galfenol be produced by hot rolling. Unfortunately, this process was time consuming and the resulting sheet material could not be pre-stressed due to potential buckling in the rolling direction (see Section 2.3.2). Although Galfenol sheet might be useful for certain applications, this manufacturing approach may not be best suited for component designs requiring bulk 3-D volume or applications where compressive stress annealing might be desired to maximize λ_s . Therefore, DS remains an important production technique for manufacturing bulk Galfenol.

The modified Bridgman rod technique described in Section 2.4 consists of increasing extraction rates up to about 100 mm/hr. The more conventional Bridgman technique used to grow single crystals takes place at a much slower rate, 2-4 mm/hr. Summers *et al.* [30] further investigated the effect of extraction rate on d and $(3/2)\lambda_s$. Using the Free Standing Zone Melt (FSZM) method, which is in essence quite similar to the modified Bridgman technique, Summers *et al.* grew 10 mm diameter and 250 mm long $\text{Fe}_{81.6}\text{Ga}_{18.4}$ Galfenol rods. With 50 MPa pre-strain compressive stresses, they produced the $(3/2)\lambda_s$ tabulated in Table 2.2:

Interestingly, a 130% increase in extraction rates reduced $(3/2)\lambda_s$ by about 20% and produced polycrystalline Galfenol with d_{ave} that was 50% smaller. Considering

Table 2.2: Magnetostriction potential ($(3/2)\lambda_s$) and resulting grain size (d) from two FSZM extraction rates of directionally solidified $\text{Fe}_{81.6}\text{Ga}_{18.4}$ Galfenol [30].

Grade	extraction rate (mm/hr)	d (mm)	$(3/2)\lambda_s$ (ppm)
Research	25	1.350 ± 0.150	190 ± 25
Production	350	0.650 ± 0.085	149 ± 12

that high Ga content Galfenol is known to be brittle in part due to its large grains and weak inter-grain cohesion, reducing d would certainly prove to be beneficial (see Section 2.8 for more details on the effects of d).

In order to standardize the size and roughness of some of the DS specimens, Summers *et al.* [30] machined the outside layer of some specimens. Overall, $(3/2)\lambda_s$ in both grades of Galfenol was increased by an average of 15%, with maximum increases as high as 39%. It was theorized that during cooling, outside grains are exposed to a different temperature gradient which can promote off-axis and non-preferential growth. Using Orientation Imaging Microscopy techniques as can be seen in Figure 2.12, Summers *et al.* demonstrated that removing approximately 1.5 mm of material from the specimen surfaces, over 95% of the remaining grains were preferentially oriented, and $(3/2)\lambda_s$ was consequently improved. This discovery exemplifies how sensitive to crystallographic orientation λ_s can be.

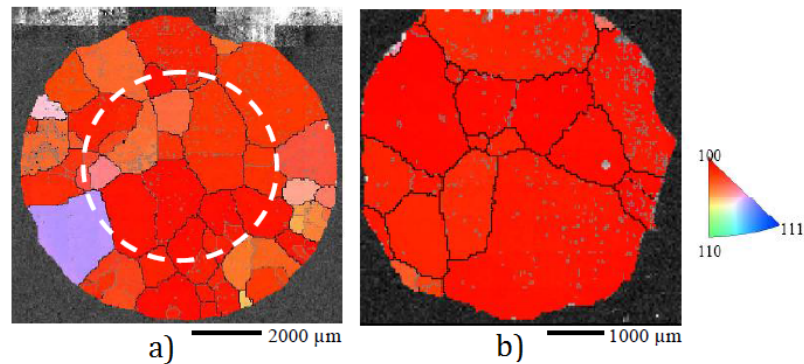


Figure 2.12: Grain orientation map of research grade Galfenol produced using the FSZM technique [30].

2.5 Mechanical properties of Galfenol

Most metals possess microstructures with sub mm d and isotropic mechanical behaviour. Polycrystalline Galfenol is an exception because by design, it possesses a high degree of cubic texture required to maximize λ_s . As $(3/2)\lambda_s$ in Galfenol are below the 500 ppm threshold (0.05%), well within the material's elastic regime, most published works were focused on mechanical behaviour well below the point of yielding. For anisotropic materials, the analysis of elastic behaviour is most easily expressed using Hooke's Law, where material stress-strain (σ - ϵ) behaviour is described by the following relationship $\sigma_i = c_{ij}\epsilon_j$ where $i, j = 1 \dots 6$. In its expanded form, this relationship can be expressed as the following:

$$\begin{pmatrix} \sigma_1 \\ \sigma_2 \\ \sigma_3 \\ \sigma_4 \\ \sigma_5 \\ \sigma_6 \end{pmatrix} = \begin{pmatrix} \sigma_1 \\ \sigma_2 \\ \sigma_3 \\ \sigma_4 \\ \sigma_5 \\ \sigma_6 \end{pmatrix} = \begin{pmatrix} c_{11} & c_{12} & c_{13} & c_{14} & c_{15} & c_{16} \\ c_{21} & c_{22} & c_{23} & c_{24} & c_{25} & c_{26} \\ c_{31} & c_{32} & c_{33} & c_{34} & c_{35} & c_{36} \\ c_{41} & c_{42} & c_{43} & c_{44} & c_{45} & c_{46} \\ c_{51} & c_{52} & c_{53} & c_{54} & c_{55} & c_{56} \\ c_{61} & c_{62} & c_{63} & c_{64} & c_{65} & c_{66} \end{pmatrix} \begin{pmatrix} \epsilon_1 \\ \epsilon_2 \\ \epsilon_3 \\ \epsilon_4 \\ \epsilon_5 \\ \epsilon_6 \end{pmatrix} \quad (2.2)$$

For BCC metals such as Fe and Galfenol, unit cell symmetry simplifies the c_{ij} tensor and elastic behaviour can be described using only c_{11} , c_{12} , and c_{44} since $c_{11} = c_{22} = c_{33}$ and $c_{44} = c_{55} = c_{66}$ and $c_{12} = c_{21} = c_{13} = c_{31} = c_{23} = c_{32}$ [35]. This helps simply equation 2.2 down to the following equation:

$$\begin{pmatrix} \sigma_1 \\ \sigma_2 \\ \sigma_3 \\ \sigma_4 \\ \sigma_5 \\ \sigma_6 \end{pmatrix} = \begin{pmatrix} c_{11} & c_{12} & c_{12} & & & \\ c_{12} & c_{11} & c_{12} & & & \\ c_{12} & c_{12} & c_{11} & & & \\ & & & c_{44} & & \\ & & & & c_{44} & \\ & & & & & c_{44} \end{pmatrix} \begin{pmatrix} \epsilon_1 \\ \epsilon_2 \\ \epsilon_3 \\ \epsilon_4 \\ \epsilon_5 \\ \epsilon_6 \end{pmatrix} \quad (2.3)$$

Shortly after their initial work on $(3/2)\lambda_s$ of single crystal Galfenol, Clark *et al.* [19] investigated the mechanical behaviour of Galfenol with the goal of determining the elastic constants. In their work, they used resonant ultrasound spectroscopy techniques to determine elastic constants of Galfenol with different Ga contents. Kellogg *et al.* [28] experimentally measured material σ - ϵ relations by conducting tensile tests on single crystal specimens oriented in the [100], [110], and [111] directions. A year later, Yoo and Flatau [29] further examined the mechanical behaviour of Galfenol single crystals with Ga contents ≥ 17 at.%.

For BCC materials, stiffness (E) in the cubic and orthorhombic directions are given by the following relationships:

$$E_{[100]} = \frac{c_{11}R'}{c_{11} + c_{12}} \quad (2.4)$$

$$E_{[110]} = \frac{4c_{44}R'}{R' + 2c_{44}} \quad (2.5)$$

and R' is defined as:

$$R' = \frac{1}{c_{11}}(c_{11} - c_{12})(c_{11} + 2c_{12}) \quad (2.6)$$

Poisson's ratios (ν) are also defined by the stiffness constants according to the following relationships:

$$\nu_{(001),[010]} = \nu_{(010),[001]} = \frac{c_{12}}{c_{11} + c_{12}} \quad (2.7)$$

$$\nu_{(001),[1\bar{1}0]} = \frac{R' - 2c_{44}}{R' + 2c_{44}} \quad (2.8)$$

$$\nu_{(1\bar{1}0),[001]} = \frac{4c_{12}c_{44}}{c_{11}(R' + 2c_{44})} \quad (2.9)$$

In order to determine c_{ij} experimentally, Kellogg used strain gauges and load cells to measure material σ - ϵ during tensile tests. For a variety of specimens with different crystallographic orientations, E and ν were determined using the following equations:

$$E \equiv \frac{1}{n} \sum_n \frac{\sigma_n}{\epsilon_{long,n}} \quad (2.10)$$

$$\nu \equiv \frac{1}{n} \sum_n \frac{-\epsilon_{trans,n}}{\epsilon_{long,n}} \quad (2.11)$$

Having determined E and ν along different axis, elastic constants c_{ij} could then be calculated using the previous equations. Rearranged, they produce the following relationships:

$$c_{11} = \frac{(1 - \nu_{(001),[010]})E_{[100]}}{(1 + \nu_{(001),[010]})(1 - 2\nu_{(001),[010]})} \quad (2.12)$$

$$c_{12} = \frac{\nu_{(001),[100]}E_{[100]}}{(1 + \nu_{(001),[010]})(1 - 2\nu_{(001),[010]})} \quad (2.13)$$

2.5. Mechanical properties of Galfenol

Table 2.3 summarizes key values obtained on Galfenol elastic properties. The anisotropy parameter (A) and bulk stiffness (B) are expressed using equation 2.14 and equation 2.15, respectively.

$$A = \frac{2c_{44}}{c_{11} - c_{12}} \quad (2.14)$$

$$B = (1/3)(c_{11} + 2c_{12}) \quad (2.15)$$

Before obtaining the results listed in Table 2.3, the most anisotropic material ever reported was that of lithium with $A = 9.2$ [36, 37]. Jain *et al.* [36] demonstrated that as A increases and the material becomes more anisotropic, $\nu_{(001),[0\bar{1}0]}$ became more negative. As can be seen in Table 2.3, Ga additions significantly reduce $\nu_{(001),[0\bar{1}0]}$. Materials with negative ν are considered to possess auxetic behaviour [38]. Exploitation of this material property has led to the development of some unique component designs [9, 33, 34, 39].

Table 2.3: Elastic properties of binary Galfenol with $\text{Fe}_{100-x}\text{Ga}_x$ and x is the at.% Ga content. Data obtained from A-[40], B-[28], C-[19], and D-[29].

at% Ga in Fe	GPa						A	[100] loading	[110] loading	
	c_{11}	c_{12}	c_{44}	$E_{[100]}$	$E_{[110]}$	$E_{[111]}$		$\nu_{[010]}$	$\nu_{[1\bar{1}0]}$	$\nu_{[001]}$
0.0 ^A	228	132	117	131	219	283	2.4	0.37	-0.06	0.61
17.0 ^B	225	181	128	65	160	315	5.7	0.45	-0.37	1.11
18.6 ^D	201	160	111	59	144	-	5.4	0.44	-0.55	-
18.7 ^C	196	156	123	57	145	297	6.2	0.44	-0.41	1.13
24.1 ^C	186	168	120	27	86	293	12.9	0.47	-0.64	1.48
27.2 ^C	221	207	135	20	68	334	19.9	0.48	-0.75	1.64
28.9 ^D	135	121	116	19.8	65	-	17.2	0.47	-0.63	-
28.9 ^{D2}	135	121	101	19.8	63	-	15.1	0.47	-0.53	-
33.2 ^D	-	-	-	-	79.8	-	-	-	-0.58	-

2.5.1 Material yielding and deformation behaviour

Kellogg's [28] $\text{Fe}_{83}\text{Ga}_{17}$ single crystal tensile tests revealed that specimens oriented in the [100] direction exhibited discontinuous yielding. It was believed that this was caused by twin deformation, kink band formation or stress-induced transformation of secondary phases. Ultimate tensile strengths (UTS) was 515 MPa and E was 65 GPa. Failure occurred at 2% elongation (%EL). In the [110] direction, the single crystals were stiffer, with an E of 160 GPa. UTS was measured as being 580 MPa through 1.6%EL and ν in this direction was particularly auxetic, -0.37.

In line with the embrittlement behavior observed by Brooks and Summers [18], Kellogg [28] found that the addition of Ga greatly reduced E in the $\langle 100 \rangle$ and $\langle 110 \rangle$ directions whereas the material property in the $\langle 111 \rangle$ directions was hardly affected (see Figure 2.3). This in part explains why magnetostrictively induced strains are far greater in the $\langle 100 \rangle$ and $\langle 110 \rangle$ directions.

Other work completed on Galfenol's mechanical properties was that of Brooks and Summers [18]. Motivated by the prospect of manufacturing this material for potential industrial purposes, they studied the impact of Ga content on mechanical properties of polycrystalline Galfenol. Depending on compositions and processing, DS polycrystalline Galfenol components possess UTS ranging from 350-580 MPa and B ranging from 72-86 GPa.

The work done by Summers *et al.* [30] on DS polycrystalline Galfenol also included published mechanical properties. The average values obtained from eight research-grade and twenty production-grade FSZM polycrystalline $\text{Fe}_{81.6}\text{Ga}_{18.4}$, they observed the following mechanical properties:

Table 2.4: Summary of mechanical properties of $\text{Fe}_{81.6}\text{Ga}_{18.4}$ Galfenol [18].

Material	B (GPa)	UTS (MPa)	Ductility (% EL)
[100] Single Crystal	65	515	2
Research Grade	72.4	370	1.2
Production Grade	86.3	348	0.81

2.5.2 Ternary addition effects

The Galfenol alloys used in this study are in fact Galfenol steels, possessing C as a tertiary element. Some of the specimens also contain Cr additions. For this reason, mention will be made of the effect these alloy additions have on material properties.

Although Ga additions have been shown to improve hardness [4], they do not produce parallel increases in strength. On the contrary, weak Ga-rich precipitates which form at grain boundaries reduce grain boundary cohesion. To counter this effect, trace amounts of C can be added to aid in maintaining grain boundary cohesion [41]. Additionally, C additions in Galfenol have similar strengthening and stiffening effects as those observed in steels.

Cheng *et al.* [42] demonstrated that C and manganese (Mg) additions improved rollability of Galfenol by reducing the quantity and size of edge cracking. Nolting [43] further assessed this phenomenon and determined that this effect was predominantly caused by the C additions. She determined that ~ 0.15 at.% C additions in-

creased σ_y by over 100 MPa and that ductility could be increased up to $\sim 15\%$ EL. C additions were also found to transform failure mechanisms from intergranular fracture to intragranular fracture. This supports the claim that C additions help increase grain boundary cohesion.

Clark *et al.* [44] demonstrated that small trace C additions can increase λ_s in Ga-rich Galfenol. As can be seen in Figure 2.13, the reduction in $(3/2)\lambda_{100}$ expected at ~ 19 at.% Ga content is delayed with the presence of C additions. It is believed that small atom interstitials like that of C, boron, or nitrogen help maintain a generalized disordering of Ga atoms in solution, delaying the formation of long-range ordered DO₃ phases.

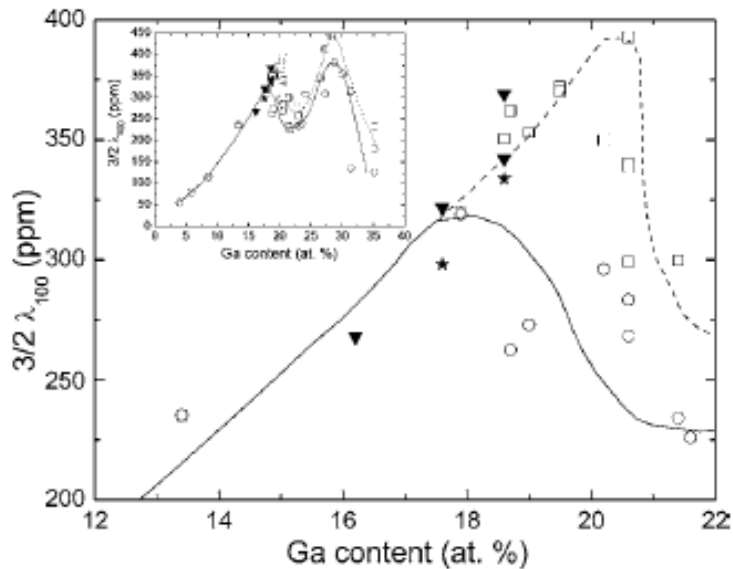


Figure 2.13: Carbon effect on magnetostrictive strain (λ) in Ga-rich Galfenol [44]. Symbols are for the following conditions/alloys: hollow circles for unquenched Fe-Ga, hollow squares for quenched Fe-Ga, full triangles for unquenched Fe-Ga-C, and full stars for quenched Fe-Ga-C.

Summers *et al.* [21] also considered the effects of C on the anisotropy of Galfenol. They determined that the addition of low-carbon steel to Galfenol increased strength and toughness while having little effect on the magnetostrictive anisotropy. As was presented in Figures 2.11, the effect of C also greatly reduced grain size. More will be discussed on this in Section 2.8.

Chromium additions

As is the case for stainless steel, Cr additions are well known to significantly enhance corrosion resistance of Fe-based alloys. Given that potential use of Galfenol sensing equipment might be destined for use in maritime or other harsh demanding environment, corrosion resistance would likely be desired. In line with the research done by Cheng and Nolting [42, 43] at Defence Research and Development Canada, fatigue resistance of Cr-doped Galfenol was also considered for this project.

As with many other alloy additions, Cr additions have been shown to have a few other benefits. Cr additions to Fe increases hardenability and combined with C additions, improves wear and abrasion resistance of steels [45]. Clark *et al.* [44] showed that Cr additions up to 2 at.% did not detract from the magnetostrictive behaviour of Galfenol. Nolting [43] showed that %EL at fracture for three 2 at.% polycrystalline Galfenol tension test specimens ranged between 7–16%.

2.6 Fatigue

2.6.1 General

Considering that the main objective of this project consisted of fatigue testing of Galfenol specimens, the next section will provide a brief overview of the principles of fatigue of metals, fatigue testing, as well as a summary of some literature concerned with fatigue of Galfenol. Fatigue of materials occurs when cyclical loading of relatively small σ result in the propagation of fatigue cracks throughout a component. Fatigue failure occurs when a fatigue crack is large enough to induce fracture of the remaining material ligament. For situations when cyclical loading is of constant stress amplitude (σ_a) (see Figure 2.14), the number of repeated cycles to failure is considered to be the fatigue life (N_f) of a component. As σ_a gets reduced, N_f typically increases. At σ_a well below σ_y , N_f might even seem infinite ($\sim 10^7$). This level is called the lower fatigue limit.

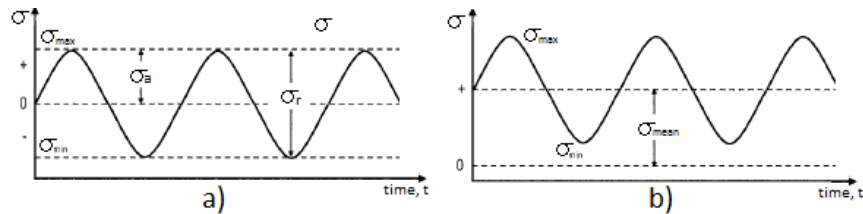


Figure 2.14: Types of constant amplitude cyclic loading [46]. a) Tension-compression with fully reversed constant amplitude loading. b) Tension-tension constant amplitude cyclical loading.

From Figure 2.14, it is important to define a few variables. The maximum and minimum σ applied to a component or specimen are expressed as σ_{max} and σ_{min} , respectively. From these, stress range (σ_r), stress amplitude (σ_a), mean stress (σ_m), and stress ratio (R) can all be easily calculated:

$$\sigma_r = \sigma_{max} - \sigma_{min} \quad (2.16)$$

$$\sigma_a = \frac{\sigma_r}{2} = \frac{\sigma_{max} - \sigma_{min}}{2} \quad (2.17)$$

$$\sigma_m = \frac{\sigma_{max} + \sigma_{min}}{2} \quad (2.18)$$

$$R = \frac{\sigma_{min}}{\sigma_{max}} \quad (2.19)$$

2.6.2 Mechanisms of fatigue failure

Fatigue cracks typically initiate at the outer surface of a specimen or component. Although σ_a may be much smaller than σ_y , small strains can still impart the movement of dislocations along preferential slip-lines. As can be seen in Figure 2.15, when dislocations pile up at surfaces, they can create extrusions and intrusions.

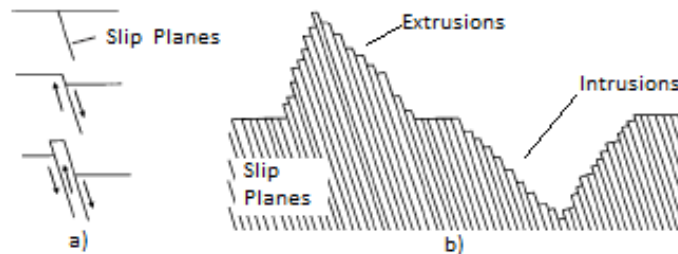


Figure 2.15: Early stages of crack initiation [46]. a) Piling up of step dislocations. b) Resulting extrusion and intrusion after multiple loading cycles.

Irregularities along the surface such as the ones depicted in Figure 2.15 introduce stress concentrations which amplify local stresses. This in turn can lead to the formation of fatigue cracks which can grow with each loading cycle. The evolution from crack nucleation into crack propagation is illustrated in Figure 2.16 where striations created by the advancement of a crack can be seen.

Crack growth is typically classified in two stages. Stage *I* immediately follows crack nucleation which stems from surface irregularities as depicted in Figure 2.15.

As can be seen in Figure 2.17, stage *I* can occur across one or multiple grains, dependent on material properties and particularly, d . During the first stage of crack growth, cracks do not necessarily propagate along a plane that is normal to the loading axis but rather along the weakest path. For most metals, the direction of crack initiation and growth in stage *I* occurs along planes of maximal shear stress.

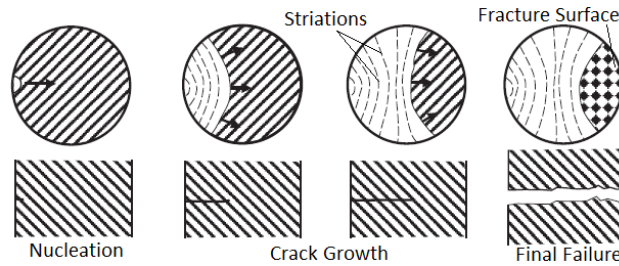


Figure 2.16: Typical propagation of a fatigue crack [47].

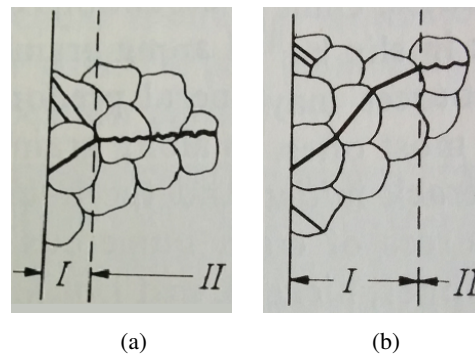


Figure 2.17: Schematic representation of the stages of fatigue crack growth in one grain (a) or several grains (b) [48]. Note that in both cases, loading is applied along the vertical axis.

Assuming that grains are randomly oriented, this explains why the crack changes orientation with each grain in stage *I* in Figure 2.17b. For materials with coarse grains, stage *I* might completely occur within one grain. Once the crack is large enough, stage *II* of growth dominates and cracks propagate along the normal plane to the applied σ . During this second stage of growth, cracks are also expected to grow a certain distance per cycle $(da/dN)^2$. For engineering applications where materials

²Conventionally, a represents crack length and N indicates number of applied cycles. Therefore, da/dN indicates the incremental change in crack length per cycle and is often referred to as the crack growth rate.

components are designed to resist fatigue, failure is expected well beyond stage *I* of crack growth.

2.6.3 Fatigue testing

Tests conducted in this project were conducted in load control. Although practical applications typically consist of loading with variable σ_a , fatigue behaviour is usually determined using fatigue tests with constant stress amplitude, as seen in Figure 2.14. Fatigue tests consisted of fully reversed cyclical loading with constant σ_a (see Figure 2.14), where $\sigma_{max} = -\sigma_{min}$ and R is necessarily -1. Regardless of the loading pattern, fatigue testing results are most typically presented with a Wöhler or Stress(S)-Life(N) curve, such as the example provided in Figure 2.18.

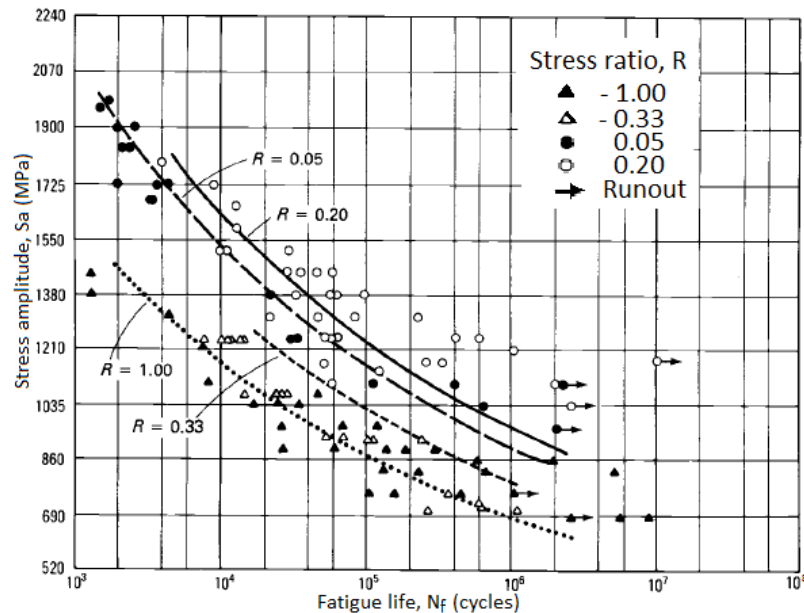


Figure 2.18: Stress-life curves that typify fatigue test results of un-notched 300M alloy steels [49].

As can be seen in this figure, R can have large effect on fatigue behaviour. In this case, the S-N curves for $R = -1$ is the lowest, indicating that fully reversed loading is the most damaging type of constant amplitude cyclical loading. Depending on testing frequency, long lasting tests can take a long time to complete. For this reason, it is quite common for tests lasting more than $\sim 10^6$ cycles to be stopped and for data points to be marked as a “run-out” data points (see Figure 2.18). As can be seen in the previous figure, at low σ_a , the difference between N_f of 2×10^6 and 3×10^6 can be

negligible when compared to the rest of the results and it might not be worth spending the extra days of testing to obtain the precision for that singular data point.

As can be seen in Figure 2.18, it is common for the slope of S-N curves to diminishes with reducing stress amplitudes, σ_a . Because testing beyond 10^6 or 10^7 becomes quite often untenable and because S-N curves tend to “flatten out” at this point, fatigue life is often termed infinite in this range. As can be seen in Figure 2.19, it is common practice to illustrate the “flattened out” curve as a purely horizontal line beyond what is deemed infinite life. The σ_a at which life seems infinite is commonly termed the fatigue limit or fatigue endurance of the material. For metals, this value is between 1/2 to 1/3 of σ_y .

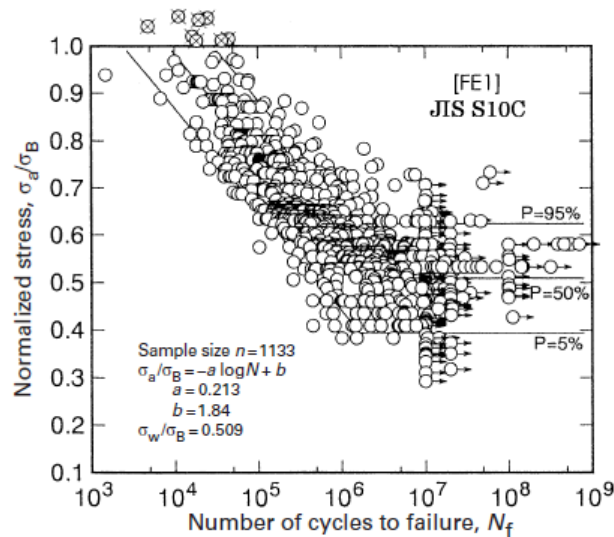


Figure 2.19: Example of fatigue scatter for a low-carbon steel where σ_a is the stress amplitude and σ_b , the ultimate tensile strength [50]. The lines labeled with P represent two standard deviations over the mean life prediction, assuming a log-normal data distribution.

2.6.4 Scatter in fatigue results

Microstructure can vary significantly throughout a material sample. For this reason, da/dN is expected to vary, and resulting N_f is expected to differ between specimens. For this reason, in order to obtain a certain degree of statistical representation, it is necessary to obtain an adequate number of data points. As can be seen in Figure 2.19, data scatter might be significant.

2.6.5 Fatigue of Galfenol

Galfenol is considered for sensing and actuating designs that would likely require cyclical loading, it is therefore necessary to discuss the material's fatigue characteristics. Considering the small range of stresses that accompany the λ_s limits of the material (~ 400 ppm), fatigue failure is not expected to be a concern for most actuating or sensing applications. That being said, for designs that require cyclical applications of larger σ_a , it is important to take into account material fatigue characteristics.

Thus far, the only research published on the effects of cyclical loading on the behaviour of Galfenol is that of Slaughter *et al.* [51]. Their work evaluated the effect of repeated loading on the effectiveness of stress annealing (see Section 2.3.2) and were not aimed at documenting fatigue behaviour. Although the experiments included cyclical loading, σ_a were relatively small, only 55 MPa, and were not designed for or significantly large enough to map out a full S-N curve. Furthermore, specimens used in their study did not comply with ASTM standards for axial loaded fatigue testing [52]. Consequently, because grip ends were machined with stress concentrating threads, many specimens failed prematurely in the grip sections, with fatigue cracks emanating from the threads.

2.7 Porosity

Porosity is well known to reduce mechanical properties of metals. The same is also true for cyclical loading applications where fatigue can be a concern. This section will introduce key concepts involved with porosity and will summarize some of the key research regarding porosity effects on mechanical properties of metals and fatigue behaviour.

2.7.1 General

Material voids or pores are usually qualified as being either isolated or interconnected. Pores can also be classified as being either surface-connected or internal to a component. Because pore shapes are not necessarily spherical, a useful measure of averaged pore size as observed along a given plane is that of the Feret mean diameter (D_f), a parameter consisting of the ratio between the pore perimeter and π . For describing overall or bulk pore content, porosity (P) is the measure of the total volume occupied by voids in a component. D_f and P are defined by the following equations:

$$D_f = \frac{\text{perimeter}}{\pi} \quad (2.20)$$

$$P = 1 - (\rho_{th}/\rho) \times 100\% \quad (2.21)$$

where ρ_{th} represents a material's theoretical density and ρ , its actual density.

Pores are most commonly found in cast or sintered P/M alloys. Because P generally has quite a deleterious effect on mechanical properties of metals, studies concerning the effects of porosity have generally been conducted on alloys manufactured by these two processes.

During the sintering process, gaps between powder particles typically result in the creation of inherent porosity. Pore shape and dimension in sintered metals is related to the dimension of P/M particles as well as the sintering conditions. For cast metals, the main mechanism of pore formation consists of gas entrapment. Although gas molecules that are diffused in solution with the molten metal may lead to microscopic pores called *pin holes*, the much larger and more damaging pores introduced in cast metals are typically caused by gas entrapment in the castings.

These entrapped spherically-shaped gas bubbles, called *blowholes*, have a relatively smooth inner surface. If cooling rates of the casting process are slow enough, *blowholes* are known to float towards the top end of the casting mold. *Blowholes* are also known to get entrapped near the outside of cast materials where cooling rates are necessarily larger than near the centre of the casting.

Two other factors that are known to contribute to porosity is material shrinkage during the casting process and the formation of Kirkendall voids when alloys are submitted to high temperatures. Material shrinkage may lead to the formation of voids when cooling rates are not consistent throughout a component. For the example of a cast component, slower cooling rates near the center of the component may lead to a lack of material flow and subsequently, the formation of internal gasless pores. Kirkendall voids are created in alloy metals when the application of heat, such as the temperatures achieved during welding, entice unequal rates of diffusion between elements. Areas with higher concentrations of the element with the higher diffusion rate will often result in the formation of Kirkendall voids with the application of heat under the right conditions.

Porosity testing can be categorized in four classes:

- i Pore detection tests: Such techniques make pores visible for observation, measurement, and counting. This category includes *in situ* testing with use of corrosive products to aid in contrasting pores and radiography techniques.
- ii Porosity index tests: These techniques provide a direct numerical measure of pore size and placement.
- iii Microscopic techniques: This type of approach permits direct observation of pores using various types of microscope.
- iv Density measurements: This approach provides bulk or average ρ values for a given specimen or component.

2.7.2 Effects of porosity on mechanical properties

Over the last decade, Hardin and Beckermann [53] have evaluated many of the effects that porosity can have on the structural properties of steels. In some of their earlier work, they demonstrated that the elastic modulus (E) of steel decreases non-linearly with increasing porosity. They proposed that E of a porous steel is dependent on the stiffness of the non-porous material (E_o) and its porosity (P) according to the following relationship:

$$E(P) = E_o(1 - 2P)^{2.5} \quad (2.22)$$

More recently, Hardin and Beckermann [54] demonstrated that increases in volumetric porosity decreased ductility in cast steels. Using A216 Grade WCB steel which has σ_y and UTS of 248 and 485 MPa, respectively, similar to that of Galfenol, the two researchers demonstrated that as little as 0.1% porosity could reduce ductility from 22 %EL for non-porous material to 12.8 %EL for porous cast steel. In their study, it was also found that pore shape and pore distribution within the specimens also affected mechanical properties.

Fleck and Smith [55] assessed the effects of porosity on the mechanical properties of a low alloy sintered P/M steel. They determined that a 5% decrease in ρ could reduce UTS of sintered steel from 400 MPa to 350 MPa and reduce 0.2% offset σ_y from 300 MPa down to 270 MPa. As can be seen in Figure 2.20, reductions in ρ also resulted in a significant increase of da/dN . Bourcier *et al.* [56] documented similar effects of reduction in ductility and strength for Ti alloys.

2.7.3 Porosity effects on fatigue

In addition to affecting ductility, stiffness, and strength of a material, porosity can also greatly affect fatigue behaviour of materials. Pores are well known to introduce stress concentrations upon loading. The stress concentration factor (K_t) consists of the ratio between the localized σ and the far-field stress, σ_{loc} and σ_o , respectively. As can be seen in the following equation, K_t is also dependent on pore or flaw dimension (a)³ and flaw tip radius (ρ_t).

$$K_t = \frac{\sigma_{loc}}{\sigma_o} = 2 \left(\frac{a}{\rho_t} \right)^{1/2} \quad (2.23)$$

Although stress concentrations dissipate away from flaws, closely packed pores may observe overlapping stress amplifications. This overlapping effect might lead

³By convention, internal flaws are considered to have a length of $2a$ and surface connected flaws have a length of a .

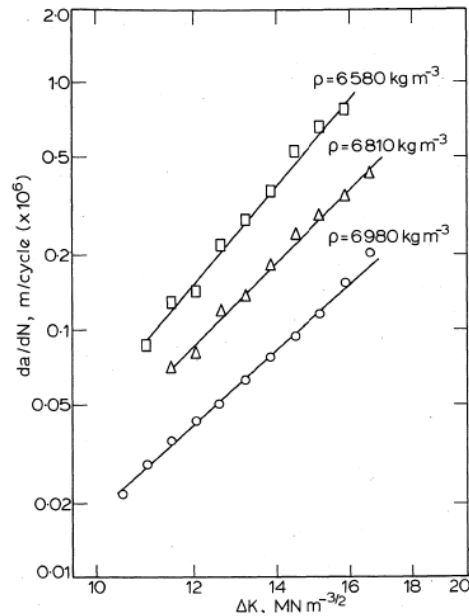


Figure 2.20: Density effect on the crack growth propagation of sintered steel ($\text{FeNi}_{1.75}\text{Cu}_{1.50}\text{Mo}_{0.50}\text{C}_{0.50}$). ΔK indicates the stress intensity factor range [55].

to further stress amplifications, which in turn may also reduce a porous component's fatigue life. The other reason closely packed pores might lead to fatigue life reduction is that once crack initiation occurs, multiple cracks emanating from various pores may grow into one another, hereby introducing sudden jumps in da/dN . Thus, pores may also be considered as crack growth precursors.

Holmes and Queeney [57] evaluated how much the overlapping and precursor factors contributed to the deleterious effect on fatigue behaviour. Their work was conducted on AISI 4625 steel and they concluded that fatigue crack initiation was directly dependent on the overlapping stress concentrating effect of closely packed pores. The precursor effect also contributed to reductions in fatigue life but was deemed secondary.

Sigl *et al.* [58] also evaluated the effect of porosity on the fatigue behaviour of quenched and tempered cast 8630 steel⁴. As described in ASTM standards E446 [59], rejection of cast components due to unsatisfactory levels of porosity is surprisingly subjectively assessed. Consequently, Sigl *et al.* also used a qualitative assessment of their radiographs to classify porosity. They established that porosity in their cast specimens was *microporous* when pores were not detectable (ap-

⁴Alloy compositions with Fe in wt%: $\text{Mn}_{0.93}\text{Si}_{0.66}\text{Ni}_{0.50}\text{Cr}_{0.48}\text{C}_{0.29}\text{Mo}_{0.27}\text{Al}_{0.045}\text{S}_{0.022}\text{P}_{0.027}$

proximately 2–20 μm), and *macroporous* when pores were visible (up to 200 μm). Specimens with macroporosity were further classified as being *least*, *middle*, or *most* porous. Shown in Figure 2.21a, microporosity had little effect on the fatigue life of cast 8630 steel whereas macroporosity had a significant effect.

Figure 2.21b provides a closer look at the fatigue results of the macroporous fatigue specimens. It was found that surface area porosity for specimens deemed to be macroporous ranged between 2.2–30.9%. Image analysis of the fracture surfaces of three macroporous specimens indicated that fatigue cracks all originated from macropores of approximately 200 μm in diameter. As well, increases in macroporosity were accompanied with increases in data scatter and decreases in N_f .

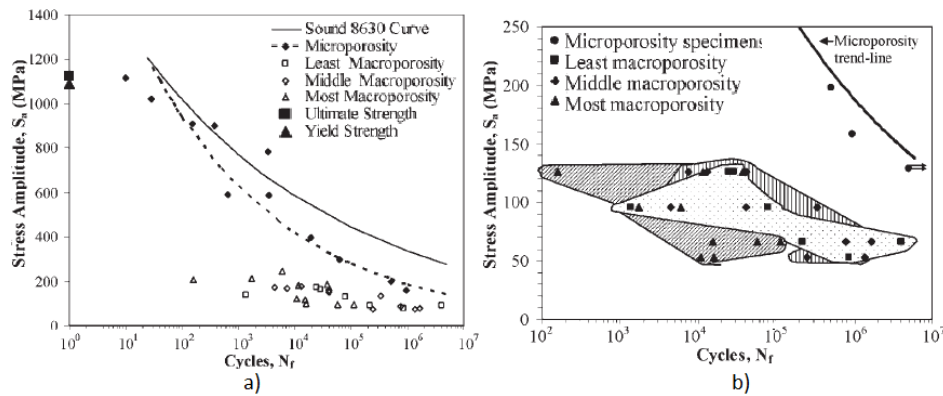


Figure 2.21: Porosity effect on the fatigue behaviour of quenched and tempered cast 8630 steel [58].

Having mentioned that sintered steels are also renowned for possessing porosity, Chawla and Deng [60] demonstrated the effect of porosity on fatigue behaviour of sintered low alloy $\text{FeMo}_{0.85}\text{NiC}$ steel. As can be seen in Figure 2.22, they showed that a 6.7% reduction in ρ reduced N_f by 46%.

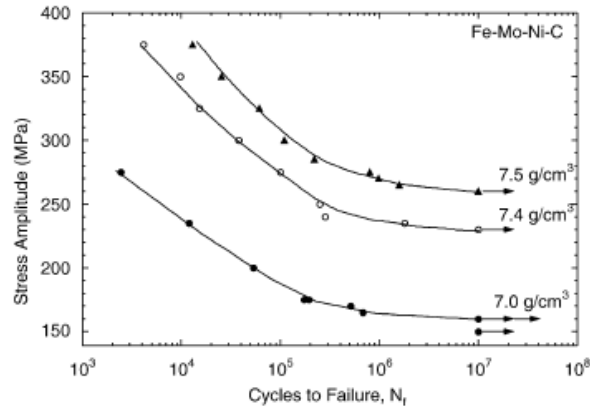


Figure 2.22: Stress-life fatigue curves of porous sintered steel ($\text{FeMo}_{0.85}\text{NiC}$) [60].

2.8 Grain size effects on mechanical properties

It has been well documented that increases in d have a negative effect on the mechanical properties of metals [15, 61]. This phenomenon is explained by the fact that grain boundaries hinder the movement of dislocations and in the case of cyclic load applications, can delay or stunt the propagation of fatigue cracks. In terms of the effects of d on mechanical properties, one of the most referenced empirical equation is the Hall-Petch Law [15], which relates the material σ_y to d :

$$\sigma_y = \sigma_o + k_y d^{-1/2} \quad (2.24)$$

where σ_o is the material property which represents its inherent ability to resist the motion of dislocations, and k_y is the strengthening coefficient or unpinning constant⁵.

As discussed earlier, and well documented by Kellogg [4], binary Galfenol has been shown to produce d well above 1 mm in diameter, even with C additions which help reduce grain growth in Galfenol by nearly a factor of two (see Figure 2.11). Regardless of the accuracy of the Hall-Petch equation, increases in d up to the order of 1 mm are expected to result in significant reductions in σ_y . Also mentioned earlier, Ga contents at or above ~ 17 at.% are known to be prone to intergranular fracture [18].

⁵This equation only applies at relatively low temperatures, below 40% of T_m (about 300 °C for Galfenol) and for materials with grains larger than 100 nm.

2.8.1 Grain size effect on fatigue of metals

In addition to reducing material σ_y , increases in d have also been shown to negatively affect fatigue behaviour of metals. In 1970, Armstrong [61] showed that quite similarly to the Hall-Petch equation, the fatigue limit also varied linearly with the $d^{-1/2}$.

Craig and Sinclair [62] were some of the first researchers to assess this effect. In their study on α -brass, they confirmed that the fatigue limit was increased with decreasing d . As can be seen in Figure 2.23, the relationship between the fatigue limit and $d^{-1/2}$ obtained in their results is linear, which is consistent with a Hall-Petch relationship (equation 2.24).

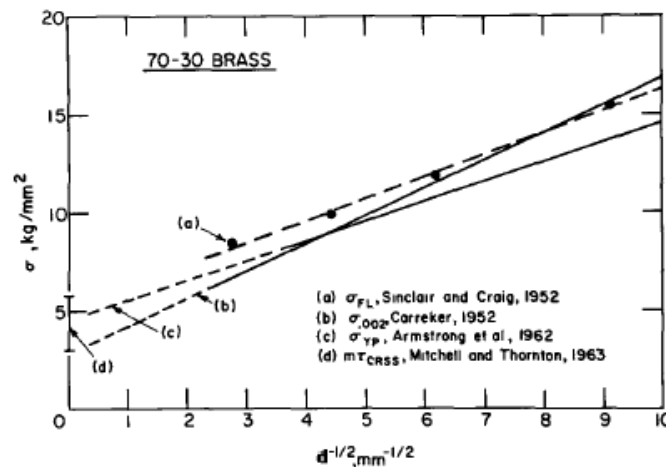


Figure 2.23: Fatigue limit and yield stress and grain size (d) for cartridge brass [62].

A few years later, in 1971, Thompson and Backofen [63] published results on the effects of d on fatigue characteristics of brass, copper, and Al. Results from their tension-compression fatigue tests are presented in Figure 2.24. It is important to note that various d were tested and that fatigue strength for these metals also decreased with increasing d .

Hersymchuck [65] evaluated the effect of d on a titanium (Ti) alloy and found that d increases also had a deleterious effect on fatigue behaviour. Results from his research on VT3-1 Ti alloys with varying d are summarized in Figure 2.25.

As established in the previously cited references, fatigue and other mechanical properties of metals are negatively affected with increases in d . The same holds true for Fe-based alloys. In 1965, Klesnil *et al.* [66] showed that fatigue limit of mild steel was linearly dependent to $d^{-1/2}$, in agreement with the relationship shown in Figure 2.23 and equation 2.24.

2.8. Grain size effects on mechanical properties

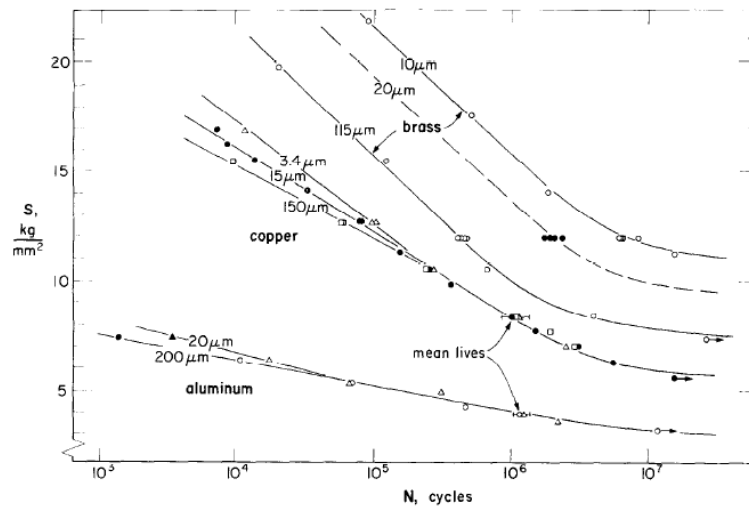


Figure 2.24: Stress-life curves for various metals with different grain sizes (d). Tests near the 10^6 cycles for copper and aluminum are only indicated by their mean lives and 95% confidence limit [63]. Solid symbols for Al were obtained from Boettner *et al.* [64].

Grain boundaries are known to stunt or at least delay crack growth. For this reason, it has been proposed that the main mechanism which determines fatigue life is not necessarily the amount of stress required to propagate a crack within a grain but rather the amount of stress required to propagate a crack across a grain boundary [67]. As materials with larger grains possess fewer grain boundaries, cracks are expected to progress relatively unhindered and overall fatigue lives are expected to be shorter.

The increase in fatigue life with decreasing d can also be explained by the fact that grain boundaries hinder the motion of dislocations, therefore limiting the formation and size of slipbands. This in turn can greatly enhance the number of cycles required to initiate a crack or to propagate a new one at a grain boundary. The theory that slip bands were arrested at grain boundaries was confirmed by Klesnil *et al.* [66] in 1965 in their work on low-carbon steels.

Ten years later, Taira *et al.* [68] assessed the effect of d on the fatigue behaviour of low-carbon steel. While conducting constant amplitude fatigue tests with $R=-1$, similar to those conducted in this study, propagation lives for specimens with average d of 7.8, 20.5, and 55 μm were 39, 4.4, and 2.6 $\times 10^5$ cycles, respectively.

Figure 2.26 shows that a similar study conducted by Jarvenpaa *et al.* [69] on 5.5 mm thick sheets of type 301LN austenitic stainless steel yielded similar results. The various microstructures were obtained by application of different heat treatments.

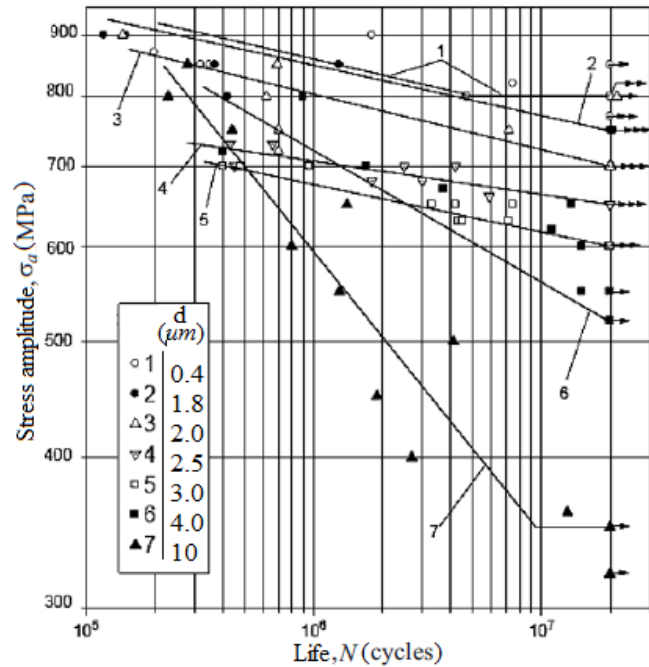


Figure 2.25: Stress-life fatigue curves for VT3-1 titanium alloy. Series 1 through 7 represent the increasing d , from 0.4–10 μm . Obtained from Herasymchuk [65].

While heating and cooling rates were constant at 200 $^{\circ}\text{C}/\text{sec}$, increasing grain coarseness was obtained by increasing peak temperature and holding time from 750 $^{\circ}\text{C}/0.1$ sec, to 800 $^{\circ}\text{C}/1$ sec, and 1000 $^{\circ}\text{C}/100$ sec, for partial reversal (PRev), complete reversion (Rev), and coarse-grained austenite (CGA), respectively. Resulting d for the three categories of specimens ranged in size from $d = 1.3$ and 1.6 μm for PRev and Rev, up to 14 μm for CGA.

2.8.2 Stages of crack growth in large grains

As is the case for Galfenol, if grains are large enough and stage *I* of crack growth occurs predominantly within a single grain, then there are no grain boundaries to retard crack growth. For the case of high Ga content Galfenol known to be brittle, preferentially oriented grain boundaries might act as crack growth precursors and promote premature crack propagation. As material brittleness is usually accompanied with low fracture toughness, it is possible that relatively short fatigue cracks are required for Galfenol components to fail by fracture. Ultimately, large grains and the brittle nature of Galfenol are two factors that can be deleterious to fatigue behaviour.

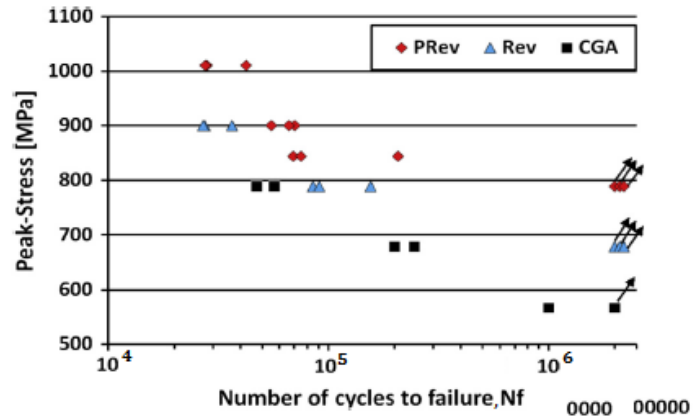


Figure 2.26: Stress-life fatigue data for various grain sizes (d) of stainless steel [69].

As discussed by Nolting [43], alloying additions and carefully selected heat treatments can help reduce grain growth in Galfenol steels, leading to improved strength, fracture toughness, and fatigue behaviour. Having assessed the effects of C, Mn, Cr, and Al, she determined that all of the elements could improve mechanical properties. As with C additions, Li *et al.* [70] showed that up to 1 at.% alloy additions of molybdenum helped offset embrittlement caused by Ga additions. As is the case with all other metals, alloy additions can therefore be used to modify Galfenol's inherent mechanical properties and texture.

2.9 Summary

The preceding review has shown that Galfenol steel is a highly magnetostrictive metal alloy which also possesses steel-like mechanical properties. In order to maximize profitability, bulk Galfenol must be manufactured in the polycrystalline form. In order to maximize cost of production whilst retaining as much of the material's magnetostrictive potential, one of the most utilized processes is directional solidification. As the development of a tough magnetostrictive metal has spurred the onset of many novel actuating and sensing designs that require cyclical loading, it is necessary to better identify this new metal's fatigue behaviour.

Given the exposure to high temperatures and the associated temperature gradients introduced during extraction and cooling, much like cast metals, DS materials are prone to inherent porosity. In order to maximize the cubic texture so heavily relied upon to produce λ_s , extraction rates of DS Galfenol are slow, approximately 100 mm/hr. Long exposures to high temperatures have also been associated with

macroscopic grain growth in DS Galfenol steel.

Furthermore, the high Ga content required to maximize λ_s has been shown to be the cause of material embrittlement. Seeing as large grains, low fracture toughness, and the presence of macroporosity are all known to reduce fatigue resistance of metals, it is expected that DS Galfenol will not be optimized for fatigue resistance. As mentioned earlier, one of the project objectives is to quantify the effect of porosity on the fatigue behaviour of Galfenol.

3 Materials and Methodology

3.1 General

As initial fatigue results were highly scattered, material density and pore geometry were analyzed before and after hot isostatic pressing of the alloys before further fatigue tests were conducted.

3.2 Materials

Galfenol steel with trace C contents (Fe-Ga-C) of approximately 0.15 at.% was selected for this project due to its enhanced mechanical properties over pure binary Galfenol [18]. In all, three alloys were tested and specimen labels were F, C, and M series for $\text{Fe}_{81.6}\text{Ga}_{18.4}$, $\text{Fe}_{82.8}\text{Ga}_{14.9}\text{Cr}_{2.2}$, and $\text{Fe}_{87.4}\text{Ga}_{12.4}$, respectively. FH and CH series are simply F and C series Galfenol processed by HIP. ETREMA Inc manufactured the samples using a modified Bridgman DS method (see Section 2.4).

3.3 Specimen preparation and preliminary tests

The as-received Galfenol samples were 125 mm long and 24 mm diameter Bridgman rods. In order to maximize the use of the as-received material, each rod was machined to produce eight fatigue specimens. In order to accomplish this, each as-received rod was quartered and machined into four 125 mm long cylindrical rods with a 8.73 mm diameter. Such an intermediate rod that fractured during machining can be seen in Figure 3.1.

The ρ of the intermediate rods were measured by water displacement. The steps and procedures used for determining ρ are included in Annex A. After ρ measurements and HIP (if applicable) were completed, each intermediate rod was further machined into two fatigue specimens. A photograph of an as-received sample and a completed fatigue specimen is included in Figure 3.2. Fatigue specimens were ma-

3.3. Specimen preparation and preliminary tests



Figure 3.1: Brittle fracture of a 8.73 mm diameter cylindrical Galfenol rod machined from a quartered as-received sample.

chined in accordance with ASTM standard E466 [52] and specimen dimensions can be seen in Figure 3.3.



Figure 3.2: As-received Galfenol sample and fatigue specimen.

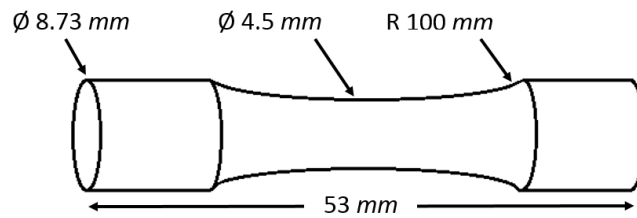


Figure 3.3: Fatigue specimen dimensions.

3.3.1 Hot iso-static pressing (HIP)

As can be seen in Figure 3.4, some of the intermediate cylindrical rods possessed significant surface connected porosity. Further metallographic observations showed that macroporosity was also present throughout the material. To remove the porosity, it was decided to process the remaining twenty-two 125 mm long intermediate rods by HIP. Processing conditions were maintained at 310 MPa and 1250 °C for a duration of four hours in an inert argon gas environment. These conditions were selected in consideration of published T_m [26], σ_y for Fe-Ga alloys [4], and recommendations from ETREMA Inc. [Summers, personal communications, 2013].



Figure 3.4: Visible surface-connected porosity on Galfenol rods.

Due to the surface porosity being visible on the majority of the machined intermediate Galfenol rods, it was decided to encapsulate the 125 mm rods in stainless steel capsules. These tubes were designed to plastically deform at selected HIP conditions while remaining impermeable to argon. The Bodycote HIP chamber was over 1 m in length and approximately 20 cm in diameter. The chamber was therefore large enough to process all twenty-two rods in one HIP operation. To achieve this, up to six rods were encapsulated together within the same stainless steel capsule (see Figure 3.5). Low-carbon steel plugs were placed between the Galfenol rods to keep the rods separated during HIP and to facilitate separation after the HIP operation.

After HIP, the capsules were plastically deformed and pressed onto the Galfenol rods. The stainless steel capsules could therefore only be removed by machining. The length of each rod and steel plug separator was known, so it was relatively easy to machine off each 125 mm long Galfenol rod.



Figure 3.5: Encapsulated Galfenol rods as-received after HIP operation.

3.3.2 Post-HIP specimen preparation

Once machined, the hardness of each specimen was determined using a Rockwell B test. Three tests were done near the ends of the specimens, well within the grip section where surface damage would not affect fatigue behavior. Specimens were then sanded within the gauge section as per the recommendations in the ASTM standard E466 [71] to remove circumferential surface machining marks that could promote premature fatigue failure. A 400 grit sandpaper was installed on a mandrel at the end of a rotating drill and polishing of the gauge section occurred in a perpendicular fashion to the rotation of the drill press. This left a polished surface on the specimen with any residual scratches in the longitudinal direction.

Once tested for hardness and sanded, the gauge section diameter was measured with a Mitutoyo micrometer with a precision of 0.0001" (0.00254 mm). After three measurements, the average diameter of the gauge section was used to calculate the gauge cross section area. Subsequently, the load required to achieve the desired σ_a for testing could be calculated by using the following equation:

$$\text{Load} = \sigma_a \times \text{cross section area} \quad (3.1)$$

Once the diameter measurements were completed, the specimen gauge section was lightly polished along its length with emery paper to remove any marks introduced in the measuring process.

3.4 Fatigue testing

The procedures used to conduct the fatigue tests abided by the principles in the Fatigue Handbook [72] and ASTM standards [52]. The equipment used for conducting the tests consisted of a servohydraulic load frame, as seen in Figure 3.6, and a computer to control and monitor load cycle amplitudes and frequency. The electromechanical frame was equipped with a load cell as well as a linear variable displacement transducer (LVDT) to help monitor the stroke of the lower grip. A computer software (REX) was used to describe σ_a for each cycle, count total number of cycles, and to monitor error in the applied load.



Figure 3.6: Electromechanical loading frame used for fatigue testing.

3.4.1 Test conditions

All fatigue testing was completed at room temperature in load control with a R of -1 (see Section 2.6.3). The calculated σ_a ranged between 150 and 450 MPa. Given the number of available specimens, multiple tests were repeated at each σ_a . Initial tests were selected at a σ_a that was well below projected σ_y . The cyclic load frequency was limited to 20 Hz due to the mechanical limitation of the loading frame. The frequency was reduced to 10–15 Hz for tests with σ_a at or above 400 MPa to help reduce error in the loading amplitude. Ultimately, testing frequency was maintained as high as possible without inducing measured maximum σ_a errors beyond 3.5 MPa for each specimen.

Galfenol is an auxetic material that exhibits audible pings similar to “tin cry” when it yields. The wedge grip force in the testing apparatus is controlled by variable hydraulic grip pressure. Given the brittle nature of both F and C series Galfenol, it was necessary to limit the gripping pressure to avoid fracturing the specimens in the grip section. This was achieved by simply listening to the specimen during gripping and setting the pressure below the level at which first yielding occurred. Some specimens were used sacrificially during this process.

3.4.2 Test monitoring and interruptions

Once a specimen was mounted in the loading frame for testing, testing was initiated at low frequencies of approximately 5–10 Hz. The software used for controlling the fatigue test had a built-in learning algorithm designed to apply the target load and to minimize the error in applied loads. The software’s program accomplished this by adjusting the applied loading waveform cycle by cycle in response to the measured feedback from the load cell. While carefully monitoring reported maximum errors to verify that loading errors remained under 3.5 MPa, the frequency was steadily increased to 20 Hz. For many of the tests where σ_a was within 15% of σ_y , cycle frequency had to be kept closer to 15 Hz to limit loading errors to 3.5 MPa. Error reporting only occurred every one hundred cycles; therefore, it was important to apply changes slowly so as to maintain timely feedback. For all specimens, steady-state testing frequency was achieved at around around 1000 cycles.

Testing was usually continuous until the specimens failed. Failure was defined as the specimens breaking in the gauge section and separating in two pieces. Tests were monitored many times a day to ensure that maximum reported errors were maintained within acceptable limits. Monitoring for specimen with σ_a at or near 400 MPa was done every thirty minutes since failure was expected to occur after a few hours of testing, even if testing frequency was reduced from 20 Hz. Tests at lower σ_a spanned 5-14 days and required less frequent monitoring. Fatigue specimens that endured

over 10^6 cycles without failure were generally stopped and considered to be at the fatigue limit, although with time permitting, some specimens were allowed to run well beyond 10^6 cycles.

For some specimens, testing was interrupted when thunderstorms posed a threat of overloading electrical circuits within the testing apparatus. On such occasions, the fatigue test was paused, the specimen was removed from the load frame, and the entire system was shut down in order to protect vulnerable equipment. Fatigue specimens were placed in plastic bags to reduce unnecessary exposure to humidity or other sources of possible corrosion. The longest interruption was 24 hours. Results from these tests were not expected to be adversely affected by this event.

3.4.3 Yield stress

The load vs displacement outputs over the first few cycles were documented for tests with σ_a near the yield point of Galfenol. Based on the load cell and bottom grip LVDT output (see Figure 3.7 for an example), the specimen yield strain was approximated. It was assumed that the captured displacement occurred within the 50.8 mm gauge section.

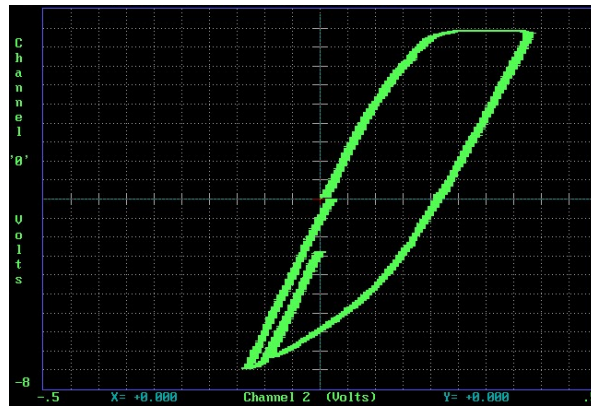


Figure 3.7: Voltage outputs for loading and stroke along the vertical and horizontal axes, respectively, for the first loading cycle on CH6.

3.5 Post-processing and analysis

Once failure occurred, the two specimen halves were removed from the testing equipment with particular attention to the preservation of the fracture surfaces. The two

specimen halves were taped together in parallel and the fracture surface ends were protected with the non adhesive side of tape to reduce contamination.

Fatigue data was compiled and gauge sections and fracture surfaces were observed with an optical microscope. A scanning electron microscope (SEM) was also used to observe the irregularities and 3D nature of the fracture surfaces. Both secondary electron (SE) and back-scattered electron microscope (BSEM) imaging were used to analyze fractured specimens.

3.5.1 Fracture surface observation

Fracture surfaces from at least six specimens from each series were observed under SEM. Specimens selected for observation were either relatively short or long lasting fatigue specimens. For each observed fracture surface, two initial SEM micrographs were captured encompassing the entire fracture surface. Some artifacts were more easily observed under BSEM therefore another micrograph of the entire fracture surface was also taken with BSEM. Additional micrographs with higher magnifications were taken of other artifacts and points of interest along the analyzed fracture surfaces. See Section 5.4 for examples of such micrographs.

3.5.2 Metallographic specimen observation

Metallographic samples were prepared with a goal of observing porosity and material texture. Using the same approach used for the analysis of fracture surfaces, specimens with relative short and long fatigue lives at various σ_a were selected for metallographic observation. In order to maximize the potential surface area available for observation, metallographic samples were obtained from the grip end of the fatigue specimens. One end was sectioned from the specimen and cut in half along its length (see Figure 3.8a).

From there, a belt sander with coarse sandpaper was used to grind the surface and produce a plane surface. Next, the specimen was mounted and cured in a phenolic pre-mold. Once cured and secured in the mould, the metallographic specimen was sanded with four varying grits of sandpaper and finally polished with diamond pastes ranging down from 6 μm to 0.05 μm for final polishing. The finished product can be seen in Figure 3.9.

3.5.3 Microporosity

Unetched polished specimens were found to be best suited for observation and analysis of porosity. The mounted and polished grip section halves provided a relatively large observation surface of approximately 8 mm \times 20 mm or 160 mm². Because a

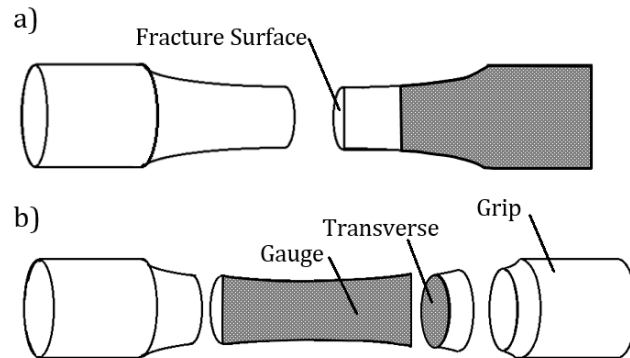


Figure 3.8: Specimen sectioning. a) Preparation for metallographic samples. b) Sectioning for texture samples.

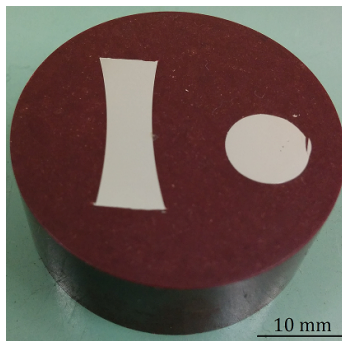


Figure 3.9: Polished metallographic specimen example.

relatively large surface area was prepared for each polished specimen, many micrographs were obtained from each specimen. Micrographs were taken with a Canon T3 Rebel Ti digital camera.

For each specimen, a minimum of six micrographs were captured. These six micrographs were later used to quantify pore sizes and distribution as well as total surface area porosity. Given that each micrograph captured 1.14 mm^2 of the polished surface area, the sum of the six pictures represented 6.86 mm^2 or approximately 5% of the total polished area. For each series of Galfenol, four specimens were analyzed this way. Therefore, analysis of porosity by micrograph was done over 27.45 mm^2 of Galfenol for each of F, FH, C, and CH Galfenol specimens. The resulting number, size, and total surface area covered by the pores are presented in the next chapter.

These results were obtained by processing the micrographs through Matrox image processing software. Through the manipulation of each micrograph, pores were

clarified, enhanced, and highly contrasted for ease of digital image analysis. A processed micrograph is presented in Figure 3.10. Application of the contrast levels to obtain a good representation of the original micrograph was somewhat subjective. This is discussed further in Section 5.3.

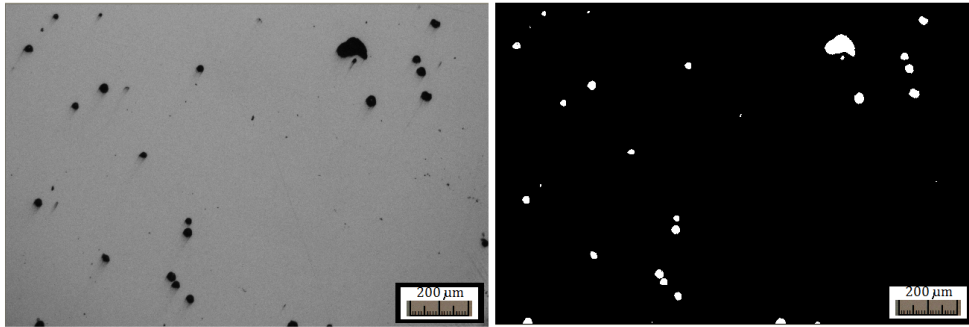


Figure 3.10: Example of image processing using Matrox software.

With such highly contrasted pores, Matrox Software was used to count the number of pixels in each pore, hereby determining its shape and size. The number of pixels in the micrographs were calibrated by comparing analyzed micrographs to the micrograph taken of a 1 mm calibration scale taken with the same magnification.

3.5.4 Material texture

Specimens that had not failed in fatigue were used for metallographic observation to determine the HIP effects on grain texture. These specimens were mounted on phenolic molds with the gauge section cut in half along its length (see Figure 3.8b). Additionally, the end of the gauge section, near the neck with the grip section, was also parted off to give a perpendicular view or a top down view of the gauge section.

These specimens were mounted, sanded, and polished using the same steps as the specimens prepared for observing microporosity. A 5% Nitol solution was used as an etchant. Once the specimens were satisfactorily etched, micrographs of grain structure along the gauge length and across the gauge diameter near the grip end were taken. Examples of such micrographs are included in Figure 3.11.

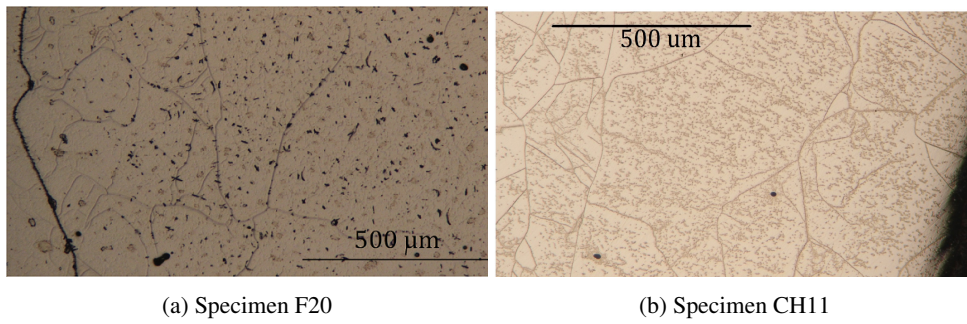


Figure 3.11: Grain texture as captured on etched metallographic specimens of F and C series Galfenol, subfigures a) and b), respectively.

4 Results

Experimental results that pertain to this project are presented in this section. Given that the main focus of this project was to analyze the effect of HIP on fatigue behaviour, fatigue data, arguably the most important results for this project, will be presented first. Following this, the effects of HIP on density and porosity will also be presented. The remainder of the experimental results is also included.

4.1 Fatigue results

Fatigue data for as-received F and C series specimens was obtained in prior research. Remaining intermediate rods were HIPed (see Figure 3.5) and then machined into twenty and twenty-four FH and CH series fatigue specimens, respectively. As-received samples of M Series were also acquired to help broaden the scope of this research project. Half of the as-received M series material sample was used to produce dogbone fatigue specimens.

Given that testing occurred in the spring/summer months, from May to September 2014, room temperatures at which the tests were conducted ranged between 20–30 °C, with an average of 25 °C. Tests were initiated at frequencies below 10 Hz. Within the first few hundred cycles, the testing frequency was increased and maintained at 20 Hz. Failure of the tested specimen was defined as full separation of the specimen into two parts. Figures 4.1 and 4.2 include comparison of the as-received and HIP fatigue data for both F and C series, respectively. Figure 4.3 includes a comparative depiction of as-received fatigue data for all three tested Galfenol series. In all three figures, arrows indicate run-on data, numbers indicate specimen labels, and the error on σ_a is smaller than the symbols used to depict the data.

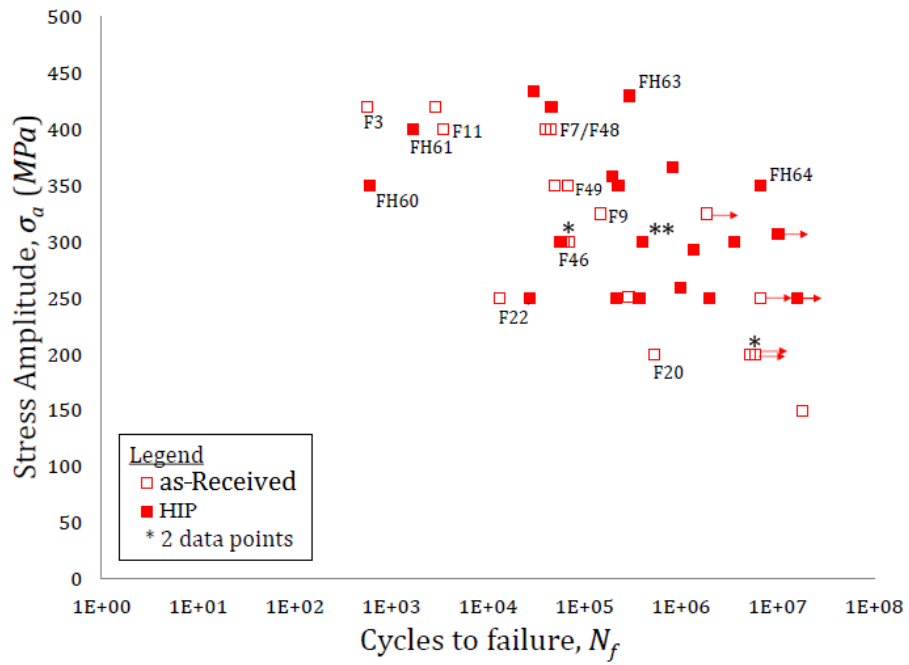


Figure 4.1: Stress-life results for as-received and HIP series $Fe_{81.6}Ga_{18.4}$ Galfenol, F and FH series, respectively.

** Note: HIP pressures for this specimen were only 193 MPa, far less than the remainder of the FH Series HIPed at 310 MPa.

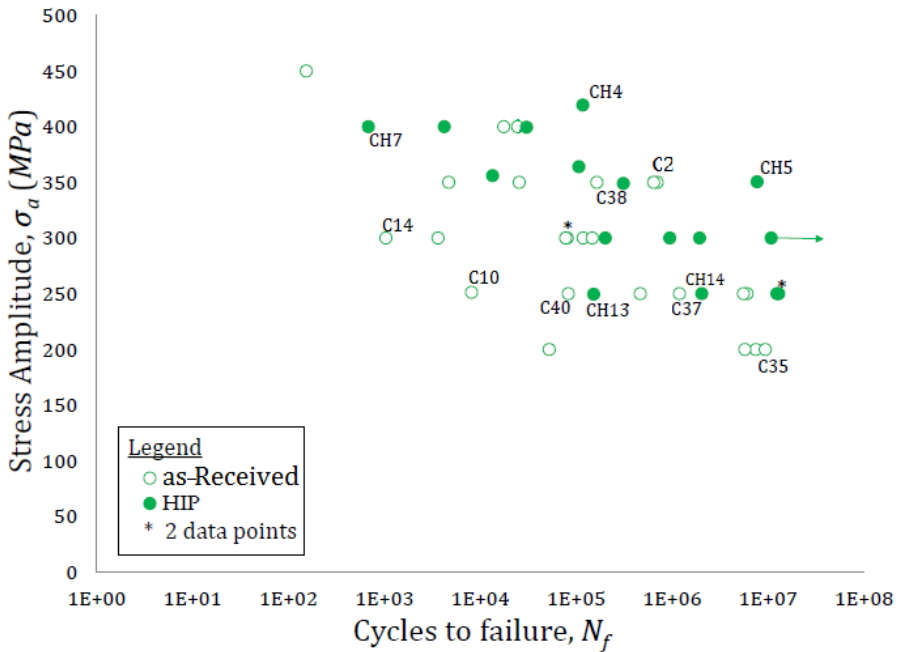


Figure 4.2: Stress-life results for as-received and HIP Fe_{82.8}Ga_{14.2}Cr_{2.2} Galfenol, C and CH series, respectively.

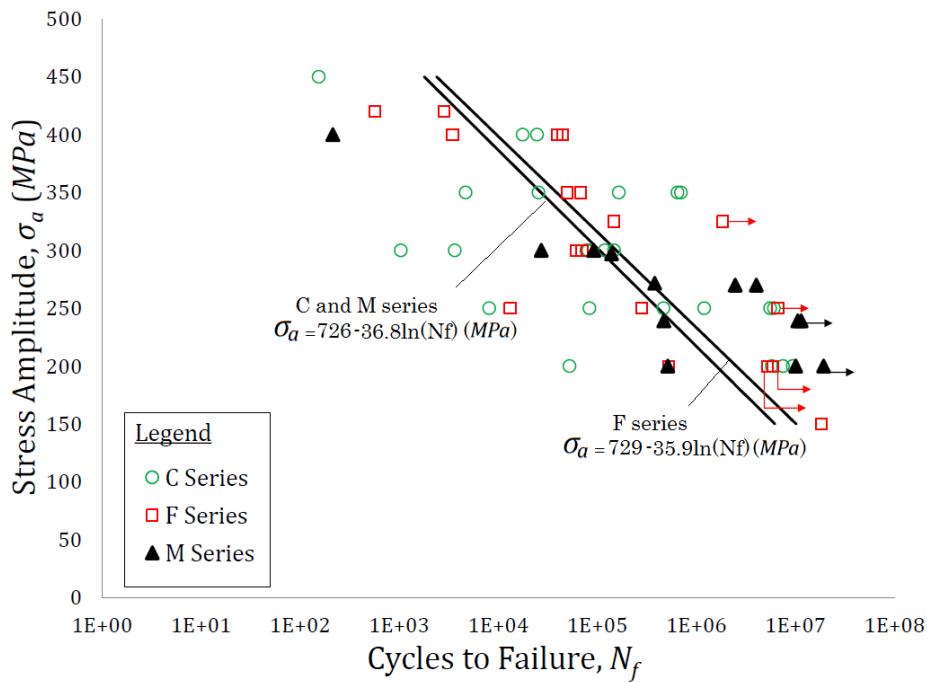


Figure 4.3: Stress-life test results for all three as-received Galfenol series with R = -1. The labeled lines indicate the mean S-N curves for each of the Galfenol series.

4.2 Density

As described in Annex A, Galfenol's ρ was calculated using the Archimedes water displacement principle. There were at least ten as-received rods with an average weight of 60 g and a bulk outer volume of $\sim 7.5 \text{ cm}^3$ used to measure density before HIP. Because the HIP Galfenol rods were encapsulated in a plastically deformed stainless steel casing (see Figure 3.5), it was necessary to remove the capsule by machining. Consequently, some of the material from the Galfenol rods had to be removed and it was decided to proceed directly to the machining of the fatigue test specimens.

At least twenty fatigue specimens (see Figure 3.2) from each Galfenol series of HIPed material were tested for ρ . These specimens weighed on average 19 g and had a bulk exterior volume of $\sim 2.5 \text{ cm}^3$. Table 4.1 summarizes the averaged ρ calculated for as-received and HIP materials. A theoretical density (ρ_{th}) of 7.97 g/cm^3 was used [73, 74] to calculate P (see equation 2.22).

Table 4.1: Material densities (ρ) and porosity (P) for as-received and HIP Galfenol. \pm represents one standard deviation and ρ and P are expressed in g/cm^3 and vol %, respectively.

Series	as-received		HIP		Change	
	ρ	P	ρ	P	$\Delta\rho$	ΔP
F	7.89 ± 0.05	1.07	7.96 ± 0.04	0.16	0.9%	-85%
C	7.88 ± 0.05	1.20	7.97 ± 0.04	0.04	1.1%	-96%
M	7.92 ± 0.06	0.68	—	—	—	—

The ρ_{th} used to calculate P was the only published value found and although it was for Galfenol containing 17 at.% Ga, it was adequate to approximate the P of the as-received material. Seeing as the actual ρ of the C and F series Galfenol might differ slightly from the quoted value, the calculated P in Table 4.1 is not necessarily accurate. What can therefore be obtained from these porosity calculations is the magnitude of the change in porosity measured by this method. A second and more accurate method of measuring porosity is described in Section 4.3.2.

4.3 Porosity

As introduced earlier in Section 3.5, it was expected that HIP would significantly reduce porosity in the as-received Galfenol. In turn, it was theorized that a reduction in porosity would improve fatigue life and reduce data scatter. Fatigue testing

requires multiple data points, therefore, it was deemed necessary to machine all the HIPed material into fatigue specimens to maximize fatigue data. Once the specimen failed in fatigue, or testing was stopped at or beyond 10^6 cycles, specimens were segmented so that large surface areas could be exposed for texture and porosity analysis (see Figure 3.8).

4.3.1 Pore size and pore size distribution

Once polished and etched, the metallographic specimens produced a good view of material texture by highlighting grain boundaries. Figure 4.4b shows the effect of etchant on the delineation and contrast level of the pores. Therefore, in order to properly quantify the level of porosity in the prepared metallographic samples, non-etched specimens were used (see Figure 4.4a). See Section 5.3.1 for a description of the effects of contrast on the porosity micrographs.

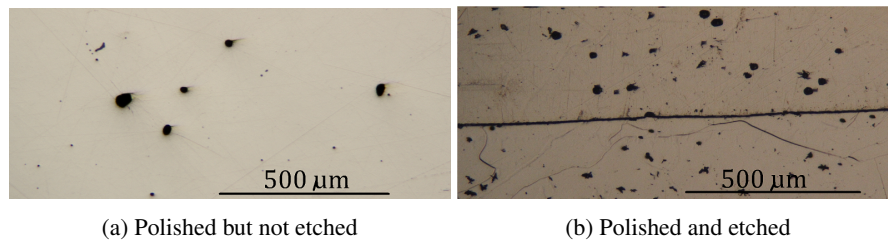


Figure 4.4: Effect of etching on Galfenol metallographic specimens.

For each prepared metallographic specimen, at least six pictures with an area of 1.144 mm^2 were taken along the grip section halves. For each material series, a minimum of four metallographic specimens were prepared. The resulting twenty four pictures were processed and analyzed with image analysis software and the resulting analysis on the sizes and number of pores for each Galfenol series is summarized in Figures 4.5 and 4.6.

4.3.2 Surface area porosity

Figures 4.5 and 4.6 provide information on the number of pores categorized by size, and the following figures represent porosity in terms of relative surface area porosity.

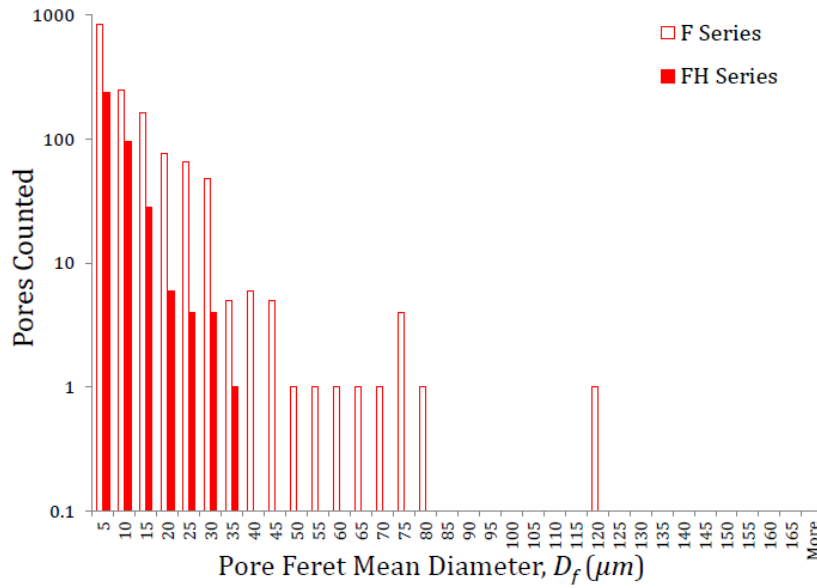


Figure 4.5: Number and size of pores detected in six micrographs (27.4 mm^2) of F and FH series metallographic specimens.

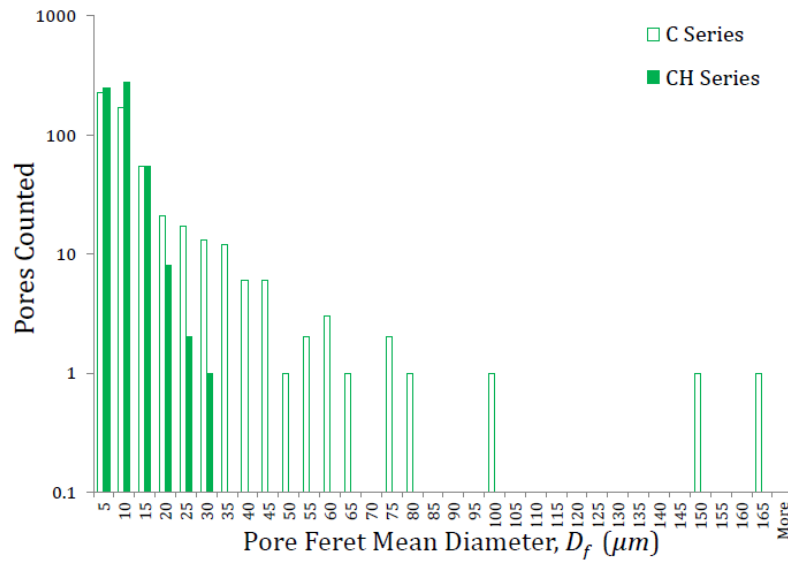


Figure 4.6: Number and size of pores detected in six micrographs (27.4 mm^2) of C and CH series metallographic specimens.

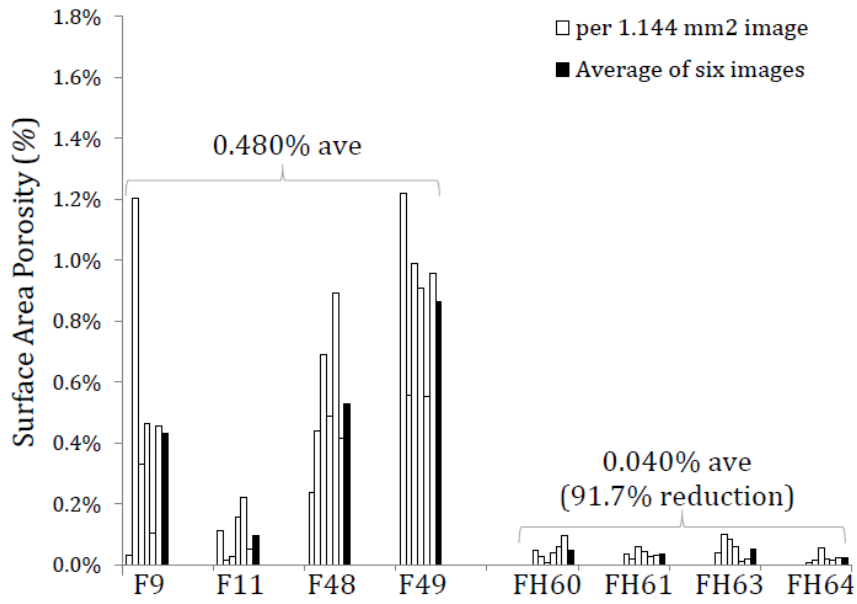


Figure 4.7: F and FH series relative pore surface area.

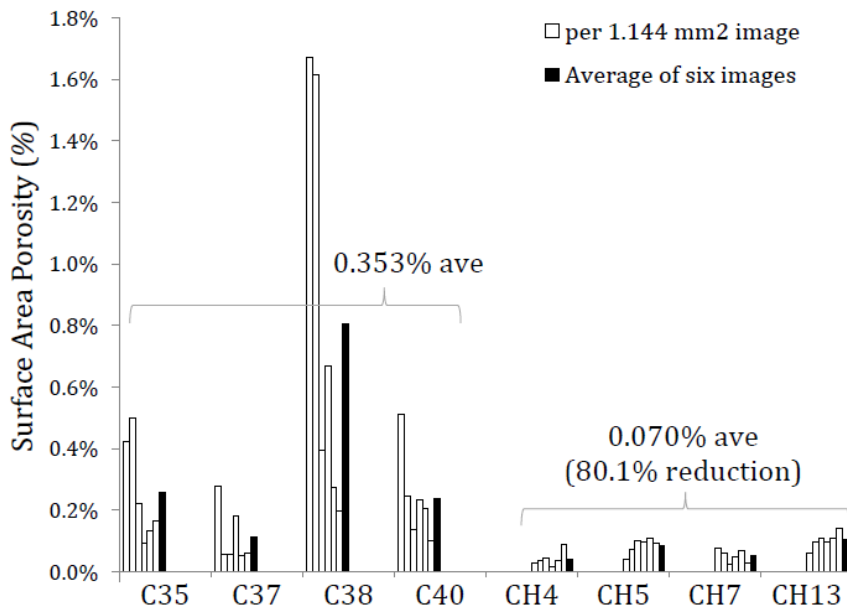


Figure 4.8: C and CH series relative pore surface area.

4.4 Hardness

As described in Section 3.3.2, material hardness was measured twice at each end of each specimen along the grip section surface. Hardness tests were conducted on a minimum of sixteen specimens for each series. For specimens which had grip ends sectioned off after testing, hardness testing was done on the plane surface of the inner grip (see Figure 3.8a). The measured hardness values for each Galfenol series are included in Figure 4.9, which gives both the numerical averages and one standard deviation as calculated from the measurements.

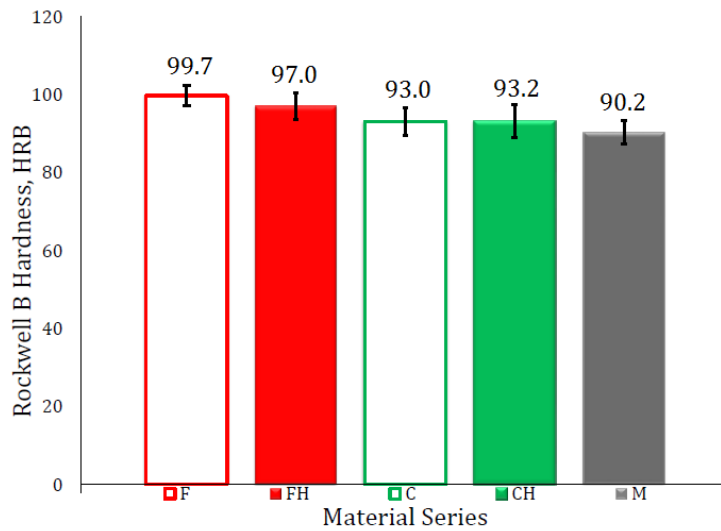


Figure 4.9: Material hardness for each Galfenol series tested.

4.5 Yield stress

Given that material and processing costs were significant, the limited quantity of HIPed material was used in its entirety to produce fatigue specimens. Although not abiding to ASTM standard testing techniques, fatigue specimens destined for testing at high or near σ_y were used to produce load–displacement curves over the first cycle of loading. Selected fatigue specimens were loaded manually up to the point of yielding, where material “crying” or pinging was audible. Load increments were about 10 MPa and strain rates were relatively low, about one order of magnitude lower than those imposed on the material during fatigue testing at steady state. Once yielding was heard or the material began to flow at the point of yielding, the load was

fully reversed until a full tension-compression cycle was completed. At this point, REX software was activated to automate testing and capture data for the remainder of the fatigue test. Examples of stress-strain paths up to yielding can be seen in Figure 4.10.

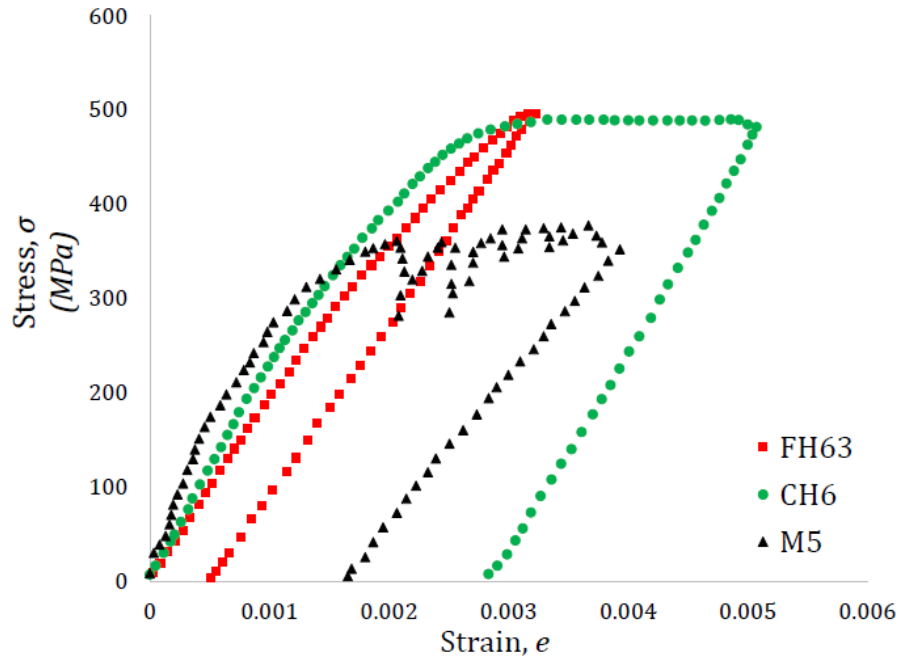


Figure 4.10: Stress-strain path from rest to yielding for the first half cycle of fatigue test. Note that strain is approximated.

As can be seen in Figure 4.10, the stress-strain path for a typical M series specimen differs significantly from that of the C or F series Galfenol. These results indicate that as expected, σ_y increased with Ga content. The softer M series Galfenol was found to yield at $375 \text{ MPa} \pm 20 \text{ MPa}$, the C series at $475 \text{ MPa} \pm 20 \text{ MPa}$, and the F series closer to 500 MPa. These values are in line with what has been documented for Galfenol, as mentioned in Chapter 2.

5 Discussion

5.1 Experimental approach

Similar to the observations made by Kellogg [4] in his early work on polycrystalline Galfenol, it was observed during testing that F and C series Galfenol samples were inherently brittle. Many of the intermediate rods and fatigue specimens fractured during machining. Overall specimen losses for F and C series Galfenol was approximately 10%. Considering that each as-received 125 mm Galfenol rod, which could produce eight fatigue specimens, cost over \$2500 and that HIP essentially doubled expenses, material losses were significant. The high material and processing costs limited the number of specimens that could be used for testing.

Kellogg [28] had also noted that the Galfenol specimens made audible pings when yielding. He concluded that sounds were likely caused by deformation twinning. Nolting [43] made similar observations while conducting tensile tests. Pinging was also heard in this project when specimens were pulled in tension to the point of yielding and when the fatigue specimens were wedged by the testing frame grips. Because this pinging or crunching sound is associated with material yielding, the amount of pressure applied to the fatigue specimen grip ends by the grip wedges was limited to the first audible sounds of yielding. As well, fatigue specimens tested at close to σ_y typically pinged during the first cycle or two of loading.

As mentioned by Brooks and Summers [18], high Ga content Galfenol is known to be inherently brittle at room temperature. Coincidentally, the M Series Galfenol with only 12.4 at.% Galfenol had relatively low hardness (see Figure 4.9), better machining characteristics, and did not fracture during machining.

From Figure 5.1 below, it is evident that macroporosity was visible in the as-received stock. Figure 3.4 shows that porosity was present in some of the intermediate rods. As initial fatigue results were so highly scattered (see Figures 4.1 and 4.2), and that macroporosity had been linked to reductions in N_f and increases to fatigue scatter, it was deemed necessary to reduce porosity before pursuing further testing.

Hot forging and hot rolling options were considered for removing porosity since these have been shown to effectively remove porosity [4]. That being said, because

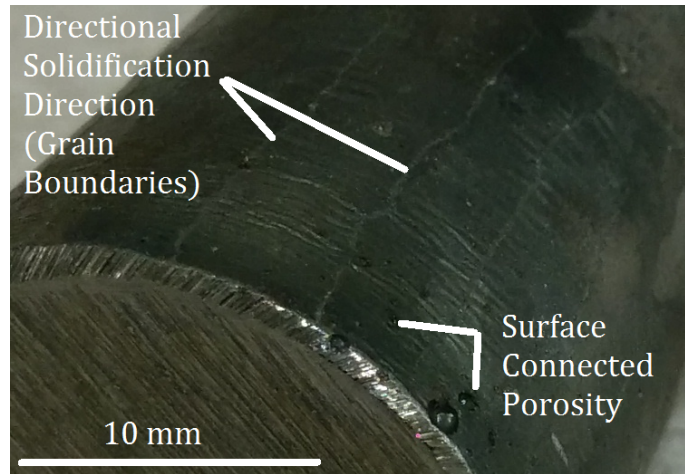


Figure 5.1: Macroporosity and visible grain boundaries on the as-received material (M Series).

as-received material tests were conducted on cylindrical specimens (see Figure 3.3), it was deemed necessary to preserve the as-received material texture and the specimen shape. HIP was therefore selected because it would help maintain overall shape, maximizing the number of cylindrical fatigue specimens that could be produced from the HIPed material.

5.2 Hot iso-static pressing (HIP)

Two 8.73 mm diameter and 125 mm long intermediate cylindrical rods from F and C series were shipped to NRC Canada and were HIPed at 193 MPa, the maximum pressure for that particular HIP chamber. These rods were HIPed without encapsulation and the final product was still visibly porous upon receipt. Half of the HIPed F series (or FH series) rod was fractured during machining and only one specimen could be machined. Its resulting fatigue life, shown in Figure 4.1, did not indicate change from the as-received results. Because the pressed C series rod was still highly porous, it was not used for testing.

Based on recommendations from ETREMA Inc. to maximize HIP effect, Galfenol specimens were then HIPed at 310 MPa and 1250 °C for a duration of four hours. Finding a HIP chamber that would use argon and that could achieve 1250 °C was relatively easy; machines that are robust and large enough to produce pressures beyond 200 MPa are rare.

The HIP chamber at Bodycote was the largest one found and produced pres-

tures of 310 MPa, much higher than the pressures achieved at DRDC. Given that the cylindrical HIP chamber was over one meter in length and approximately 20 cm in diameter, it was possible to press all of the Galfenol specimens in one HIP cycle. This ultimately helped save processing costs. According to the Galfenol binary phase diagram (Figure 2.8), it was expected that F series Galfenol would have the lower T_m of the two metal alloys. Melting was expected at around 1400 °C, and it was deemed prudent to HIP at a temperature of 1250 °C. In theory, a higher HIP temperature would make the densification process faster.

High Ga content Galfenol alloys became brittle with increasing Ga content [18] because Ga-rich deposits are expected to precipitate at grain boundaries and result in weakened intergrain cohesion. It is possible that heat treating at 1250 °C for a duration of four hours may have further increased the quantity of these Ga rich precipitates which in turn could have an effect on structural properties.

5.2.1 Encapsulation

As some of the machined samples possessed surface connected pores, as illustrated in Figure 3.4, HIP might not be effective if the material is not encapsulated before processing. Figure 5.2 shows that encapsulating specimens helps make surface pores effectively internal which in turn improves the effectiveness of the HIP process.

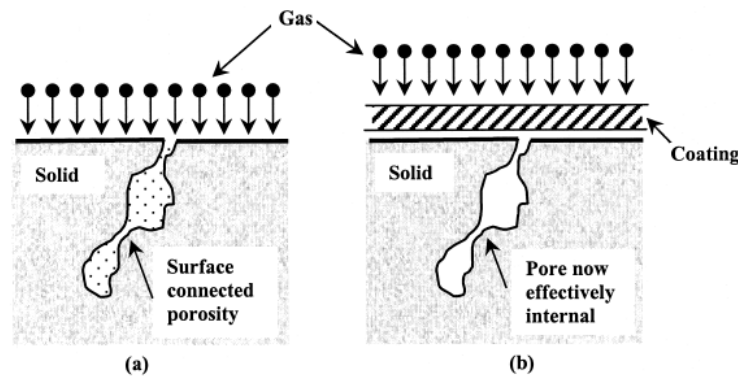


Figure 5.2: Effect of encapsulation on surface connected pores. a) The pressurizing medium impinges on the surface-connected pores as though it was an extension of the surface. b) After encapsulation, the surface-connected pores effectively become internal and can be closed if the pores are evacuated [75].

As shown in Figure 3.5, the Galfenol specimens were encapsulated in thin walled stainless steel tubes. Because the tubes are thin walled and ductile, the iso-static pressure effectively deforms the tube against the target specimens and transfers the pres-

tures radially to the Galfenol rods. Although multiple rods separated by low-carbon steel plugs were encapsulated together, diffusion of Ga, C and Fe was considered to be negligible.

In order to remove the Galfenol rods from the stainless steel capsules it was necessary to machine the tubes. It was difficult to delineate between specimens, plugs, and capsules as they are all Fe-based alloys. Luckily, as can be seen in Figure 5.3, the radial delineation between Galfenol specimens and low-carbon steel plugs along the length of the capsules was easily identifiable. It was intended for ρ of each individual rod to be measured before and after HIP. Unfortunately, the identity of the Galfenol rods was not preserved during the HIP process. This made it impossible to determine the ρ change of individual rods. However, averaged bulk density (ρ_{ave}) before and after HIP could still be compared.

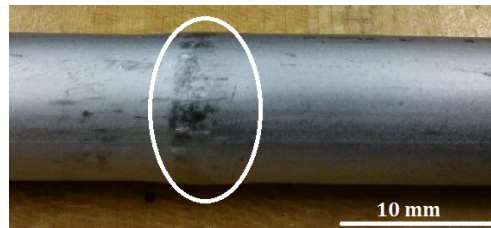


Figure 5.3: Example of the resulting plastic deformation caused by HIP. Sudden changes in diameter occurred along the stainless steel tube precisely where the low-carbon steel plugs were placed between specimens.

5.2.2 HIP effects on density

In order to quantify how successful the HIP process was going to be, it was deemed necessary to calculate material ρ before HIP. To obtain accurate results, the first options considered were to use either a mercury porosimeter or a gas pycnometer, both techniques used to procure outer envelope volumes of metal specimens. The former instrument uses liquid mercury displacement to permeate the surface connected pores and precisely measure the outer volume of each specimen. When compared to the specimen weight, the ρ can easily be calculated. Unfortunately, the only accessible porosimeter was not functioning and it would have been too long of a wait to have the instrument fixed.

Gas pycnometry was also considered for quantifying changes in ρ due to HIP. This technology uses pressure differentials from gas displacement to measure outer envelope volume of a specimen. For very porous materials such as sintered ceramics, this type of instrument can also be used to accurately measure bulk volume. As with

most metals, the majority of pores in Galfenol are isolated (see Figure 4.4b). Use of a gas pycnometer would be the preferred instrument for measuring the difference in ρ before and after HIP.

Water displacement

A gas pycnometer could not be procured for this research, therefore water displacement was selected as the next best option to determine ρ . Given the dimension and the level of P to be measured in the Galfenol specimens, the water overflow method as explained by Hughes [76] was used. The submersion method typically used for P/M components [77] is designed for specimens with less than 2% porosity, much less than the as-received Galfenol. Changes in ρ measured using this method were on the order of $90\% \pm 5\%$. As presented in Figures 4.7 and 4.8, the porosity reduction was evaluated at $85\% \pm 6\%$ using the visual analysis of the processed micrographs.

Overflow water displacement involves the transfer of water between containers. Due to this, there are many variables that can affect the degree of precision of the measured volume. The biggest variable which affected volume measurements was the fact that due to surface tension, some of the displaced water would remain in the overflow spout. As drops of water would continue to drop out of the tube for many seconds, a standard period of time was given for each measurement. Repeating this process was important because a simple drop of water affected the measured volume by 0.1%. The container used to collect the displaced water also had to be thoroughly dried between measurements so as to ensure that all the water contained was indeed displaced by the submerged specimen.

Dish washer rinse agent was also used as a surfactant for the measurements. Approximately 5 drops of rinse agent were applied per litre of deionized water. This amounts to about 0.01% volume content. ASTM B311 [77] states that up to 0.1% volume surfactant may be used for similar water displacement tests. Ultimately, the small quantities of surfactant used had negligible effect on the deionized water's ρ , a critical value for determining the volume of the displaced water. The ρ of the deionized water at the measured temperatures was obtained from ASTM Standard B311.

Density measurement results

Although there is a little discrepancy between the two techniques, results obtained by both processes indicate that HIP successfully removed porosity ($\sim 85\%$). The advantage of the liquid displacement technique is that it provides an averaged value for all the tested material, pre and post HIP. In order to obtain an averaged value for the bulk sample, analysis of many micrographs is required. Considering that twenty-

four micrographs were analyzed for each series, and that results were in line with averaged values indicates that both methods were likely accurate.

Though time consuming, the visual analysis approach does provide additional information that can not be obtained by liquid displacement. For one, it gives the researcher the ability to observe pores individually. It also provides information on the shape, size, and distribution patterns of the pores within the specimens. As can be seen in Figures 4.7 and 4.8, the degree of porosity varied significantly between specimens. For example, the porosity in C37 and C38 varied on average by one order of magnitude. This indicates that porosity in the as-received Galfenol samples was not evenly distributed, a typical phenomenon for cast and for DS components. This variation between specimens is likely a contributor to the data scatter observed in the fatigue results.

5.2.3 HIP effects on pore sizes

Figures 4.5 and 4.6 indicate that as-received material for both Galfenol series possessed macroscopic pores as large as 165 μm (see Figure 5.4). Additionally, and as mentioned in Section 3.5.3, polished and etched metallographic surfaces were also analyzed for further artifacts. Figure 5.4 illustrates that some of the pores observed within the metallographic specimens were nearly 1 mm in length.

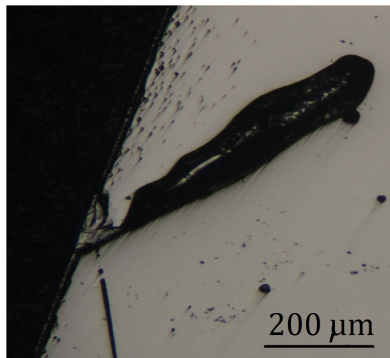


Figure 5.4: Large surface connected pore observed in specimen F49.

The HIPed specimens from either series had pores that were no larger than 35 μm . As mentioned in Section 2.7.3, Sigl *et al.* [58] had shown that microporosity had little effect on the fatigue behaviour of a porous cast steel. On the contrary, they had shown that macroporous specimens with pores as large as 200 μm have shorter fatigue lives. Assuming that the same would hold true for Galfenol, another Fe-based alloy, then one would expect for HIPed specimens to have notably increased fatigue lives over as-received material.

5.2.4 HIP effects on pore shape

So far, the only pore geometry parameter that has been discussed is the Feret mean diameter (D_f). From the principals of fracture mechanics, flaw shape and orientation also have an impact on stress concentrations. Seeing as the pores observed for this project were predominantly spherical, flaw orientation was not assessed. That being said, pore shape was considered. Taking an elliptical shaped pore as an example, stress concentrations arising from it would be larger if its long axis would be within the normal plane to the component loading axis. The opposite would be true if the ellipsis long axis would be parallel to the loading axis.

In order to quantify change in shape of the pores, the following equation was used to describe a pore geometry factor (PGF):

$$\text{PGF} = \frac{D_{\max} - D_f}{D_f} \quad (5.1)$$

In addition to removing all of the macroscopic pores ($> 35 \mu\text{m}$) from the analyzed polished surface areas, Figure 5.5 shows that HIP also had an effect on pore shape. This figure indicates that proportionally speaking, 10% more of the remaining pores after HIP possessed PGF of 0.1 or less. As can be seen by the illustration included in the top right of the figure, even a pore geometry factor of 0.177 represents a relatively spherical pore. As well, for both FH and CH series, there were reductions in the proportion of pores that had PGFs of 0.2 or more.

Although the analysis provided by the PGF provides information on the approximate shape of the pores, it does not account for jagged irregularities contained within the pores. Sharp edges or corners (dependent on orientation) within flaws are known to further amplify stresses and promote premature crack initiation. Figure 5.6 shows that some of the largest pores possessed cloverleaf-shaped irregularities after HIP.

As can be observed from Figure 5.6b, a post-HIP pore measuring over $200 \mu\text{m}$ was observed during optical analysis of specimen FH61. Although the results summarized in Figures 4.5 and 4.6 do not indicate that there were any remaining pores larger than $35 \mu\text{m}$, this example clearly indicates that macroscopic pores may not have entirely been eliminated during HIP. If such large macropores happened to be close to the specimen surface within the gauge section, that specimen would likely fail in fatigue after a relatively short life.

5.2.5 HIP effects on mechanical properties and fatigue behaviour

Figure 4.9 shows that hardness was essentially unaffected by HIP. This indicates that mechanical properties such as σ_y and UTS likely did not change after HIP. That being said, crack growth mechanisms are not necessarily linked to the aforementioned

5.2. Hot iso-static pressing (HIP)

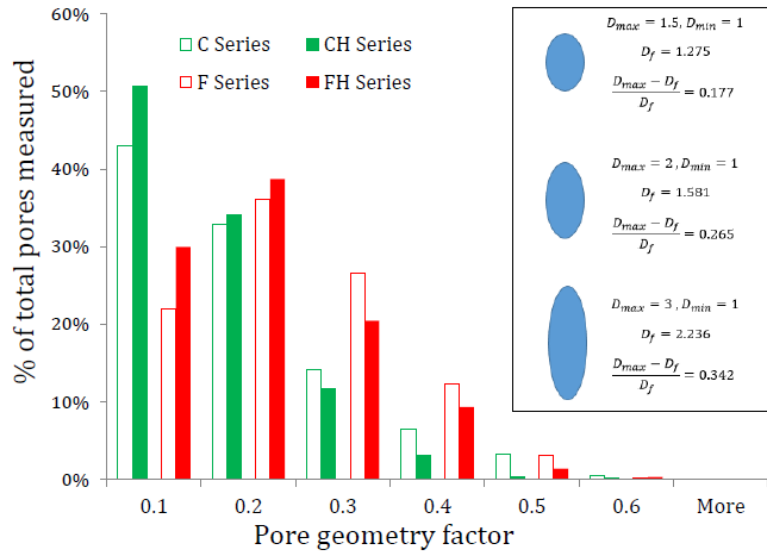


Figure 5.5: Pore geometry before and after HIP for F and C series Galfenol.

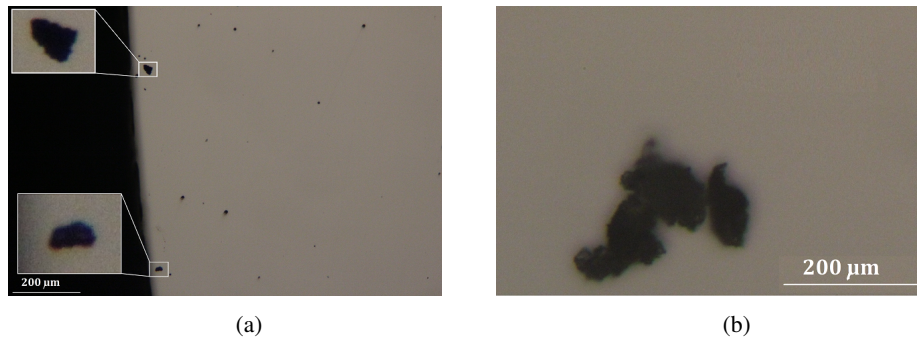


Figure 5.6: Plastic deformation observed for larger HIPed pores for metallographic samples taken from specimens a) CH5 and b) FH61.

mechanical properties. As mentioned earlier, it was expected that reductions in P would result in improvement of overall fatigue behaviour.

Figures 4.1 and 4.2 compare as-received and HIP fatigue results for each tested series. In these figures, it is evident that the amount of scatter remained high after HIP. The data also suggest that HIP resulted in small increases in fatigue behaviour, especially for the C series. At each tested σ_a , the longest lasting fatigue specimen was in fact from HIP material, for both FH and CH material.

In order to quantify the change in scatter and the potential increase in fatigue

behaviour, it was necessary to conduct a regression analysis between $\log(N_f)$ and σ_a for each data set. Once completed, the results were submitted to an analysis of variances (ANOVA), a statistical method introduced by Snedecor [78] and commonly used to determine the statistical significance between two samples of data. As it is often done for S-N fatigue results, it was assumed that the test data were log-normally distributed in order to proceed with the regression analysis.

Results from this analysis were then used to predict and plot mean S-N curves for each data set, as well as the stdv on N_f , the value used to describe data scatter. Figure 5.7 includes a graphical depiction of these results, including scatter bands over one stdv. Subjectively, it is difficult to determine whether HIP had any effect on the fatigue behaviour of the more brittle F series Galfenol. Values for the stdv and the coefficient of determination or data fit (R^2) are included in Table 5.1. Given the excessive amount of fatigue scatter for the FH series, its R^2 is particularly poor. In fact, the stdv values indicate that the scatter increased by 43% after HIP for the higher Ga content F series (FH series).

Table 5.1: Fatigue data analysis results. Stdv denotes the standard deviation of N_f and for the M series row, the last three cells indicate results for the statistical comparison of the M and F series.

Regression analysis results			Comparison of data sets		
Series	Data fit (R^2)	stdv ($\pm 10^x$) $x =$	F score	F critical	p -value
F	0.67	0.76	3.92	4.11	0.055
FH	0.17	1.09			
C	0.40	1.02	7.07	4.10	0.011
CH	0.50	0.94			
M (M vs F)	0.75	0.72	5.14	4.18	0.031

Although it is easy to subjectively assess the results, given the limited number of data and the substantive amount of scatter, this approach alone is not satisfactory for describing the effects of HIP. With R^2 values ranging around 0.45 ± 0.2 , none of the fitted curves included in Figure 5.7 are particularly good fits. This is in large part why an ANOVA was required to compare fatigue results. Next to some of the regression analysis results, the key ANOVA results are also listed in Table 5.1. See Annex B for the steps and equations used to obtain the tabulated results. It is also important to note that for the ANOVA, the null hypothesis (H_o) consisted of the following statement:

$H_o = \text{HIP}$ had no effect on S-N curves and compared data are effectively the same.

As it is the convention for many scientific statistical analysis, a significance (α) of 0.05 was also used for the calculations. This value directly relates to the level of statistical confidence of the test being conducted. For scientific testing, α is most conventionally 0.05 or 0.01. Given the variability in results inherent to fatigue testing, and the particular scatter observed in this project, the more precise $\alpha = 0.01$ was not used.

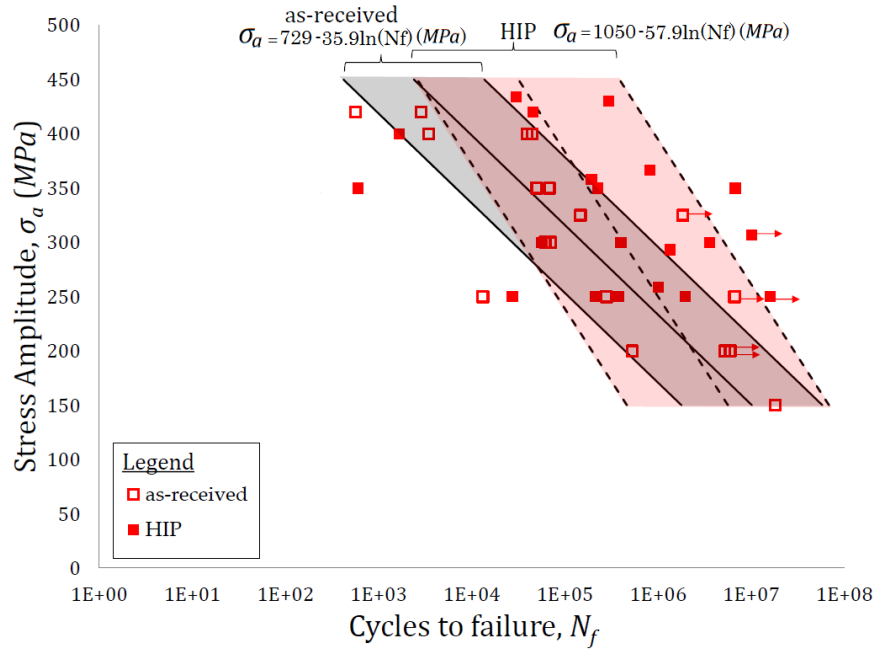
In summary, the data scatter as defined by one stdv was approximately one order of magnitude ($10^{0.84} \pm \sim 10^{0.15}$) for the as-received Galfenol. Scatter actually increased by 43% for the F series and decreased only by 8% for the C Series. For the F series, visual interpretation of Figure 5.7a can show that there is more of the FH scatter band to the right of the F series scatter band, especially at higher stresses. That being said, with a p value of 0.055, there is only weak evidence that these correlations are statistically different. It can therefore be said that there is not enough statistical evidence to show that HIP had a positive effect on the fatigue behaviour of F series Galfenol.

For the C series, there is strong statistical evidence that the increase in fatigue behaviour is significant. Figure 5.7b and Table 5.1 indicate that scatter was only reduced by 8%. Taking into account the slight decrease in the slope of the CH S-N curve, the predicted increases in fatigue life (N_f) based on the mean S-N curves would be almost two orders of magnitude at lower σ_a , ~ 100 MPa. Remembering that regression analysis produced relatively poor fitting curves, it can therefore be said that on average, assuming that the as-received and HIP S-N curves should be parallel, that HIP increased fatigue life by about one order of magnitude ($10^{0.95}$).

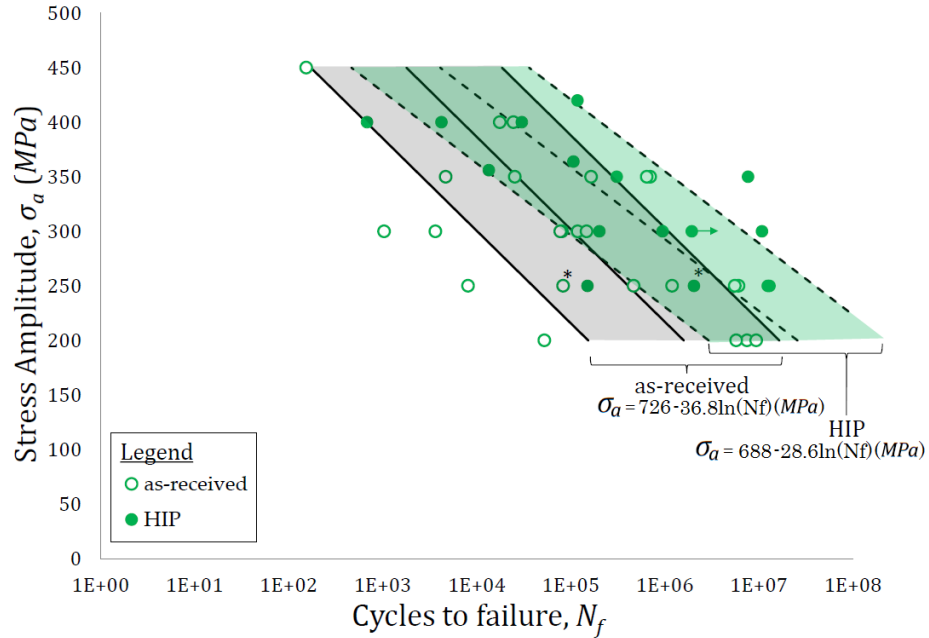
It is interesting to note that P reduction was more pronounced in the F series (91.7%) than in the C series (80.1%) yet the fatigue life improvements were only essentially observed in the C series Galfenol. It is suspected that the more brittle nature of the F series Galfenol might be the cause of the retained fatigue scatter. This indicates that the large grain size of the weak intergrain boundaries are also major contributing factors to fatigue scatter.

As well, the fatigue results indicate that the M and F series fatigue data sets are statistically separate from one another. That being said, Figure 4.3 shows that the M series results fall well within the F series scatter band and that their mean S-N curves are essentially the same. The same figure also shows that M and C series Galfenol effectively have the same S-N curves. This indicates that statistically speaking, the fatigue results indicate that Ga content between 12.4–18.4 at.% has little effect on the fatigue behaviour of Galfenol.

5.2. Hot iso-static pressing (HIP)



(a) F series



(b) C series

Figure 5.7: Effect of HIP on fatigue behaviour of Galfenol with $R = -1$. Sets of three lines represent the predicted mean S-N curves \pm one standard deviation and the indicated equations represent σ_a for the mean S-N curves.

5.3 Image analysis

While observing the polished but unetched metallographic specimens under low magnification ($\times 10$), pores were in very high contrast to the polished material. In an effort to keep the selection of micrographs random, the exact position of the micrographs along the polished surface was obtained without looking in the microscope, only by moving the specimen around on the microscope. Once the pictures were taken, micrographs were also taken of artifacts of interest. See Figure 5.4 as an example of a macroscopic surface-connected pore.

From the principles of fracture mechanics, flaws near the edge of a specimen introduce much higher stress concentrations than internal flaws of the same size. In this particular case, this surface connected pore was not in the gauge section of a specimen. If it would have been, it would likely have introduced massive stress concentrations within the gauge section, resulting in prematurely large crack growth rates and early fatigue failure. Given the random nature of the pore distribution, this may also contribute to data scatter.

5.3.1 Image analysis software

The use of image analysis software helped standardize the image processing for each micrograph, but there still remains some subjectivity in the manner with which pore dimensions were measured. In essence, the image analysis software determined pore size by counting how many pixels were in a given pore. Using micrographs of a 1 mm calibrating tool, the number of pixels for the micrographs of each magnification was calibrated and the number of pixels could be used to determine D_f , total area, D_{min} , and D_{max} of pores.

Where there is some subjectivity in the process rests in the step used to produce the heavy white on black contrast used for pore size and shape measurement (see Figure 3.10). As can be seen in Figure 5.8, too little or too much contrast could skew the measured size of a pore. The subjective part of the analysis consisted of adjusting the contrast level so that the white on black pore looked about the same size as the original pore. An example of this is seen in Figure 5.8b.

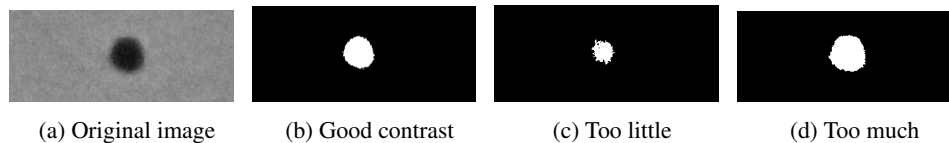


Figure 5.8: Illustration of the contrasting effect on pore size analysis.

Figure 5.8 shows that changes in contrast level could affect pore dimension results. This effect was more pronounced for microscopic pores. Small changes in contrast for sub 5 μm pores could easily double the effective size of the pores or make it disappear completely. As smaller pores are not expected to be deleterious to fatigue life, the level of contrasting was adjusted to best represent the larger pores. Consequently, the measured dimensions for the smaller pores may have been affected by up to 50%. With the same approach being applied to HIP specimens, there is more fidelity on the values of D_f for pores larger than 10 μm than there is for the smaller micropores.

Looking back to Figures 4.5 and 4.6, it is evident that the number of larger pores was dramatically reduced with HIP, for both C and F series Galfenol. As the larger pores were theorized to have the most damaging effect on fatigue, it is therefore expected that fatigue lives would also be improved. From the resulting fatigue data, although it can be argued that there was some improvement in the fatigue life, the effect was not as dramatic as the change in porosity, about 90%.

5.4 Fractography

Upon failure, the fatigue specimens were observed under optical microscope up to x75 magnification in order to identify the source and type of failure. For essentially all C and F Galfenol specimens, there were very little signs of crack propagation and failure was very brittle in nature. Although some specimens demonstrated intergranular failure, all specimens failed in mixed mode with the majority of failure being intragranular. As will be discussed later on, crack propagation near crack initiation sites were also intergranular, indicating that weak grain boundaries may have been the sources of hastened crack propagation for some of the shorter lived specimens. Fracture in the higher Ga content F and FH series was predominantly intragranular.

As can be seen in Figure 5.9, crack propagation in the F and FH series was limited to approximately 100 μm at the time of fracture. The more ductile C and CH series specimens produced fatigue cracks that were closer to 500 μm at the time of fracture. Micrographs of fracture surfaces from short and long lasting specimens from each series are included in Figure 5.9.

Another observation is that less than 10% of the specimen fracture surfaces possessed clamshell-like markings typical of most steel fatigue fracture surfaces (see Figure 2.16). C2 as seen in Figure 5.9a was one of the very few fatigue specimens whose fracture surfaces showed “thumbnail” markings. Coincidentally, this specimen was also one of the longest lasting C series specimens. A close-up of the striations is provided in Figure 5.10.

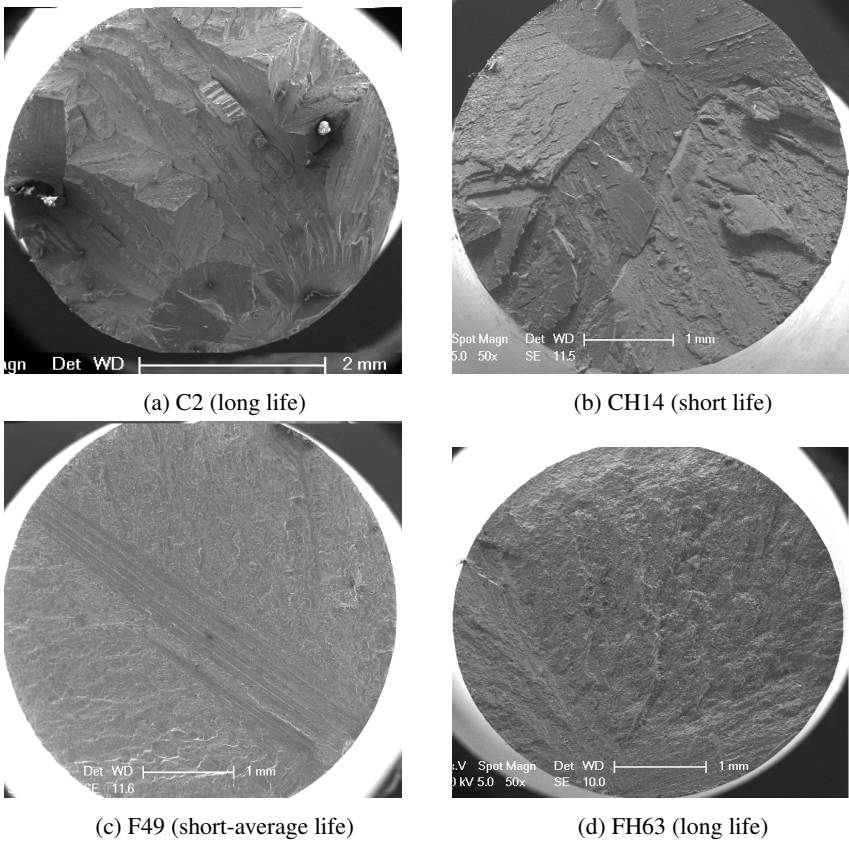


Figure 5.9: Mixed mode inter and intragranular fracture surfaces of C, CH, F, and FH Galfenol.

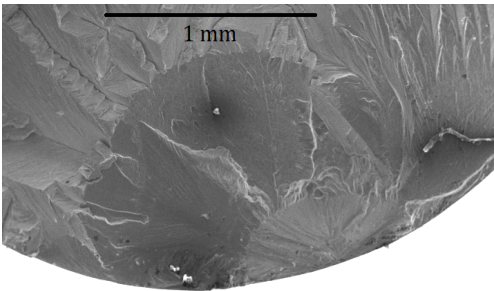


Figure 5.10: Fracture surface of long-lasting specimen C2 with visible striations and thumbnail formation.

5.5 Sources of fatigue failure

As mentioned earlier, due to the three-dimensional nature of fatigue crack growth and fracture surfaces, SEM was a good tool to obtain fractographs. As expected for fatigue specimens, crack initiation all stemmed from *irregularities* located near specimen surfaces. The idea that surface-connected flaws produced larger stress concentrations was introduced in Section 5.2.3. As well, an example of a surface-connected pore that could potentially shorten fatigue life was presented in Figure 5.4. Figure 5.11 provides four other examples of such surface-related *irregularities* that were identified as the source of crack initiation in four of the most short-lived specimens tested (see Figures 4.1 and 4.2).

In the case of F3 and F11 (see Figures 5.11a and 5.11b), fatigue failure most likely stemmed from the propagation of cracks, which initiated at near-surface pores. The two examples of the surface-related *irregularities* are very similar to the one presented in Figure 5.4. As explained earlier, macroscopic pores can be the source of intense stress concentrations and are likely sites for crack initiation. For the examples provided in Figures 5.11a and 5.11b, the macroscopic pores and associated fatigue cracks effectively become one large surface connected defect when the cracks grow out to the specimen surface. Subsequently, the flaw becomes more damaging and crack growth rates for cracks emanating inwards are further increased. Given that the

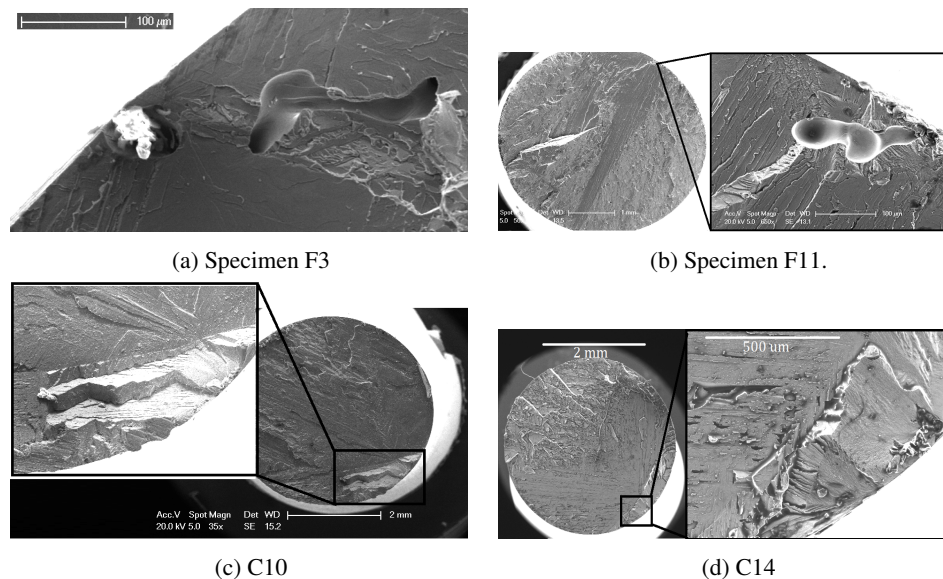


Figure 5.11: Suspected sources of failure in short lived fatigue specimens.

size, shape, and proximity to the surface of macroscopic pores are all variable, the degree to which pores affect fatigue behaviour is also random. This in part explains why macroporosity is associated with data scatter.

The removal of such macroscopic pores was expected to significantly reduce scatter and overall, improve fatigue behaviour. Although it has been shown that macroporosity was removed by HIP, data scatter was not affected in the HIPed material. As will be discussed next, it is expected that material texture and macroscopic grain sizes are the cause for the retained data scatter.

5.5.1 Grain size and effects on fatigue behaviour

The micrographs in Figure 5.11 were selected because they best exemplify the type of irregularities found in short-lived specimens. Although no pore-related fatigue failures were observed in HIPed specimens, it was observed that fatigue crack initiation stemmed from grain-related irregularities, such as the ones captured in in Figures 5.11c and d.

As mentioned earlier, increases in d have been shown to reduce fatigue lives and increase data scatter for many metals (see example on Ti alloys from Figure 2.24). Considering that the Galfenol specimens have been shown to possess grains with d of the order of 1 mm, nearly two orders of magnitude larger than d typically found in commercial steels, d effects were likely an important contributor to the observed data scatter.

As discussed in Section 2.8.2, crack growth is most often classified in two stages. Stage *I* cracks propagate along the weakest path of a grain, along its maximum shear planes. For the majority of metals used in structural applications, grains are usually microscopic ($\sim 10\ \mu\text{m}$) and cracks must typically propagate through many grains before the onset of stage *II* crack growth and then well beyond the onset of stage *II* before failure is expected to occur. In such cases, grain boundaries and neighbouring grains, which are non-preferentially oriented, both act as barriers to crack growth and da/dN is not dependent on grain orientation. In coarse-grained metals, the opposite is true.

For brittle materials such as Galfenol (see Section 2.4.3), stage *II* of crack growth might not even occur. Brittle metals generally have low fracture toughness and sub-grain sized cracks seem sufficiently long to induce fracture. As mentioned previously in Section 5.4, critical flaw lengths (a_c) at the time of failure were well below 1 mm in the majority of the observed specimens. The fact that there are no striations similar to those illustrated in Figure 2.16 along the fracture surfaces of short-lived fatigue specimens supports this idea. Considering that grains are typically larger than a_c , cracks may therefore grow unhindered in stage *I* if grains happen to be preferentially oriented. The randomness of d and grain orientation where cracks initiate explains

why fatigue data scatter is expected in coarse-grained metals. In the case of C10 and C14, which were also two relatively short-lived specimens, fatigue failure stemmed from such near surface grain-related *irregularities*.

5.5.2 Deformation mechanism

During observation of fracture surfaces with SEM, some additional material artifacts were captured. Of note, slip bands were observed. Similar, but more pronounced slip bands were also observed in some of the etched metallographic specimens. As seen in Figure 5.12, these artifacts were notably visible within the grip section, where plastic deformation was known to have occurred next to the grip wedge teeth marks (Figure 5.12a and b).

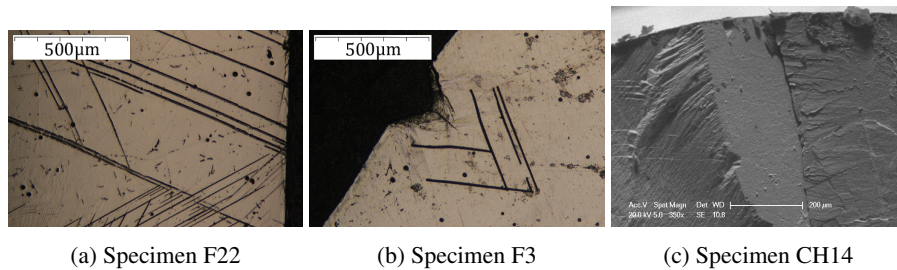
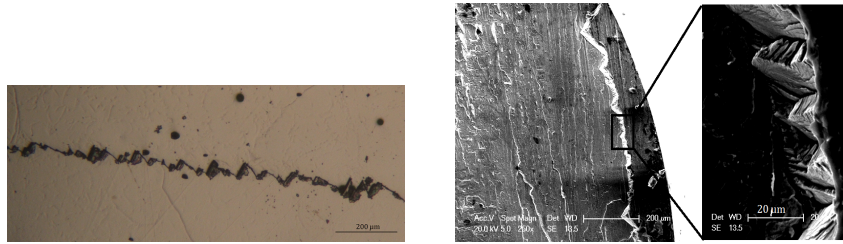


Figure 5.12: Slip band formation in fatigued specimens. Subfigures a) and b) were obtained from metallographic specimens where slip band formation is made evident by etching. Sub-figure c) consists of a micrograph obtained from SEM along the fracture surface of a HIPed specimen.

The theory put forward by Klesnil *et al.* [66] in 1965 had shown that slip bands pile up at grain boundaries and do not propagate into neighbouring grains. As dislocations pile up at grain boundaries, with time, they create intrusions and extrusions, as was presented in Figure 2.15. The magnitude of the pile-ups and irregularities increases with larger grains because more dislocations can exist within each grain. Such dislocation pile-ups were observed along grain boundaries on polished and etched metallographic. Similar dislocation pile-ups were also observed by SEM. Examples of these observations are provided in Figure 5.13.

In terms of effects on fatigue behaviour, such dislocation pile-ups surely introduced stress concentrations, which can lead to the initiation of cracks (see Figure 2.15). When occurring internally, such irregularities do not pose as large a stress concentration as if they occur near the specimen surface where edge effects further increase stress amplification. With grain boundaries suspected of being weak for

5.5. Sources of fatigue failure



(a) Etched metallographic surface obtained from specimen F22 (b) SEM micrograph of specimen F9's fracture surface

Figure 5.13: Dislocation pile-up occurrences at grain boundaries.

high-Ga content Galfenol, the introduction of such dislocation pile-ups along grain boundaries would likely expedite crack initiation or crack growth.

5.6 M series testing

As discussed in Section 5.2, the first attempts to HIP at 193 MPa were unsuccessful since surface and internal porosity was still visible. It was uncertain how successful HIP would be at removing porosity. It was theorized that P would be more easily removed in a softer alloy. As the ductile to brittle transition occurs between 15-18 at.% Ga content, the third Galfenol alloy selected for this project contained 12.4 at.% Ga content. Two 125 mm long and 24 mm diameter cylindrical rods were purchased and one of the rods was machined to produce the eight fatigue data included in Figure 4.3.

It was decided not to HIP the M series Galfenol, as HIP of the C and F series proved successful in reducing total surface area porosity by about 90%, and because fatigue data was not dramatically influenced by this change. It was assumed that HIP would have similar effects on the fatigue behaviour of M series Galfenol.

Of note, the one data point for the M series which failed at 400 MPa was the only specimen to fail by ductile failure. As M series Galfenol has been shown to possess σ_y of approximately 375 MPa (see Figure 4.10), it is of no surprise that ductile failure was observed after so few cycles, only 216 full reversals.

6 Conclusions

Since the 1970s, functional ceramics like piezo-electric ceramics with magnetostrictive properties have replaced the use of Ni alloys or other magnetostrictive metals in the design of sensing and actuating applications. With modern advances, these materials now offer magnetostrictive potentials upwards of 1000 ppm, more than an order of magnitude larger than the magnetostrictive potentials offered by first generation sensing materials dating back to WWII (see Figure 1.1). Although ideal for sophisticated applications, these materials are expensive to produce and their use in demanding environments becomes costly when their inherent low fracture toughness results in frequent failure.

Galfenol steel, a low-carbon steel alloyed with 15-20 at.% Ga, provides a never before seen balance between good mechanical properties similar to that of other steels and magnetostrictive potential as high as 400 ppm, nearly half that of piezo-electric ceramics. A common processing technique used to produce preferentially-oriented grain texture in polycrystalline Galfenol is the Bridgman rod technique, a process which involves slow extrusion and directional solidification of a starting melted ingot from a heat source. Although this process enhances the preferential grain orientation required to maximize λ_s , grain growth of up to and beyond 1 mm diameter as well as inherent macroporosity are accompanying and undesirable side effects. The as-received Bridgman rods acquired for this project all possessed significant macroporosity, with surface-connected and internal isolated macropores measuring as large as 1 mm in diameter. Total surface area porosity obtained from polished metallographic F and C series specimens were 0.48% and 0.35%, respectively.

Given that many of the applications for which Galfenol is being considered consist of repetitive loading, it is imperative that Galfenol's fatigue behaviour be determined. Early attempts at producing S-N fatigue curves for tension-compression axial tests with constant σ_a produced highly scattered data. As macroporosity is known to reduce N_f and increase data scatter, it was theorized that P reduction by HIP would improve fatigue behaviour. In all, three Galfenol steel alloy compositions were tested: F, C, and M series Galfenol with $\text{Fe}_{81.6}\text{Ga}_{18.4}\text{C}_{0.15}$, $\text{Fe}_{82.8}\text{Ga}_{14.9}\text{Cr}_{2.2}\text{C}_{0.15}$, and $\text{Fe}_{87.6}\text{Ga}_{12.4}\text{C}_{0.15}$, respectively.

In line with this project's three objectives, the following conclusions have been produced:

1. Evaluate the effectiveness of HIP: The effectiveness of HIP on the reduction of P was quantified using two approaches.
 - The first approach consisted of comparing material densities through water displacement techniques. HIP improved density of F and C series Galfenol by 0.9% and 1.1%, respectively. Assuming that ρ_{th} of both Galfenol alloys was 7.973 g/cm^3 , these increases in ρ would equate to a $90\% \pm 5\%$ decrease in P .
 - The second approach used to quantify the effects of HIP on P consisted of computer-aided visual analysis of micrographs obtained from polished and non-etched metallographic specimens. Results from this analysis indicated that total surface area porosity (see Section 3.5.3) was reduced by 91.7% and 80.1% for F and C series, respectively. More importantly, this analysis indicated that the HIPed alloys no longer possessed macropores, pores with D_f larger than $35 \mu\text{m}$. Although it was somewhat redundant, both approaches indicated that HIP dramatically reduced the size and number of pores in the as-received material.
2. The effect of P on the fatigue behaviour of Galfenol: Given that P was effectively removed by HIP, it was expected that the material's fatigue behaviour would also be positively improved. Unfortunately, the fatigue data for the FH series was actually 43% more scattered than the F series Galfenol. Although the fatigue behaviour documented in Figure 5.7a seems to be better after HIP, especially for higher σ_a , the limited number of data points and the significant amount of scatter indicate that there is in fact not enough statistical evidence to indicate that HIP improved fatigue behaviour of the F series. Conversely, the mean S-N results for the CH material was 95% improved over the as-received C series Galfenol (Figure 5.7b) and the data scatter for the CH series was reduced by 8%. It is interesting to see that even with 91.7% reduction in P , fatigue behaviour of the higher Ga content F series Galfenol was not improved. It is suspected that the macroscopic grain sizes and the low fracture toughness associated with the presence of weak intergrain Ga rich precipitates are the main factors involved with persistent scatter in results for the F series.
3. Gallium content affect on fatigue behaviour: As seen in Figure 4.3, results also indicate that Ga content between 12.4–18.4 at.% has no significant effect on the fatigue behaviour of Galfenol. Because improvements in fatigue behaviour for the F and C series Galfenol were modest, the remaining as-received M series Galfenol was not HIPed for further testing.

7 Recommendations

The modest changes in fatigue behaviour observed after HIP do not justify the costs associated with the HIP process. Hot rolling processes have been shown to produce preferential grain growth and result in comparable levels of λ_s than those produced by DS (~ 150 ppm [4]). As hot rolling processes are also effective at removing porosity, they would likely be better manufacturing options for the production of bulk Galfenol destined for cyclical loading applications.

Another insight from this project is that the largest λ_s observed in polycrystalline Galfenol are well below 400 ppm, the largest λ recorded on single crystal Galfenol [16]. Considering that Galfenol is relatively stiff, with a bulk elastic modulus below 200 GPa, associated σ required to “actuate” such strains remain well below 80 MPa. Fatigue results indicate that at 80 MPa, short-lived Galfenol components would still be expected to last beyond 10^7 – 10^8 cycles, which is essentially infinite for most applications. Given the limited amount of material available for testing, high cycle fatigue testing at lower σ_a was not conducted. It is recommended that further testing with σ_a below 150 MPa be conducted to better map Galfenol’s fatigue behaviour.

It has been shown that large d can also be detrimental to fatigue life and that at extremes, can also lead to significant increases in data scatter. Given that d in the as-received DS Galfenol was macroscopic, beyond 1 mm in diameter, grain size effects were likely large contributors to fatigue scatter in both as-received and HIP material. Recent research [43, 42] has shown that much like steels, alloy additions can help increase inter-grain boundary cohesion, reduce d , and reduce the formation of secondary phases. It is suspected that in order to reduced fatigue scatter, both d and pore sizes need to be reduced. Assuming that finer grained Galfenol can retain its sought-after λ_s , it is recommended that grain size effects on fatigue scatter be further studied. As discussed earlier, Summers *et al.* [30] had shown that extraction rates can have significant impact on d . One simple process that could be used to obtain Galfenol with a variety of grain sizes would be to conduct fatigue tests on DS Galfenol extracted at different rates. Given that porosity is inherently reduced in hot rolled Galfenol, it would also be recommended to pursue fatigue testing on sheet Galfenol processed by hot rolling.

References

- [1] James P. Joule. XVII. On the effects of magnetism upon the dimensions of iron and steel bars. *The London, Edinburgh, and Dublin Philosophical Magazine and Journal of Science*, 30(199):76–87, 1847.
- [2] J. Atulasimha, A.B. Flatau, and E. Summers. Characterization and modeling of the magnetomechanical behavior of polycrystalline iron-gallium alloys. *Smart Materials and Structures*, 16(4):1265, 2007.
- [3] W. D. Callister and D. G. Rethwisch. *Materials Science and Engineering: an Introduction*, volume 7. Wiley New York, 8 edition, 2007.
- [4] Rick A. Kellogg. *Development and modeling of iron-gallium alloys*. PhD thesis, Iowa State University, 2003.
- [5] Rupal Jain. *Design and packaging of an iron-gallium (Galfenol) nanowire acoustic sensor for underwater applications*. ProQuest, 2007.
- [6] A.E. Clark, M. Wun-Fogle, J.B. Restorff, and T.A. Lograsso. Magnetostrictive properties of Galfenol alloys under compressive stress. *Materials Transactions*, 43(5):881–886, 2002.
- [7] S.P. Khromov. Great soviet encyclopedia (a translation of the 3rd edition). *New York: Macmillan London, Collier Macmillan Publishers*, 17:129, 1978.
- [8] K. Honda and S. Kaya. On the magnetization of single crystals of iron. *Sci. Rep. Tohoku Imp. Univ*, 15:721–754, 1926.
- [9] Ryan S. Scott. *Measurements on Galfenol Material and Transducers*. PhD thesis, The Pennsylvania State University, 2008.
- [10] E. Tatsumoto and T. Okamoto. Temperature dependence of the magnetostriction constants in iron and silicon iron. *Journal of the Physical Society of Japan*, 14(11):1588–1594, 1959.
- [11] R.C. Hall. Single crystal anisotropy and magnetostriction constants of several ferromagnetic materials including alloys of NiFe, SiFe, AlFe, CoNi, and CoFe. *Journal of Applied Physics*, 30(6):816–819, 1959.
- [12] A.E. Clark, R.M. Bozorth, and B.F. Savage. Anomalous thermal expansion and magnetostriction of single crystals of dysprosium. *Physics Letters*, 5(2):100–102, 1963.

- [13] A.E. Clark and H.S. Belson. Giant room-temperature magnetostrictions in TbFe_2 and DyFe_2 . *Physical Review B*, 5(9):3642, 1972.
- [14] J. Atulasimha and A.B. Flatau. A review of magnetostrictive iron–gallium alloys. *Smart Materials and Structures*, 20(4):043001, 2011.
- [15] E.O. Hall. The deformation and ageing of mild steel: III discussion of results. *Proceedings of the Physical Society. Section B*, 64(9):747, 1951.
- [16] A.E. Clark, J.B. Restorff, M. Wun-Fogle, T.A. Lograsso, and D.L. Schlagel. Magnetostrictive properties of body-centered cubic Fe-Ga and Fe-Ga-Al alloys. *IEEE Transactions on Magnetics*, 36(5):3238–3240, 2000.
- [17] M. Wun-Fogle, J.B. Restorff, and A.E. Clark. Magnetostriction of stress-annealed Fe-Ga and Fe-Ga-Al alloys under compressive and tensile stress. *Journal of Intelligent Material Systems & Structures*, 17(2):117–122, 2006.
- [18] M. Brooks, E. Summers, and T.A. Lograsso. Gallium content effects in low carbon steels. *AIST Steel Properties & Applications Conference Proceedings and Materials Science & Technology*, ASM International:681–692, 2009.
- [19] A.E. Clark, K.B. Hathaway, M. Wun-Fogle, J.B. Restorff, T.A. Lograsso, V.M. Keppens, G. Petculescu, and R.A. Taylor. Extraordinary magnetoelasticity and lattice softening in BCC Fe-Ga alloys. *Journal of Applied Physics*, 93(10):8621–8623, 2003.
- [20] Q. Xing and T.A. Lograsso. Phase identification of quenched FeGa_{25} . *Scripta Materialia*, 60:373–376, 2009.
- [21] E.M. Summers, R. Meloy, and Suok-Min Na. Magnetostriction and texture relationships in annealed Galfenol alloys. *Journal of Applied Physics*, 105(7):07A922, 2009.
- [22] M. Brooks, E. Summers, J.B. Restorff, and M. Wun-Fogle. Behavior of magnetic field–annealed Galfenol steel. *Journal of Applied Physics*, 111(7):07A907, 2012.
- [23] H. Wang, Z.D. Zhang, R.Q. Wu, and L.Z. Sun. Large-scale first-principles determination of anisotropic mechanical properties of magnetostrictive Fe-Ga alloys. *Acta Materialia*, 61(8):2919–2925, 2013.
- [24] H.M. Schurter, Y. Zhang, R. Wu, and A.B. Flatau. Mechanical behavior and auxetic properties of Galfenol. In *SPIE Smart Structures and Materials+ Non-destructive Evaluation and Health Monitoring*, pages 72891Y–72891Y. International Society for Optics and Photonics, 2009.
- [25] S. Datta, M. Huang, J. Raim, T.A. Lograsso, and A.B. Flatau. Effect of thermal history and gallium content on magneto-mechanical properties of iron gallium alloys. *Materials Science & Engineering*, 435:221–227, 2006.
- [26] Ortrud Kubaschewski. *Iron-binary phase diagrams*, volume 14. Springer, 1982.
- [27] O. Ikeda, R. Kainuma, I. Ohnuma, K. Fukamichi, and K. Ishida. Phase equilibria and stability of ordered BCC phases in the Fe-rich portion of the Fe-Ga system. *Journal of Alloys and Compounds*, 347(1):198–205, 2002.

-
- [28] R.A. Kellogg, A.M. Russell, T.A. Lograsso, A.B. Flatau, A.E. Clark, and M. Wun-Fogle. Tensile properties of magnetostrictive iron–gallium alloys. *Acta Materialia*, 52(17):5043–5050, 2004.
- [29] Jin-Hyeong Yoo and A.B. Flatau. Measured iron-gallium alloy tensile properties under magnetic fields. In *Smart Structures and Materials*, pages 476–486. International Society for Optics and Photonics, 2004.
- [30] E.M. Summers, T.A. Lograsso, J.D. Snodgrass, and J.C. Slaughter. Magnetic and mechanical properties of polycrystalline Galfenol. In *Smart Structures and Materials*, pages 448–459. International Society for Optics and Photonics, 2004.
- [31] Govindhan Dhanaraj, Kullaiiah Byrappa, Vishwanath Prasad, and Michael Dudley. *Springer handbook of crystal growth*. Springer Science & Business Media, 2010.
- [32] T. Ueno, E. Summers, and T. Higuchi. Machining of iron-gallium alloy for microactuator. *Sensors and Actuators A: Physical*, 137(1):134–140, 2007.
- [33] T. Ueno, C. Saito, N. Imaizumi, and T. Higuchi. Miniature spherical motor using iron-gallium alloy (Galfenol). *Sensors and Actuators A: Physical*, 154(1):92–96, 2009.
- [34] Ueno Higuchi, Toshiro and Toshiyuki. *Next Generation Actuators Leading Breakthroughs*. Springer, 2010.
- [35] John Frederick Nye. *Physical properties of crystals*. Clarendon press, 1985.
- [36] M. Jain and M.P. Verma. Poisson’s ratios in cubic crystals corresponding to (110) loading. *Indian journal of pure & applied physics*, 28(4):178–182, 1990.
- [37] R.H. Baughman, J.M. Shacklette, A.A. Zakhidov, and S. Stafström. Negative poisson’s ratios as a common feature of cubic metals. *Nature*, 392(6674):362–365, 1998.
- [38] Yunan Prawoto. Seeing auxetic materials from the mechanics point of view: a structural review on the negative poisson’s ratio. *Computational Materials Science*, 58:140–153, 2012.
- [39] T. Ueno and S. Yamada. Performance of energy harvester using Fe-Ga alloy in free vibration. *IEEE Transactions on Magnetics*, 47(10):2407–2409, 2011.
- [40] C.S. Smith and K.O. McLean. A common equation of state? —LiF, NaF, NaCl, NaI. *Journal of Physics and Chemistry of Solids*, 34(6):1143–1145, 1973.
- [41] MP Seah. Adsorption-induced interface decohesion. *Acta Metallurgica*, 28(7):955–962, 1980.
- [42] L.M. Cheng, L. Eckstrand, and C. Ng. Improving texture in polycrystalline Galfenol: Development of rolling processes. Technical report, Defence Research and Development Canada, 2006.
- [43] Allison Nolting. Tensile properties of ternary Galfenol alloys and Galfenol steel. Technical report, Defense Research and Development Canada, 2011.

- [44] A.E. Clark, J.B. Restorff, M. Wun-Fogle, K.B. Hathaway, T.A. Lograsso, M. Huang, and E. Summers. Magnetostriction of ternary Fe-Ga-x alloys ($x = \text{C, Y, Cr, Mn, Co, Rh}$). *Journal of Applied Physics*, 101(9):09C507–09C507, 2007.
- [45] J.M. Beswick. The effect of chromium in high carbon bearing steels. *Metallurgical Transactions A*, 18(11):1897–1906, 1987.
- [46] Flake C. Campbell. *Elements of metallurgy and engineering alloys*. ASM International, 2008.
- [47] R. Higgins. Engineering metallurgy: Applied physical metallurgy. *Edward Arnold, 1992*, page 560, 1992.
- [48] S. Kocanda. Fatigue of metals. *Sijthoff & Noordhoff*, 1978.
- [49] B Boardman. Fatigue resistance of steels. *ASM International, Metals Handbook. Tenth Edition*, 1:673–688, 1990.
- [50] H. Nakayama. Encyclopedia of materials: Science and technology. *Elsevier Science Ltd.*, 6:2981–2986, 2001.
- [51] J.C. Slaughter, J. Raim, M. Wun-Fogle, and J.B. Restorff. Effect of cyclic stresses and magnetic fields on stress-annealed Galfenol alloys. In *Smart Structures and Materials*, pages 183–191. International Society for Optics and Photonics, 2005.
- [52] ASTM Designation. E466-07: Standard practice for conducting force controlled constant amplitude axial fatigue tests of metallic materials, 2007.
- [53] R.A. Hardin and C. Beckermann. Effect of porosity on the stiffness of cast steel. *Metallurgical and Materials Transactions A*, 38(12):2992–3006, 2007.
- [54] R.A. Hardin and C. Beckermann. Effect of porosity on deformation, damage, and fracture of cast steel. *Metallurgical and Materials Transactions*, 44:5316–5332, December 2013.
- [55] N.A. Fleck and R.A. Smith. Effect of density on tensile strength, fracture toughness, and fatigue crack propagation behaviour of sintered steel. *Powder Metallurgy*, 3:121–125, 1981.
- [56] R.J. Bourcier, D.A. Koss, R.E. Smelser, and O. Richmond. The influence of porosity on the deformation and fracture of alloys. *Acta Metallurgica*, 34(12):2443–2453, 1986.
- [57] J. Holmes and R.A. Queeney. Fatigue crack initiation in a porous steel. *Powder Metallurgy*, 28(4):231–235, 1985.
- [58] K.M. Sigl, R.A. H.R.A. Hardin, I. Stephens, and C. Beckermann. Fatigue of 8630 cast steel in the presence of porosity. *International Journal of Cast Metals Research*, 17(3):130–146, 2004.
- [59] ASTM Designation. E446: Nondestructive testing.
- [60] N. Chawla and X. Deng. Microstructure and mechanical behavior of porous sintered steels. *Materials Science & Engineering*, 390:98–112, 2005.

-
- [61] R.W. Armstrong. The influence of polycrystal grain size on several mechanical properties of materials. *Metallurgical Transactions*, 1:1169–1176, May 1970.
- [62] W.J. Craig and G.M. Sinclair. Influence of grain size on work hardening and fatigue characteristics of α -brass. *ASM TRANS Q*, 44:929–948, 1952.
- [63] A.W. Thompson and W.A. Backofen. The effect of grain size on fatigue. *Acta Materialia*, 19:597–606, 1971.
- [64] R.C. Boettner, C. Laird, and A.J. McEvily. Crack nucleation and growth in high strain low cycle fatigue. *TRANS METALL SOC AIME*, 233(2):379–387, 1965.
- [65] O.M. Herasymchuk. A generalized grain-size dependence of the fatigue limit. *Strength of Materials*, 43(2):205–216, 2011.
- [66] M. Klesnil, M. Holzmann, P. Lukas, and P. Rys. Some aspects of fatigue process in low-carbon steel. *Journal of the Iron and Steel Institute*, 203:47, 1965.
- [67] A. Yoshikawa and T. Sugeno. Factors responsible for the sharp fatigue limit in iron and steel. *Trans. Metall. Soc. AIME*, 233:1314–1317, 1965.
- [68] S. Taira, K. Tanaka, and M. Hoshina. Grain size effect on crack nucleation and growth in long-life fatigue of low-carbon steel. *Fatigue Mechanisms*, 675:135, 1979.
- [69] A. Jarvenpaa, L.P. Karjalainen, and M. Jaskari. Effect of grain size on fatigue behavior of Type 301LN stainless steel. *International Journal of Fatigue*, 65:93–98, 2014.
- [70] J.H. Li, X.X. Gao, J. Zhu, X.Q. Bao, T. Xia, and M.C. Zhang. Ductility, texture and large magnetostriction of Fe–Ga-based sheets. *Scripta Materialia*, 63(2):246–249, 2010.
- [71] ASTM Standard. E466. *Standard practice for conducting force controlled constant amplitude axial fatigue tests of metallic materials*. West Conshohocken, PA: ASTM International, 2007.
- [72] S. Roy Swanson. Handbook of fatigue testing. In *Handbook of fatigue testing*. American Society for Testing and Materials, 1974.
- [73] Aleksey Zakharenko. First evidence of surface sh-wave propagation in cubic piezomagnetism. *Journal of Electromagnetic Analysis and Applications*, 2010, 2010.
- [74] A.E. Clark. Structural Fe-based alloys with high magnetostriction. In *Galphenol Workshop, University of Maryland, USA*, volume 29, 2004.
- [75] H.V. Atkinson and S. Davies. Fundamental aspects of hot isostatic pressing: An overview. *Metallurgical and Materials Transactions*, 31:2981–3000, 2000.
- [76] Stephen W. Hughes. Archimedes revisited: a faster, better, cheaper method of accurately measuring the volume of small objects. *Physics education*, 40(5):468, 2005.
- [77] ASTM Designation. B311: Standard test method for density of powder metal (P/M) materials containing less than two percent porosity.
- [78] G.W. Snedecor and Cochran W.G. *Statistical methods*, 1967.

Appendices

A Density measurements

In order to quantify the effect that hot iso-static pressing (HIP) had on the porosity of untested Galfenol, it was decided to compare the density of the material before and after HIP. The density of Galfenol rods was calculated by comparing the measured weight of each rod to its total external volume. Each specimen outer volume was obtained by using the water overflow method described by Hughes [76]. Each specimen was submerged in a glass container pre-filled with room temperature deionized water (see Figure A.1). The displaced water overflowed out of the container spout and was collected for weight measurement. The weight of the displaced water was then measured using a Scientech SA 210 electronic scale with a precision of 0.0001 g (see Figure A.2).



Figure A.1: Glassware used to perform water displacement tests.

The volume of the displaced water could be calculated by dividing the weight of the displaced water by the theoretical water density for the observed water tempera-



Figure A.2: Scale used to measure the weight of Galfenol rods and displaced water from submerged rods.

ture during testing. Because the weight of the displaced water was dependent on how much water poured out of the spout, there was some variation from one reading to the next. This was likely due to the difference in how much water adhered to the spout surface after the overflow and how many drops of water continued dripping into the overflow collection container. Although the standard deviation on the weight measurements was only 0.2% of the average of the measured values, four measurements were taken to improve fidelity.

In order to standardize each measurement and to control the rate of the water being poured out of the glass tube, the rods and water were always introduced into a rearward leaning tube as seen in Figure A.3. In order to ensure that the glass cylinder was filled to the same level before each measurement, water was first filled in a rear slanted tube. Once filled beyond the overflow capacity, the tube was steadily returned to the vertical position and excess water flowed out of the spout. Carefully repeating this step for each measurement helped standardize results.

Once the tube was full of water, it was leaned backwards again and the Galfenol specimen was slid into the glass tube. Leaning the tube backwards was necessary to reduce unwanted splashing which could alter results. A rubber stopper was also used at the bottom of the glassware to reduce the risk of damaging or fracturing the glassware. As with the previous step, once the Galfenol specimen was submerged, the glass tube was brought back to the vertical position in a slow, steady, and repeatable fashion. All the displaced water would then pour out of the spout and be collected in



Figure A.3: Insertion of specimen for water displacement test.

a plastic cup for further measurement. Because the mass of displaced water could be greatly affected by the addition of a single drop of water, water dripping out of the spout was only collected for five seconds.

Having measured the average weight of the displaced water as well as its temperature, it was possible to determine the density of the water using available ASTM standard references [77]. With both mass and density of the displaced water, the displaced water volume was calculated and compared to the measured mass, the average specimen density could easily be calculated.

It is important to note that a few drops (~ 0.1 mL) of dish washer rinsing agent, a well-known surfactant, was used to help reduce surface tension in the test water. Given that surface porosity and imperfections were present in most specimens, the addition of rinse agent was expected to help produce more accurate results for displaced water.

B Analysis of variances (ANOVA)

The variances between and within data sets were calculated using the two equations below. SS_x indicates the (S)um of the (S)quares or variance and the suffixes B, W, and T indicate the variance between groups, within groups, or amongst the entire data population, respectively. By definition, the SST, SSB, and SSW are related by the following equation:

$$SST = SSB + SSW \quad (B.1)$$

therefore,

$$SSB = SST - SSW \quad (B.2)$$

As explained earlier, SSW is defined as the variance within the groups being assessed such that:

$$SSW = \sum_i \left(\sum_j (\text{observations} - \text{predicted } N_f \text{ for data group})^2 \right) \quad (B.3)$$

where i is the number of observations in each group and j is the number of groups being compared (2). For these calculations, the variance is calculated as the square of the difference between the predicted N_f obtained by regression analysis and that actual data point obtained in the S-N results.

$$SST = \sum_k (\text{observations} - \text{predicted fatigue life for for both groups})^2 \quad (B.4)$$

k is the total number of observations within the two groups being compared (approximately 35 ± 5). In order to complete the F test, it is also necessary to define the degrees of freedom within and between groups, df_{wg} and df_{bg} , respectively:

$$df_{wg} = \text{total \# observations} - \text{\# groups} \quad (B.5)$$

$$df_{bg} = \text{\#groups} - \text{\#samples} = 2 - 1 = 1 \quad (B.6)$$

And finally, the F score or F factor is calculated using the following equation:

$$F \text{ factor or score} = \frac{SSB \times df_{wg}}{df_{bg} \times SSW} \quad (\text{B.7})$$

In order to interpret the values listed in Table 5.1, it is important to underline a few other key facts:

- A F score that was smaller than the critical F value would indicate that in all likelihood, with 95% confidence, H_o would be true.
- The opposite would also hold true; a F score greater than the critical value would indicate that H_o would be rejected. In this case, this would mean that compared data sets would in fact differ from one another.
- p values less than 0.01 indicate a very strong evidence against H_o . p values between 0.01-0.05 indicate strong evidence against H_o . p values between 0.05-0.1 indicate some but weak evidence against H_o .

C Collected Data

Table C.1: Rockwell B hardness results for tests conducted on as-received and HIPed F series Galfenol specimens, F and FH series, respectively.

Specimen	Measurements			
F1	98.5	102.5	100.5	99.5
F2	95.5	97.5	99.5	93.5
F3	100.5	100.5	102.0	98.0
F4	101.5	103.0	100.5	101.5
F5	97.5	99.5	100.5	98.5
F10	102.5	102.5	99.5	93.3
F11	103.0	102.5	98.0	97.0
F12	105.0	103.0	95.5	98.5
F13	102.5	103.0	101.5	98.5
F14	103.0	101.5	99.5	103.0
F44	98.5	100.5	100.5	101.5
F45	99.5	99.5	97.5	96.5
F46	96.5	98.5	100.0	101.0
F47	101.5	100.5	100.5	99.5
F48	97.5	96.5	94.0	97.0
FH52	93.5	97.5	98.5	97.5
FH53	93.5	96.5	101.0	94.0
FH54	89.3	95.5	100.0	95.0
FH55	92.3	97.5	95.5	96.5
FH56	94.5	93.5	96.5	92.3
FH57	94.5	93.5	96.5	96.5
FH58	88.3	95.5	96.5	95.5
FH59	95.5	97.5	98.5	96.5
FH60	96.5	91.3	95.5	97.5
FH61	91.3	91.3	97.5	93.5
FH62	99.5	97.5	103.0	100.5
FH64	91.3	94.5	95.5	98.0
FH65	98.5	96.5	93.8	96.5
FH66	99.0	99.0	102.5	100.5
FH67	99.0	100.5	100.5	97.5
FH68	101.5	101.5	104.0	105.0
FH69	100.5	101.5	97.5	95.5
FH70	99.5	100.5	99.0	98.5
FH71	98.5	95.5	103.0	101.5

Table C.2: Rockwell B hardness results for tests conducted on as-received and HIPed C series Galfenol specimens, C and CH series, respectively.

Specimen	Measurements			
CH1	98.0	95.0	97.0	97.0
CH2	94.0	94.0	94.0	96.0
CH3	96.0	93.0	93.0	96.0
CH4	93.3	96.0	90.0	86.0
CH5	93.0	75.0	91.3	–
CH6	95.0	97.0	97.0	95.0
CH7	93.3	93.0	99.6	101.0
CH8	94.0	98.0	94.0	95.0
CH9	94.0	93.0	93.3	96.0
CH10	93.0	86.3	93.0	99.5
CH11	94.0	93.0	93.3	93.0
CH12	94.0	93.3	88.3	90.3
CH13	97.0	95.0	94.0	95.0
CH14	92.3	88.3	93.0	88.0
CH15	93.0	91.3	85.3	94.0
CH16	93.0	93.0	81.0	91.0

Table C.3: Rockwell B hardness results obtained for M series Galfenol specimens.

Specimen	Measurements			
M1	89.9	88.1	93.5	92.6
M2	93.5	89.0	94.5	92.6
M3	89.9	77.2	89.0	89.9
M4	89.9	89.0	90.8	92.6
M5	91.7	93.5	94.4	96.3
M6	93.5	92.6	89.9	90.8
M7	92.6	93.5	90.8	89.0
M8	93.5	93.5	94.4	94.4
M9	89.0	89.9	88.1	94.4
M10	89.0	92.6	90.8	94.4
M11	83.3	90.8	90.8	89.9
M12	86.3	85.3	84.0	86.3
M13	88.3	87.3	89.3	85.3
M14	90.8	92.6	93.5	92.6
M15	84.3	87.2	93.5	88.1
M16	88.0	87.0	88.0	86.0

Table C.4: Fatigue data for the F series Galfenol.

Specimen Label	Load (kN)	Stress (MPa)	N_f	Comments
F3	6.274	420	565	
F4	3.835	250	278760	
F7	5.844	400	44554	
F8	2.228	150	18179412	
F9	4.681	325	146342	
F11	5.687	400	3443	
F13	6.333	420	2846	
F14	4.676	325	1847299	Run out specimen
F18	2.949	200	5191367	Run out specimen
F19	5.035	350	49614	
F20	2.905	200	526322	Particularly high error max error reported of 7 MPa
F21	4.576	300	69643	
F22	3.813	250	13133	
F43	3.787	250	–	Broke during gripping
F44	3.761	250	6635285	Run out specimen
F45	3.857	250	–	Broke during gripping
F46	4.655	300	61166	
F47	3.054	200	5945449	Run out specimen
F48	6.172	400	39376	
F49	5.339	350	67900	

Table C.5: Fatigue data for the FH series Galfenol.

Specimen Label	Load (kN)	Stress (MPa)	N_f	Comments
FH50	4.518	300	399118	HIP at 28 ksi
FH51	4.502	300	–	HIP at 28 ksi
FH52	4.342	307	10140226	
FH53	5.139	367	815386	
FH54	3.671	259	996458	
FH55	5.143	358	192336	
FH56	5.823	434	29978	
FH57	5.862	420	45384	
FH58	4.416	304	–	Broke during setup
FH59	4.219	293	1352988	
FH60	4.772	350	594	
FH61	5.436	400	1662	
FH62	4.895	350	223092	
FH63	6.040	430	294080	
FH64	4.905	350	6717749	Tested at 15 Hz
FH65	4.226	300	3587990	
FH66	4.216	300	56544	
FH67	3.565	250	1939172	
FH68	3.609	250	377080	
FH69	3.632	250	212590	Damaged during loading.
FH70	3.578	250	27184	
FH71	3.631	250	15925870	

Table C.6: Fatigue data for the C series Galfenol.

Specimen Label	Load (kN)	Stress (MPa)	N_f	Comments
C1	4.437	300	118828	
C2	5.176	350	700618	
C3	5.916	400	24616	
C4	5.176	350	645536	
C5	4.362	300	80734	
C6		450	154	
C7		400	17641	
C8	3.580	250	466986	
C9	5.234	350	25510	
C10	3.683	250	8101	
C11	3.700	250	6090070	
C12	4.383	300	3641	
C13	3.748	250	5564554	
C14	4.466	300	1038	
C15	2.981	200	7500000	
C16		350	4693	
C17	2.949	200	52526	
C35	2.803	200	9408032	
C36	4.602	300	147516	
C37	3.765	250	1199340	
C38	5.357	350	165168	
C39	5.382	350	–	Failed in the grip section after 2 cycles
C40	3.778	250	83230	
C41	4.645	300	77706	
C42	3.037	200	5760980	

Table C.7: Fatigue data for the CH series Galfenol.

Specimen Label	Load (kN)	Stress (MPa)	N_f	Comments
CH1	5.619	400	30240	
CH2	5.210	364	106968	
CH3	5.101	356	13452	
CH4	6.002	420	118022	Abnormal errors up to 7 MPa reported
CH5	5.113	350	7695238	Abnormal errors up to 7 MPa reported
CH6	5.748	400	4226	
CH7	5.874	400	682	
CH8	5.105	350	308620	
CH9	4.285	300	201646	
CH10	4.403	300	948072	
CH11	4.154	300	10826984	
CH12	3.558	250	12430621	Run on test
CH13	3.495	250	151040	
CH14	3.364	250	2047060	
CH15	3.615	250	12976705	
CH16	4.348	300	1939012	

Table C.8: Fatigue data for the M series Galfenol.

Specimen Label	Load (kN)	Stress (MPa)	N_f	Comments
M1	3.758	300	27154	
M2	5.332	400	214	
M3	3.963	300	91784	
M4	4.049	297	139008	
M5	2.683	200	513998	
M6	3.244	239	469440	Max errors up to 10 MPa observed
M7	3.667	272	379950	
M8	3.412	270	4024428	Tested at 8 Hz. Suspended at $N = 3.5E6$ (storm)
M9	2.629	200	10050230	Run-on test.
M10	3.089	239	11421756	
M11	3.571	270	2469253	
M12	3.380	239	10581984	
M13	2.797	200	19207248	Run-on test